UNIVERSITÀ
DEGLI STUDI
FIRENZE

DOTTORATO DI RICERCA IN ENERGETICA E TECNOLOGIE INDUSTRIALI E AMBIENTALI INNOVATIVE

CICLO XXXI
COORDINATORE Prof. Maurizio De Lucia

Numerical Modeling of supersonic two-phase ejectors working with natural refrigerants

Settore scientifico disciplinare ING-IND/11

PhD Candidate	Tutor
Eng. Francesco Giacomelli	Prof. Adriano Milazzo

Co-ordinatore
Prof. Maurizio De Lucia

Firenze 2015/2018

UNIVERSITÀ
DEGLI STUDI
FIRENZE

DOTTORATO DI RICERCA IN ENERGETICA E TECNOLOGIE INDUSTRIALI E AMBIENTALI INNOVATIVE

CICLO XXXI
COORDINATORE Prof. Maurizio De Lucia

Numerical Modeling of supersonic two-phase ejectors working with natural refrigerants

Settore scientifico disciplinare ING-IND/11

PhD Candidate
Eng. Francesco Giacomelli
Department of Industrial Engineering, Univerity of Florence

Tutor
Prof. Adriano Milazzo
Department of Industrial Engineering, Univerity of Florence

Co-Tutor
Prof. Giuseppe Grazzini
Department of Industrial Engineering, Univerity of Florence

Dr. Federico Mazzelli
Department of Industrial Engineering, Univerity of Florence

Firenze 2015/2018

Abstract

During the recent years the interest of industry and scientific community in refrigeration systems working with natural fluids has considerably grown because of the more and more strict regulations regarding environmentally safe refrigerants.

In the present work, three numerical models for supersonic multiphase ejectors working with natural refrigerants have been developed. These models have been implemented in the commercial code ANSYS Fluent. The fluids considered are R718 for Heat Powered Cycles (HPC) and R744 for Vapor Compression Cycles (VCC).

The condensation process occurring in steam ejectors has been modeled by means of a non-equilibrium wet-steam model, implemented in the commercial code in a way that allows great flexibility in the choice of the physical model settings and calibration parameters. The numerical results have been compared with a Homogeneous Equilibrium Model (HEM) and two experimental test-cases available from the literature: a nozzle and a full ejector. Despite its simplicity, the HEM was found to be more stable from a numerical point of view and it was developed to be adaptable to various fluids, hence it could be regarded as a preliminary analysis tool for both R718 and R744 applications.

The flash evaporation process in the R744 ejector has been studied with the HEM and with a non-equilibrium evaporation-condensation model with real fluid properties. This latter is a general tool that can be applied to virtually any type of compressible multiphase flow. It has been firstly validated on a flashing nozzle test-case available from the literature. Both models have finally been compared with an ejector test case, whose experimental data have been collected by the author during a visiting research period in NTNU-SINTEF Energy Research laboratory.

The development and implementation procedure of the numerical models is explained in detail throughout the Thesis, so that these tools could be reproduced by others.

The Thesis is divided in three main chapters. The first is a description of the ejector physics and main performance parameters used to discuss and compare the results. The second is focused on the condensing steam analysis, the description, implementation and validation of the computational model. The third deals with flashing of carbon-dioxide. The numerical and experimental activity on this topic are presented and discussed in this latter chapter.

Contents

List of Figures

Nomenclature

Latin letters		*Greek letters*	
a	Speed of sound [m s^{-1}]	α	Volume fraction [-]
B	Second virial coefficient [m^{3} kg^{-1}]	β	Mass fraction [-]
C	Third virial coefficient [m^{6} kg^{-2}]	Γ	Mass transfer source term [kg m^{-3} s^{-1}]
c	Specific heat capacity [J kg^{-1} K^{-1}]	γ	Specific heat ratio [-]
G	Gibbs Free-Energy [J]	η	Droplets per unit volume mixture [m^{-3}]
h_{lv}	Latent heat [J kg^{-1}]	λ	Thermal conductivity [W m^{-1} K^{-1}]
J	Nucleation rate [s^{-1} m^{-3}]	ξ	Kantrowitz non isothermal correction
k_b	Boltzmann constant [J K^{-1}]	ρ	Density [kg m^{-3}]
k	Turbulent kinetic energy [m^{2} s^{-2}]	σ	Surface tension [J m^{-2}]
l	Molecular mean free path [m]	τ	Shear stress [Pa]

m	Mass [kg]	φ_{ss}	Supersaturation ratio [-]
n	Droplets per unit mass of mixture [kg^{-1}]	ω	Specific dissipation rate [s^{-1}]
p	Pressure [Pa]	ε	Rate of turbulence dissipation [m^2 s^{-3}]
q_c	Accommodation factor	θ	Angle (°)
R	Specific gas constant [J kg^{-1} K^{-1}]	ς	Mass-specific thermodynamic property
r	Radius [m]	χ	Volume-specific thermodynamic property
t	Time [s]		
T	Temperature [K]		
u	Velocity [m s^{-1}]		
p	Pressure (Pa)		
x	Coordinate (m)		
Y	Mass fraction of the species		

Superscripts/subscripts		Acronyms	
c	Condensation	CFD	Computational Fluid Dynamics
e	Evaporation	EOS	Equation Of State

eff	Effective	EXP	Experimental
l	Liquid	HEM	Homogeneous Equilibrium Model
m	Mixture	HFO	Hydro-Fluoro-Olefin
sat	Saturation	SST	Shear Stress Transport
v	Vapor	UDF	User-Defined Function
d	Droplet	UDRGM	User-Defined Real Gas Model
		MN	Motive Nozzle
		SN	Suction Nozzle

Introduction

The European F-Gas regulation (EU No 517/2014) has pushed stakeholders towards a renewed interest in refrigeration systems working with natural fluids. In order to reduce the fluorinated gas equivalent CO_2 emissions by 72% to 73% by 2030 the introduction of low Global Warming Potential (GWP) alternative refrigerants has started. Among them, natural refrigerants look as a promising alternative to HFCs without an expiration date. The focus of the Thesis will be on ejectors for refrigeration applications with Water/Steam (R718) and Carbon-Dioxide (R744).

To date, the use of ejectors as expansion devices seems to be a promising development field for these components. Their application in substitution of the throttling valve in a vapor compression cycle (VCC) is particularly beneficial for R744 refrigeration technology [1]. The relatively low critical temperature of CO_2 ($\approx 304\,K$) causes the cycle to operate in transcritical mode at higher ambient temperature.

Considering a transcritical refrigeration cycle, one method to reduce the loss of COP due to the expansion process is the introduction of an internal heat exchanger. It has the benefit to reduce the flash gas generation in the expansion by increasing the sub-cooling.

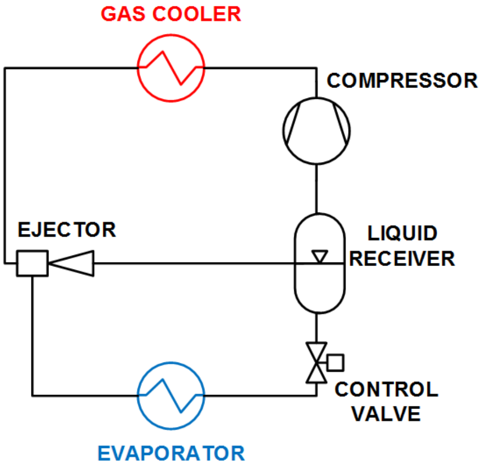

Figure 1 CO_2 vapor compression cycle with ejector

The work recovery by means of mechanical expanders (such as scroll, rotary vane, rolling piston, free piston) is also known to be beneficial both in terms of COP and cooling capacity [2]. The idea is to use the kinetic energy of the expansion process to reduce the compressor work. The isentropic expansion process occurring in the expander (instead of the isenthalpic process) also causes a reduction of the specific enthalpy at the evaporator inlet. As a consequence, one obtains an increase of the system cooling capacity. On the other hand, several problems can result from the introduction of this kind of devices, such as mechanical, thermodynamic and control issues. The cost of expanders is also of the same order of magnitude of compressor cost. Thus reducing the attractiveness of these devices for commercial HVAC&R systems [2].Hence, the focus of industry and researchers has moved to ejectors. They are components that could allow, in principle, the same benefits of mechanical expanders with reduced cost. They are, in facts, relatively cheap and have no moving parts.

The basic idea of an ejector VCC is depicted in Figure 1 where the ejector is placed in substitution of the tradition electronic expansion valve (EEV) at the exit of the Condenser/Gas Cooler.

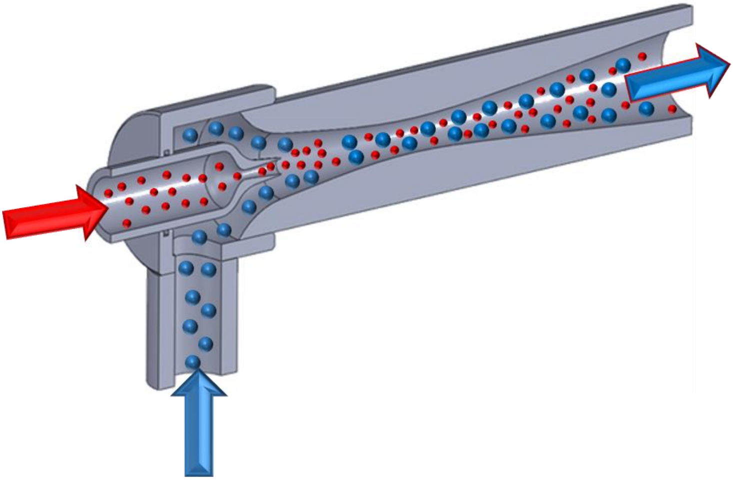

Figure 2 Ejector working principle

The ejector working principle is shown in Figure 2. The expansion of a high-pressure (motive or primary) fluid from the Gas Cooler is used to entrain and compress a low-pressure (suction or secondary) fluid by means of momentum transfer between the two streams of fluid. Other basic configurations are also possible with the introduction of ejectors in place of the EEV. The evaporator overfeeding shown in Figure 3 is a solution where the ejector is mainly used to recirculate the liquid refrigerant in the evaporator to enhance the heat transfer and possibly allow an increment of the evaporation temperature and a consequent increase of the COP [3].

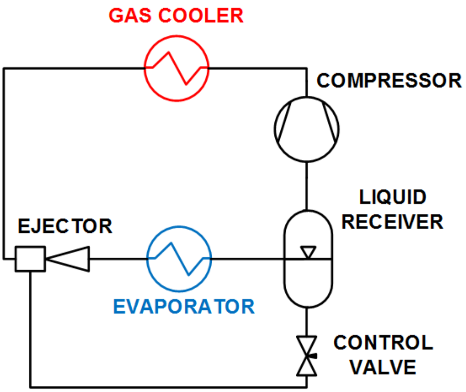

Figure 3 CO_2 vapor compression cycle with ejector and evaporator overfeeding

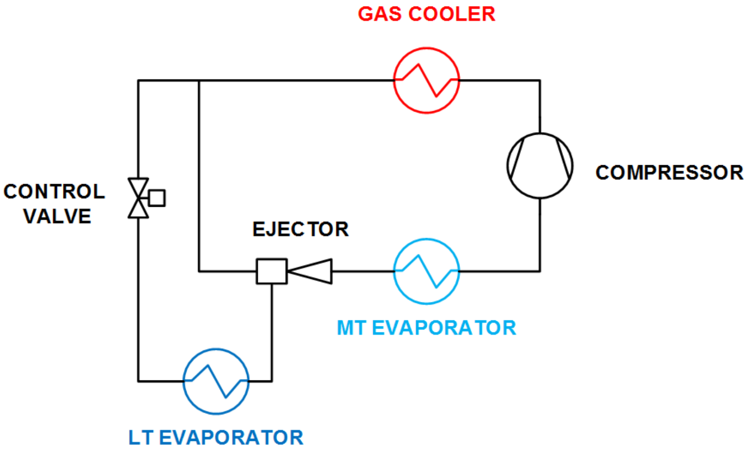

Figure 4 CO_2 vapor compression cycle with ejector and evaporator split

The Condenser Outlet Split (COS) cycle is represented in Figure 4 where the flow exiting the Condenser/Gas Cooler is split in 2 streams. This allows for 2 evaporation levels with benefits in terms of heat transfer losses in several applications (e.g. HVAC, chilled water, etc.). This latter configuration can be also seen as a combination of the former two layouts.

In order to push south the CO_2 equator, the use of complex system solution (multi-ejector modules, parallel compression etc.) has been studied in recent years. A lot of research and industrial activity on this topic has been conducted (see for instance [4] and [5]) and this is particularly true for supermarket applications where the generous size of the system allows for increase of layout intricacy. Gullo et al. summarized the most recent advancement in the field in [6].

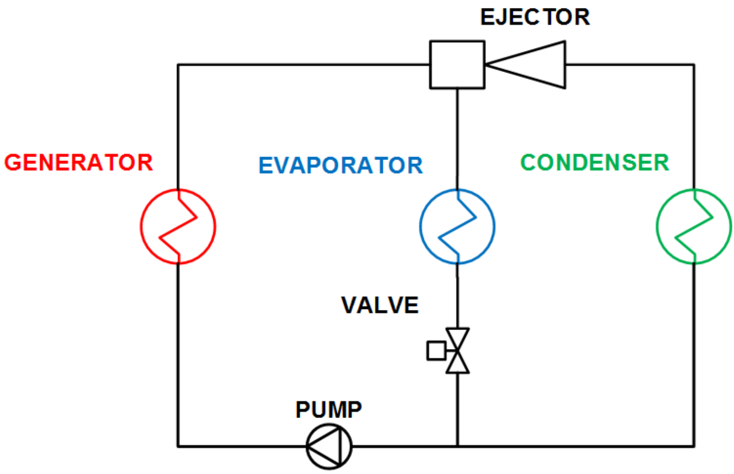

Figure 5 Heat powered steam ejector chiller

From vapor compression system the focus is now moved to heat powered cycles. The layout of a steam ejector chiller is shown in Figure 5, the idea is to use relatively low heat input (90-180°C) at the Generator to subtract heat at the evaporator. The Generator provides the energy input for the vaporization of the working fluid (R718). The high temperature and pressure flow is then expanded in the motive nozzle of the ejector, which entrains the secondary flow from the Evaporator. After the mixing process, the resulting flow is compressed at the intermediate pressure of the Condenser. Finally, the condensed flow is split in 2 streams. The first is pumped back to the Generator pressure, while the latter passes through the throttling valve before the Evaporator. By looking at the typical P-h diagram of a steam ejector chiller in Figure 6 one can easily notice a motor cycle and a refrigeration cycle combined and coupled together by means of the ejector, which is the actual compressor of the cycle. This kind of system becomes particularly convenient when

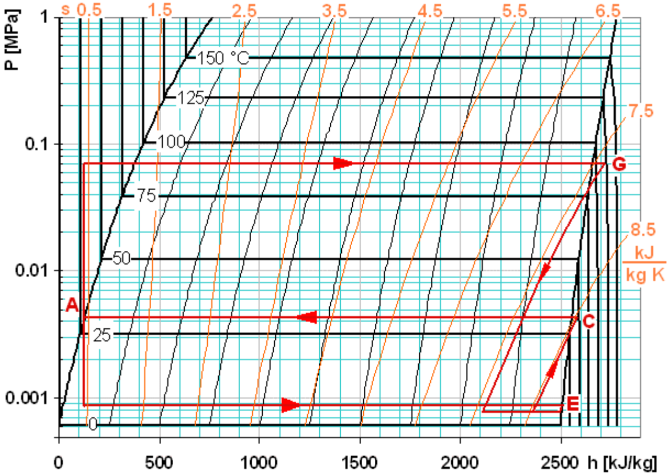

Figure 6 Ideal P-h diagram of steam ejector chiller

steam is already available in the industrial process and can be directly used (without a proper steam generator). The system is also oil-free and, since there is no volumetric compressor, the well-known low volumetric capacity of water/steam systems is not a problem in this application. On the other hand, the main drawback is its relatively low efficiency compared to its main competitor: absorption chiller [7].

In order to improve the efficiency of both CO_2 and steam refrigeration systems, the development of tools capable to predict and optimize the performance of the ejector are necessary.

The main goal of the thesis has been conducted in the implementation and validation of novel CFD models for supersonic two-phase ejector that can be used for analysis and optimization of these key components in the field of refrigeration with natural fluids. The developed tools have also the benefit to be easily adaptable to different fluid and different applications.

1 Chapter 1

In this chapter the basics of ejector physics will be discussed. Details about the single- and two-phase phenomena will be addressed in the following sections.

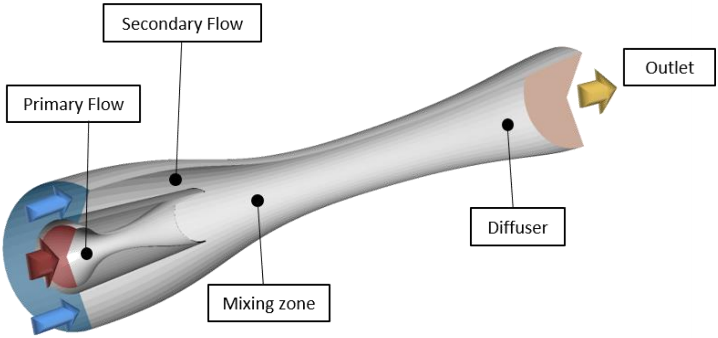

Figure 7 Ejector layout

As shown in Figure 7, the layout of the ejector can be schematized in different areas: motive nozzle, suction nozzle, mixing chamber and diffuser. When the profile of the ejector has a continuous shape the distinction of the different zones is not straightforward but, from a didactic point of view, it is useful to decompose the main flow features of the ejector in different zones. The flow features in a supersonic ejector can be complex and challenging to study. An example of a density gradient contour of the flow one can expect in an ejector is represented in

Figure 8. The supersonic flow exiting the motive nozzle as well as the shock train in the diffuser are clearly visible. Such a behavior, typical of supersonic wall bounded jets, will be explained and commented in further sections.

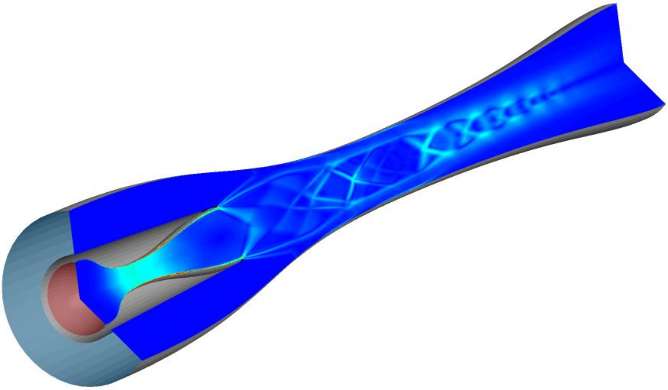

Figure 8 Numerical Schlieren photography (density gradient contour) of the flow inside a supersonic ejector.

1.1 Jet Physics

The flow behavior in the ejector is driven by the expansion in the motive nozzle, which leads to a supersonic flow exiting the nozzle, in most of the cases. If the motive nozzle is not perfectly

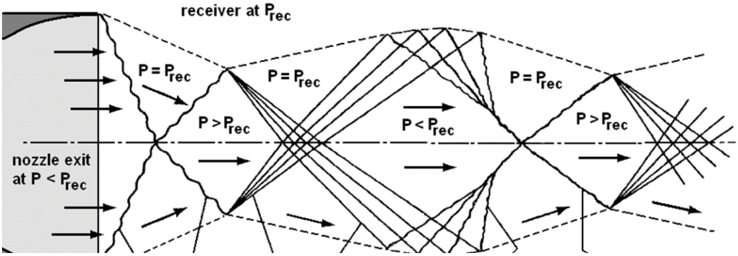

Figure 9 Flow exiting a nozzle in over expanded condition [9]

designed, the expanded motive flow could have a static pressure which differs from the pressure of the mixing zone of the ejector, which is very close to the suction flow pressure. If, for instance, the suction pressure is higher than the design pressure, the supersonic flow will experience a shock downstream the nozzle throat [8]. From a theoretical point of view, the shock can be seen as an adiabatic process of zero thickness causing a temperature and entropy increment [9]. By increasing the receiver (or secondary flow) pressure, as shown in Figure 9, the normal shock moves towards the nozzle throat. For intermediate receiver pressure, the shock becomes conical and it moves downstream the nozzle exit plane (NXP). As a result of the oblique shock-wave, the flow decelerates remaining in supersonic conditions. However, as the ejector axis behaves like an impermeable wall, the flow that converges towards the axis, if supersonic, will originate another oblique shock that produces a further pressure increase [9]. At this point the pressure difference between the flow core and the surrounding gives rise to a typical Prandtl-Meyer expansion starting at the oblique shock-wave limit. The expansion fan is reflected at the jet axis as well.

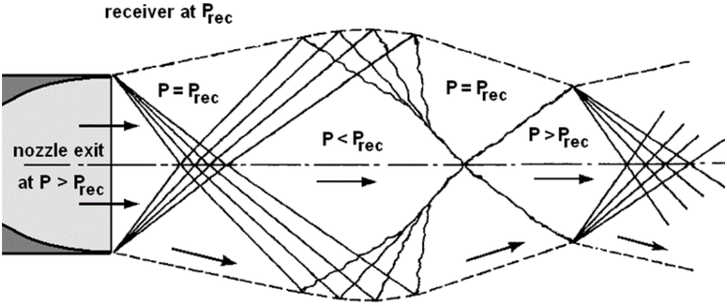

Figure 10 Flow exiting a nozzle in under expanded condition [9]

Therefore, the often cited mechanism that sees the primary nozzle to expand the fluid down to very low pressure in order to produce a “suction” for the secondary flow, in the case of supersonic ejectors, is oversimplified and misleading [8]. When the nozzle has an exceedingly high pressure ratio between the throat and the exit cross sections, it is said to be “over-expanded” and its effectiveness is partially reduced by the irreversibility connected to the shock-waves. This was clearly shown by Mazzelli and Milazzo in [10].

If the pressure of the flow exiting the nozzle is lower than the suction pressure, then Prandtl-Meyer expansion fans will originate from the nozzle trailing edge. This behavior is shown in Figure 10 and, in this case, the nozzle is said to be “under-expanded”.

This first analysis of the flow behavior holds true, with some modifications, for the two-phase ejectors as well, with the presence of the classical “expansion diamonds” structure.

1.2 Diffuser Physics

Another typical flow feature of the ejector is the shock train occurring in the diffuser zone. Generally speaking one of the most important factor of influence for a supersonic channel flow is its interaction with the viscous boundary layer [11]. This latter becomes unstable in diverging ducts, where the pressure is increasing in the flow direction, causing a tendency to separation [12].

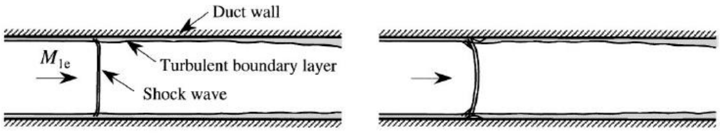

(a) Normal shock wave ($1.0 < M_{1e} < 1.2$)

(b) Curved shock wave ($1.2 < M_{1e} < 1.3$)

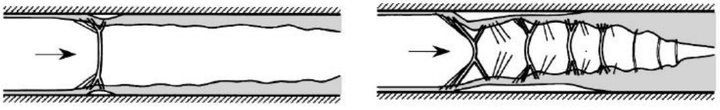

(c) Bifurcated shock wave ($1.3 < M_{1e} < 1.5$)

(d) Shock train ($1.5 < M_{1e}$)

Figure 11 Shock trains and boundary layer interaction [11]

Figure 11 depicts what happens in a constant area duct as the Mach number upstream the shock train is increased. At relatively low Mach number, one can notice the presence of a normal shock-wave with a negligible interaction with the walls. At higher Mach number, separation of the flow in proximity of the wall may occur. When the Mach number is even higher, the shocks begin to bifurcate and the interaction with the boundary layers is progressively more intense. This behavior has been experimentally observed several times, as an example the reader is referred to [11] and [13]. The presence of shock and expansion waves of the flow exiting the motive nozzle and the typical shock train in the diffuser affect the ejector performance and must be taken into account in the design and optimization of the ejectors.

1.3 Performance Parameters

Because of the difficulty in the detailed local analysis of supersonic flows, the main performance parameters used to compare the ejector performance are mainly based on global quantities. The first parameter is the entrainment ratio (Equation (1.1)), i.e. the ratio between the suction nozzle mass-flow rate and the motive nozzle mass-flow rate.

$$ER = \frac{\dot{m}_{SN}}{\dot{m}_{MN}} \tag{1.1}$$

The pressure lift of the ejector is defined in Equation (1.2) and is the difference between the ejector outlet pressure and the suction nozzle inlet pressure. It is used as an alternative of the pressure ratio (Equation (1.3)), which is the ratio between the outlet pressure and the suction nozzle inlet pressure.

$$P_{lift} = P_{OUT} - P_{SN} \tag{1.2}$$

$$P_{ratio} = \frac{P_{OUT}}{P_{SN}} \tag{1.3}$$

Finally, when it comes to the overall efficiency of the device, several formulations have been proposed over the years. The most used, for flashing ejectors, is the one proposed by Elbel and Hrnjak [14] which is presented in Equation (1.4). It is a single parameter that accounts for mass entrainment ratio effects and pressure lift effects. It represents the actual work recovered by the ejector, divided by the theoretical maximum recoverable work. The recovered work is calculated as the power used in an isentropic compression of the suction flow till the outlet pressure. The maximum recoverable work is defined as the work of an isentropic expansion of the motive stream to the outlet pressure.

$$\eta = \frac{\dot{W}_{rec}}{\dot{W}_{MAX,\, rec}} \tag{1.4}$$

It is worth to note that this definition is valid only for flashing ejector and it is not a univocal formulation. Moreover, it should be emphasized that a maximization of the ejector efficiency does not necessarily results in an optimization of the overall system Coefficient of Performance (COP) [15].

In the case of condensing ejectors, a commonly accepted efficiency formulation is not available. In this case the entrainment ratio plays a key role in the determination of the overall COP. By looking at Equation (1.5) one can immediately see that the COP of the system is optimal at highest possible entrainment ratio.

$$COP_{real} = \frac{\dot{Q}_c}{\dot{Q}_G + \dot{W}_{pump}} = ER \cdot \frac{h_{Evaprator\ Out} - h_{Condenser\ Out}}{h_{Generator\ Out} - h_{Condenser\ Out}} \tag{1.5}$$

1.4 Ejector Operation

Since in heat powered refrigeration cycles the pressures and temperatures at the boundaries of the ejector are easier to control, many examples of detailed operating curves are available in the literature. By keeping fixed the conditions at both generator and evaporator, while varying the outlet (Condenser) pressure, one obtain one of the curves of Figure 12. The operation mode of the ejector is divided in 2 main regions. The double chocked condition is when the condenser pressure is lower than critical pressure and the flow is chocked in both motive nozzle and diffuser. In this case the entrainment ratio (and the system COP) remain constant. The *critical pressure* is, by definition, the higher condenser pressure that allows a double chocking operating mode.

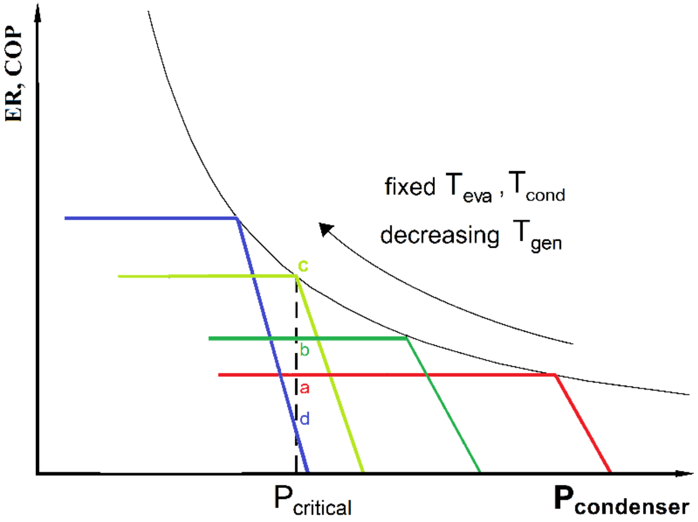

Figure 12 Operating curves at fixed evaporator temperatures and varying generator temperature [7]

When the condenser pressure goes above the critical pressure, the entrainment ratio decreases as well as the COP. Several curves can also be obtained at different generator and/or evaporator temperatures. Despite it is the most common way to describe the operation of heat powered cycle ejectors and the same conclusion are, in principle, valid for any ejector, the problem with flashing ejectors in VCC is a bit more complex. Using ejectors to recover the throttling loss in a transcritical vapor compression cycle, does not allow for a precise control of the pressure and temperatures at the outlet of the ejector. Therefore, such an operating curve is difficult to reproduce experimentally. Moreover, since there is not a direct connection between the ejector efficiency and the system COP, any attempt to maximize the component efficiency could reduce the performance of the system. In this case, the ejector should fit the required values of entrainment ratio and pressure lift that allow for the best possible COP. However, as shown in [15], this may not correspond to the highest value of component efficiency, as above defined in Equation (1.4).

1.5 Non-equilibrium Phase Change

The condition of equilibrium phase change is an idealization of real flows with mass transfer occurring between the phases. Such an assumption may give satisfactory results in some applications, especially when the flow speed is quite low. For the large majority of high-speed flows, the effects of non-equilibrium phase change are often of primary importance. A brief introduction on non-equilibrium phase change is necessary in order to understand the physics of this kind of flows.

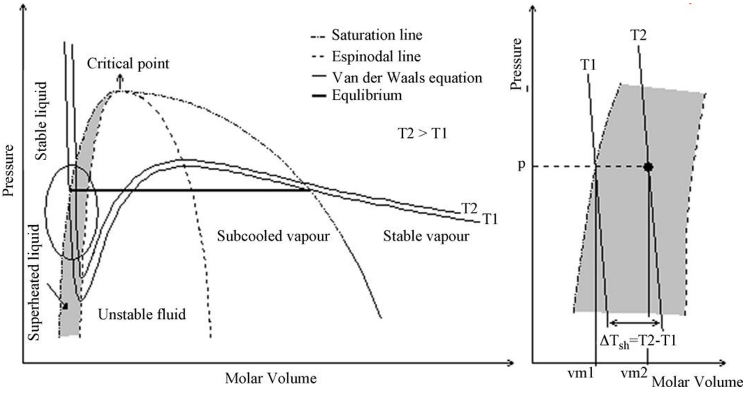

Figure 13 Typical P-v diagram of metastable flashing flow with insert showing the superheating of the liquid phase [16]

The explanation of metastable state behavior will be given for flashing flow but the same holds true for condensing flows as well. The metastable condition of superheated liquid is when the liquid temperature is higher than its boiling temperature (at the local pressure) [16]. In fact, any perturbation of the fluid state may cause the occurrence of the phase change. This is shown in Figure 13, where $\Delta T_{SH} = T - T_{SAT}$. The figure, from the review of Polanco et al. [16], shows a P-v diagram with two Van der Waals equation of state isothermals, referring to temperatures T_1 and T_2. By increasing the specific volume of the system at constant temperature the Van der Waals equation predicts that the fluid passes through a minimum of pressure and then a maximum before decreasing steadily at higher values of specific volume [17]. This is the case when the temperature is below the critical temperature T_C. It can be easily shown that in the region between the minimum and the maximum of pressure the requirements of intrinsic stability are not satisfied and the behavior of real system deviates from the states predicted by Van der Waals equation. This well-known Equation of State (EOS) was used as an illustrative example, however the same can be concluded with any other EOS of the third order. Figure 13 also underlines the two curves denoting the limits of phase stability: liquid and vapor spinodal limits. It is well known that liquid state can be superheated and vapor state can be supercooled (or supersaturated) without a phase transformation occurring. These conditions are known as metastable states and all the possible metastable states lie within the area between saturation and spinodal curve. The behavior suggested by the Van der Waals EOS is, at least qualitatively, close to the behavior of two-phase systems.

1.6 Two-phase Speed of Sound

Another challenging topic is the formulation of the speed of sound of two-phase flows. This fundamental parameter is difficult to measure for real flows and its formulation is not univocal since it depends on the topology of the flow itself. In most of the cases one has to rely on approximated formulation or correlations to estimate the local Mach number in a two-phase system. The Mach number is defined as the ratio between the velocity and the local speed of sound. For single phase flows in converging-diverging nozzles, it is important in the determination of the chocked condition (i.e. Mach number unity at the nozzle throat). On the other hand, the determination of chocking section in a two-phase nozzle with non-equilibrium phase-change is not straightforward. When the interfacial exchange processes are sufficiently slow, compared to the characteristic time of the flow, the equality of velocity and local speed of sound does not occur in correspondence of the nozzle throat anymore. The "effective" passage area reaches its minimum further downstream [18]. A sketch of this phenomena and the plot of pressure and Mach number are represented in Figure 14, where the effect of non-equilibrium phase-change are also shown. The exact position of this section can only be determined by integrating the full set of flow equations from the nozzle inlet to the chocking section itself [18].

For single phase flows the speed of sound is defined with Equation (1.6).

$$a^2 = \left(\frac{\partial P}{\partial \rho}\right)_s \tag{1.6}$$

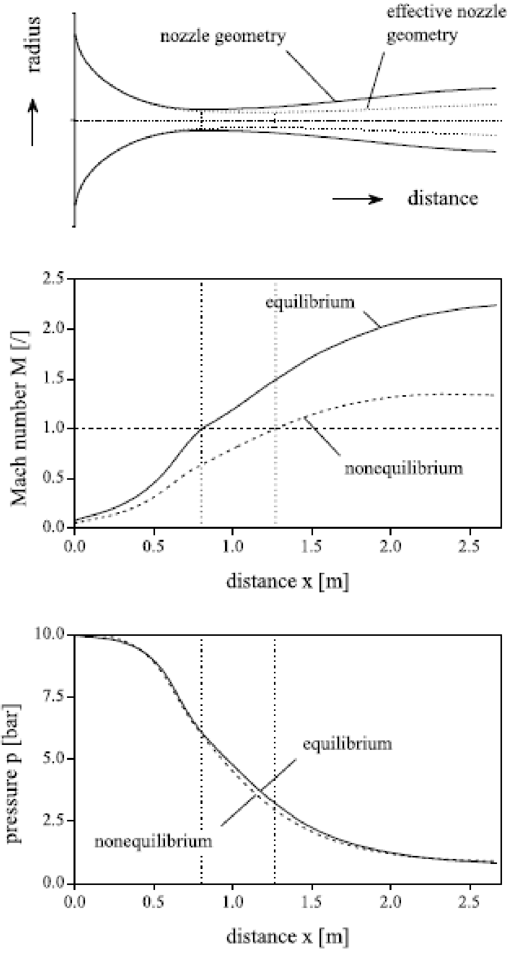

Figure 14 Two-phase flow in convergent-divergent nozzle with effects of non-equilibrium conditions [18]

With two-phase mixture and, in particular, with phase changing fluids the sound speed is difficult to determine. With an opportunely simplified set of Navier-Stokes Equations (NSE) for two-phase flows and by calculating the eigenvalues of the coefficients matrix, one can obtain simplified formulations. For instance, under the hypothesis of non-homogeneous flow conditions (i.e., the velocity of the phases are different) but with neglected influence of surface tension (i.e., the phases share the same pressure) one can analytically derive the formulation of Equation (1.7) for the two-phase speed of sound [18].

$$c = \sqrt{\frac{\alpha_g \rho_l + \alpha_l \rho_g}{\frac{\alpha_g \rho_l}{c_g^2} + \frac{\alpha_l \rho_g}{c_l^2}}} \qquad (1.7)$$

Where the subscripts g and l refer respectively to gas phase and liquid phase properties and *c* is speed of sound. The difference between liquid and vapor velocities, also known as slip-velocity, has an impact on the two-phase speed of sound. In particular, the sound speed is reduced by increasing the slip-velocity. This effect is reduced (and often neglected) if the order of magnitude of the slip-velocity is lower than the one of the speed of sound [18]. Another noteworthy formulation is the one derived under the assumption of homogeneous flow with thermal non-equilibrium between the phases. In this case, the liquid and gaseous phases share the same pressure and velocity. The resulting sound speed formulation is shown in Equation (1.8) [18].

$$c = \sqrt{\frac{1}{\frac{\alpha_g \rho}{c_g^2 \rho_g} + \frac{\alpha_l \rho}{c_l^2 \rho_l}}} \tag{1.8}$$

This is also known as Wallis equation [19] and is widely used in the computation of multiphase compressible flows [20].

A different approach for the derivation of a formulation for speed of sound of two-phase flows with phase change can be found in [21]. An infinitely homogenized mixture of liquid and vapor is considered. The real behavior of such a multiphase flow lies in between a *homogeneous equilibrium model* (phases in thermal equilibrium) and a *homogeneous frozen model* (zero heat transfer between the phases). The formulation has these two extremes cases as boundaries and a limited amount of heat transfer is assumed to occur between the phases. This is modeled by considering an interactive portion of each phase (ε) which instantaneously exchanges heat with the corresponding interactive portion of the other phase. The remaining portions are assumed to be perfectly insulated. If ε of both phases is equal to 0 one obtains the *homogeneous frozen model*; else if ε approaches unity, one obtains the *homogenous equilibrium model.* The resulting formulation is shown in Equation (1.9) [21].

$$\frac{1}{\rho c^2} = \frac{\alpha_l}{p}[(1-\varepsilon_l)f_l + \varepsilon_l g_l] + \frac{\alpha_v}{p}[(1-\varepsilon_v)f_v + \varepsilon_v g_v] \tag{1.9}$$

Where f and g are functions of the thermodynamic properties of the phases and the subscript l and v refer to liquid and vapor quantities, respectively. Some approximations can be done for practical flows and some experimentally obtained correlations for f and g are also available for some fluids (for instance H_2O and CO_2). The possible simplifications will be further discussed in the following sections.

From a physical point of view, the speed of sound of a two-phase mixture is lower than the saturated phases sound speeds. This behavior is reproduced by all the presented formulations, more details and wider analysis can be found in [19], [22] and [23] to cite some. Figure 15 shows the typical trend for Equation (1.9) in the two-phase domain. The saturated phase sound speeds are represented by the blue dots. It is worth to note that this equation has a mathematical discontinuity for low vapor volume fractions, so this had to be limited in its practical implementations within CFD models.

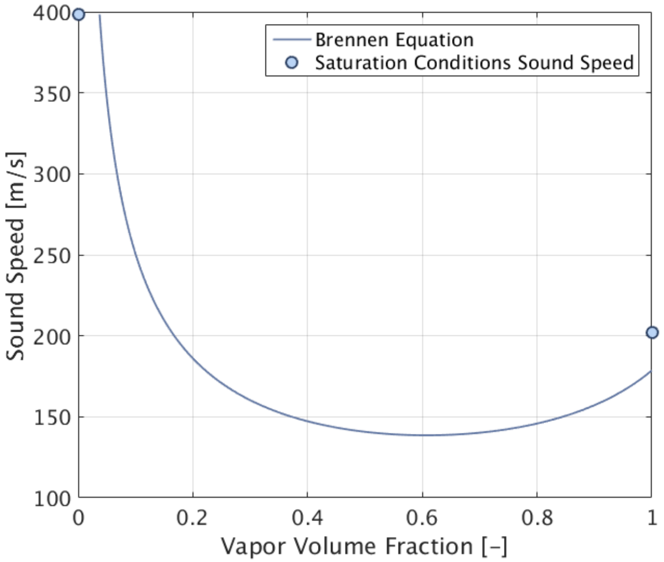

Figure 15 Brennen equation for two-phase sound speed at constant pressure

2 Chapter 2

The part of the thesis involving CFD computations of wet-steam flow will be described in this Chapter. After a brief description of the physics of condensing steam and the computational modeling, the obtained results are presented. The results shown in this chapter have been published in [24], [25], [26] and [27].

2.1 Wet-Steam Flow

Non-equilibrium condensation of steam occurs in many jet and turbomachinery devices, such as supersonic nozzles, and across low pressure stages of steam turbines. Normal operation of these devices involves flow expansions which leads to states that are well within the saturation dome. In the ideal case of a reversible transformation, the attending condensation process would follow a path of equilibrium states, and no losses occur. In real conditions, the very limited residence time and high cooling rates lead to a substantial departure from the equilibrium state. As the steam rapidly expands inside a nozzle or blade vane, thermodynamic equilibrium is not maintained and, at a certain degree of expansion, the vapor state collapses and condensation takes place abruptly as a shock-like disturbance. This is generally called the “condensation shock” [28]. This sudden change of state of aggregation leads to an instantaneous and localized heat release that increases the pressure and temperature and reduces the Mach number [28]. Moreover, the condensation shock implies large gradients between the phases that cause irreversibilities and, downstream the condensation shock, the flow contains a considerable number of tiny liquid droplets (of the order of $10^{19}/\mathrm{dm}^3$, [29]) that can interact in non-trivial ways with shock waves and turbulent structures. A reliable CFD scheme should be able to account for all these effects. In the past decades, several methods have been devised to simulate wet steam flows, with different levels of complexity and accuracy. The simplest and perhaps most used is the so-called "single-fluid" approach. This is basically a fully Eulerian method that solves the continuity equation for both phases separately, whereas the momentum and energy equations are computed for the average properties of the mixture. In addition, a further transport equation is needed to describe the conservation of the number of droplets in the unit volume. This method is commonly employed by commercial codes (e.g. ANSYS Fluent or CFX) and has been used by several research teams [24] [30] [31].

Although commercial codes dispense from developing complex in-house solvers, the use of wet-steam built-in models generally does not allow much freedom in the change of the physical parameters and settings. The work presented in this chapter is an attempt to overcome this limitation through the development of a customized model within a widely used CFD commercial code (ANSYS Fluent, [32]). This approach has the double benefit to allow great flexibility in the choice of the physical model setting (especially for phase change and phase interaction models) and, at the same time, to exploit the capability of the commercial software in terms of selection of algorithms and solver settings.

To date, CFD simulations of wet-steam flows have proved to achieve a quite good agreement for the steam condensation within transonic nozzles [33] and steam turbines [34] [35], both in terms of pressure and droplet size trends. However, the same may not hold true in ejector applications where the interaction between droplets, shocks and shear layers may introduce many unpredictable effects. In this respect, most of the numerical studies on condensing steam ejectors have been accomplished through single-phase, ideal-gas simulations (e.g. [36]) and very few examples of CFD using wet steam models exist (see for instance [30] [37]).

The developed scheme is based on a single-fluid approach (*Mixture model and Eulerian-Eulerian model*). The validation of the model is made by comparing the simulation results against two different experimental test-cases, the converging-diverging nozzle from Moses and Stein [38] and the supersonic steam ejector studied by Al-Doori [39] and Ariafar *et al* [30], who provide data for both mass flow rates and wall pressure profiles. In order to assess the effects of non-equilibrium phase change, the results have also been compared with a HEM implemented in ANSYS Fluent. The details of this latter model and its implementation in the commercial code will be explained in the next section.

2.2 Preliminary Analysis

This section represents a first attempt to overcome all or some of aforementioned limitations connected to the use of design methods unable to account for condensation effects in steam ejectors. To this aim, the CFD model that includes a non-equilibrium condensation model is tested in order to assess and refine the performances of a first ejector design concept with a continuous profile designed with a 1D model procedure in [31]. The results obtained with the standard implementation of the wet-steam model in ANSYS Fluent were compared against HEM. This latter is an Eulerian model capable to study equilibrium phase change. Due to its simplicity it can be used as a valid approach to obtain results in a preliminary stage of the ejector designing process. Its main limitations can be summarized as follows:

- Phases in mechanical equilibrium, i.e., they have the same velocity;
- Phases in thermodynamic equilibrium, i.e., they have the same temperature;
- No possibility to account for metastability affects.

In particular, this last approximation may lead to significant errors due to the high speed that occurs within supersonic ejectors. This point is studied in details in Chapter 2 and Chapter 3.

The implementation of the HEM in ANSYS Fluent can be done by simulating a fluid with mean properties between liquid and vapor, as a function of pressure and static enthalpy [J/kg]. The default Energy equation in ANSYS Fluent is replaced with a user defined scalar transport equation where the only unknown variable is the specific enthalpy:

$$\nabla \cdot \left(\rho \tilde{\boldsymbol{u}} \tilde{h}\right) = \nabla \cdot \left(\Gamma_{h,eff} \nabla \tilde{h}\right) + \dot{S}_{h1} + \dot{S}_{h2} + \dot{S}_{h3} \qquad (2.1)$$

$$\dot{S}_{h1} = \tilde{\boldsymbol{u}} \cdot \nabla \bar{p} \qquad (2.2)$$

$$\dot{S}_{h2} = (\mu + \mu_T)\left\{2\left[\left(\frac{\partial \tilde{u}}{\partial x}\right)^2 + \left(\frac{\partial \tilde{v}}{\partial y}\right)^2 + \left(\frac{\partial \tilde{w}}{\partial z}\right)^2\right] + \left(\frac{\partial \tilde{u}}{\partial y} + \frac{\partial \tilde{v}}{\partial z}\right)^2 + \left(\frac{\partial \tilde{u}}{\partial z} + \frac{\partial \tilde{w}}{\partial x}\right)^2 + \left(\frac{\partial \tilde{v}}{\partial z} + \frac{\partial \tilde{w}}{\partial y}\right)^2 - \frac{2}{3}(\nabla \cdot \tilde{\boldsymbol{u}})^2\right\} - \frac{2}{3}\bar{\rho}K\nabla \cdot \tilde{\boldsymbol{u}} \tag{2.3}$$

$$\dot{S}_{h3} = -\rho\tilde{\boldsymbol{u}} \cdot \nabla K \tag{2.4}$$

Where (~) and (-) denote Favre- and Reynolds-averaged quantities, ***u*** is the velocity vector and *u, v, w,* are its components. ρ is the local density, μ and μ_T are the molecular and turbulent viscosity, respectively. $\Gamma_{h,eff}$ is the effective diffusion coefficient, which represents the sum of the molecular and turbulent thermal diffusion coefficients. As for the fluid properties, these have been implemented as follows:

- density defined via User-Defined Function (UDF) as a function of pressure and specific enthalpy;
- speed of sound defined via User-Defined Function (UDF) as a function of pressure and specific enthalpy;
- Average vapor phase value for the molecular viscosity and molecular diffusion coefficient.

The last assumption is practically equivalent to consider “dry walls” due to the heat recovery in the boundary layer (due to the high turbulence levels, the molecular diffusion and viscosity affects only the dynamics of the viscous sub-layer).

The introduction of the sound speed formulation is required by ANSYS Fluent to solve the pressure-correction equation [32]. Unfortunately, formulation of the two-phase speed of sound are not available within REFPROP libraries [40]. Therefore, in the two-phase region, the sound speed has been calculated by means of the Wallis equation [19], explained in the previous chapter. From a numerical point of view, both density and sound speed are calculated by means of lookup-tables constructed by developing an in-house MATLAB [41] code that automatically generates the fluid property matrices by acquiring data from REFPROP libraries. The tables are loaded in the Random Access Memory (RAM) of the computer or computational cluster before the start of the calculations. At runtime, the CFD solver operates a bi-linear interpolation (with pressure and specific enthalpy as independent variables) to obtain the correct value of density and sound speed in each cell of the computational domain.

It is worth to remark the main drawback of this numerical model. Because of the limitations in the implementation of a scalar transport equation in place of the standard energy equation, the use of only one unknown variable is allowed [32]. As shown by Smolka et al. [42], who firstly derived the equation, this can be done by eliminating the temperature gradient term of the energy equation by means of the following simplification:

$$\nabla \cdot (k \nabla T) = \nabla \cdot (\Gamma \nabla h) - \nabla \cdot \left(\Gamma \underbrace{\left(\frac{\partial h}{\partial p}\right)_T}_{\approx 0} \nabla p \right) \qquad (2.5)$$

In principle, this assumption is valid for Ideal Gas only and, as remarked by Lucas et al. [43], this simplification may lead to unphysical heat fluxes between the phases, even in case they are in thermal equilibrium. However, the group of Prof. Smolka at the Silesian University of Technology have performed a wide validation of HEM and HRM (Homogeneous Relaxation Model) for CO_2 ejectors, both based on this energy equation formulation. For details, the reader is referred to [44] and [45]. Because of the low computational cost of the HEM model, it was widely used for optimization of ejectors [46] [47] and, more recently, Haida et al. [45] also validated the HRM model for heat transfer applications.

The wet-steam model, as already mentioned, is a Eulerian homogenous model available in several commercial CFD codes. The model considers the condensed phase as monodispersed in the vapor phase and the transport equations are written for the whole mixture. A more detailed description of the model will be given in the next chapter, where the standard implementation in ANSYS Fluent will be compared with the new mixture-model developed.

The computational domain is two-dimensional and axi-symmetric, the mesh is composed of approximately 45000 quadrilateral elements and is wall resolved, see Figure 16. The solver adopted for the Wet-Steam calculations is a density-based solver while in case of the HEM approach the solver is pressure-based with a pressure-velocity coupling. Calculations are second order accurate and a k-ω SST turbulence model is selected in all cases because it was seen to give good results in previous ejector studies [48]. The boundary conditions at the inlets are summarized in Table 1. The inlets pressures are the saturation pressures corresponding to T_{SAT} and they are maintained as constants for various outlet pressures.

Table 1 Boundary conditions at both inlets

	T_{SAT} [°C]	T_{SH} [°C]
Primary Inlet	80	1
Secondary Inlet	7	0

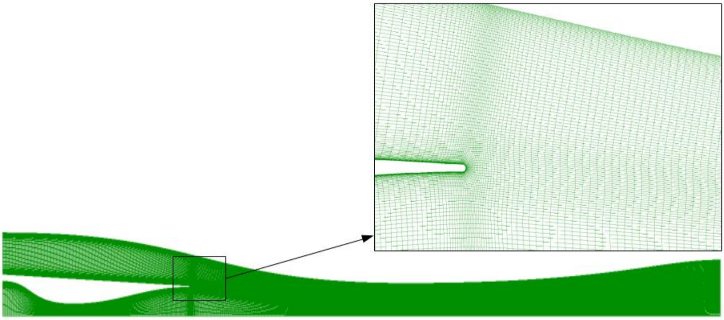

Figure 16 Computational mesh with detail near the motive nozzle fillet [31]

Figure 17 shows a comparison of the entrainment ratio between the Wet Steam (WS) and the HEM, where the HEM predicts a higher value of this quantity.

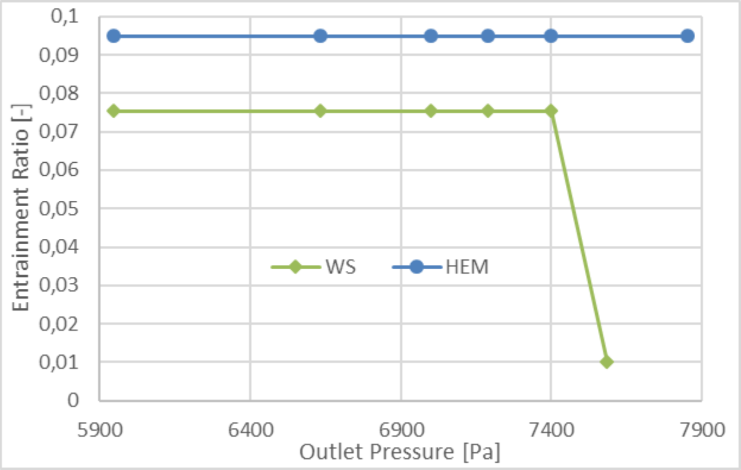

Figure 17 Entrainment ratio of the ejector for different outlet pressures

The mismatch is connected mainly to differences in the prediction of the velocity profiles at the Nozzle Exit Plane. In turn, these are most likely due to the different equation of state and fluid properties (and in particular, the heat capacity ratio) which causes different expansion levels and results in different mass flow rates in the nozzle throat.

Figure 18 shows the variation of density along the nozzle axis. The throat region is highlighted in red in order to show that the density differences are almost negligible at this point, thus confirming that the mass flow rate discrepancies are mostly affected by velocity trends. Right downstream the throat region a clear mismatch in the density profiles is visible. The main reason for this has to be found in the WS model capacity to account for metastability effects, which results in the aforementioned "condensation shock". As can be seen, this leads to an abrupt variation of density during the phase change process, as opposed to the gradual variation of the HEM.

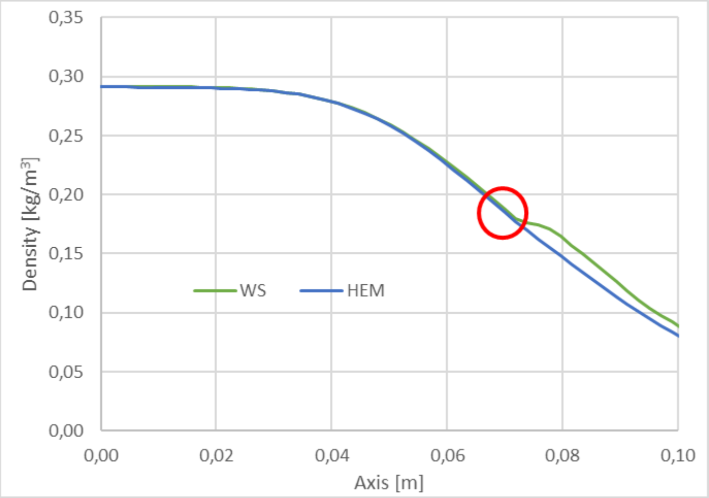

Figure 18 Comparison of density trends along the axis (the red circle highlights the nozzle throat region)

Figure 19 shows the quality contours inside the ejector obtained with both models. Clearly, the HEM overestimates the variations of quality with respect to the WS model. Due to the assumption of thermodynamic equilibrium, the HEM model gives rise to instantaneous quality variation that follows the compressions and expansion patterns in the mixing chamber. On the other hand, the Wet Steam model accounts for the time dependency of the condensation process (i.e., relaxation time), hence, the shocks have a lower impact on the quality (and, of course, on the other flow variables). This difference in the model behavior results in significant discrepancies in the pressure profile along the axis, as shown in Figure 20. In other words, the relaxation time included within the WS model acts as a damper in the shock/expansion processes that occur all along the ejector length.

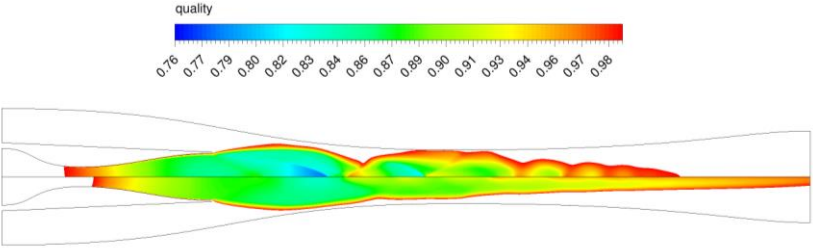

Figure 19 Contours of quality; HEM top, WS bottom

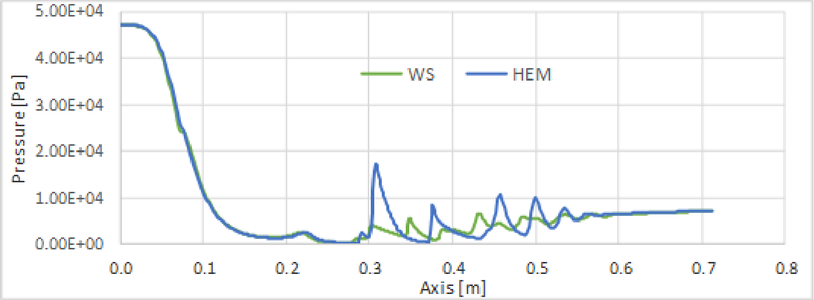

Figure 20 Comparison of pressure trends along the axis

Figure 21 shows a comparison of the temperature results along the axis. In the case of Wet Steam model the temperature goes well below the HEM results. This is again due to the absence of a relaxation time of HEM: due to the higher variation of the quality, the condensing mass is generally higher in HEM, thus resulting in higher latent heat transfer and higher temperatures. Most interestingly, looking at the WS profile of both vapor and liquid phase one can see that the temperatures go well below the Triple Point temperature (273.15 K) in some regions downstream the nozzle exit, meaning that there are some possibilities of ice formation inside the ejector.

It is worth to note that the temperature of the liquid phase for the WS are very close to that of the HEM model. This is probably due to the fact that the Fluent WS model assumes the liquid temperature to be the equilibrium saturation temperature at the vapor pressures. Therefore, whenever the pressure differences between the two models are small, the two temperatures are close to each other (this is true as long as the system is two phase).

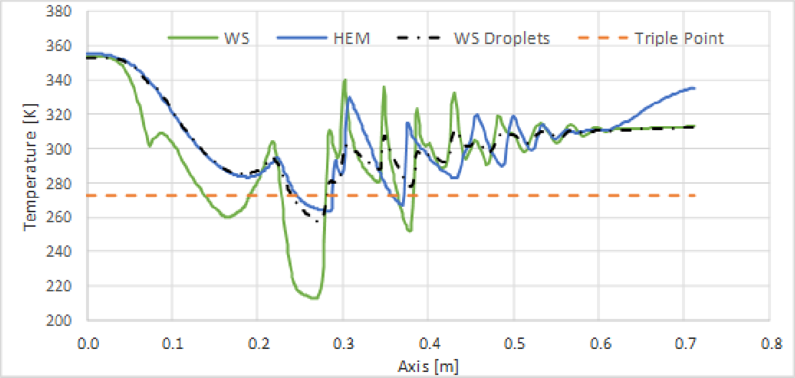

Figure 21 Comparison of temperature trends along the axis

A first attempt to compare two different methods and approaches for the simulations of multiphase flows in steam condensing ejector has been performed. A Homogeneous Equilibrium Model and the standard Wet-Steam model implemented in the commercial code ANSYS Fluent. The results show a general tendency of the HEM to overestimate the variations of the main quantities during the shock/expansion process occurring in the ejector.

2.3 Nozzle test-case

Both a Mixture-model and a full Eulerian-Eulerian-model have been developed and validated for a condensing steam flow. Since, for numerical stability reasons, the Mixture-model was found to perform better in full ejector applications, the set-up of the Eulerian-Eulerian model will be only commented in Section 2.8.

The conservation equations for mass, momentum and energy are written for the average mixture fluid and assume the form of the conventional Navier-Stokes equations for compressible flows:

$$\frac{\partial \rho_m}{\partial t}+\frac{\partial \rho_m u_{mj}}{\partial x_j}=0 \qquad (2.6)$$

$$\frac{\partial \rho_m u_{mi}}{\partial t}+\frac{\partial \rho_m u_{mi} u_{mj}}{\partial x_j}=-\frac{\partial p}{\partial x_j}+\frac{\partial \tau_{ij\_eff}}{\partial x_j} \qquad (2.7)$$

$$\frac{\partial \rho_m E_m}{\partial t}+\frac{\partial \rho_m u_{mj} H_m}{\partial x_j}=\frac{\partial q_{j\_eff}}{\partial x_j}+\frac{\partial u_{mi} \tau_{ij\_eff}}{\partial x_j} \qquad (2.8)$$

In Equations (2.6), (2.7) and (2.8) the properties of the mixture are described by means of mass or volume weighted averages:

$$\varsigma_m = \beta\varsigma_l + (1-\beta)\varsigma_v \tag{2.9}$$

$$\chi_m = \alpha_l\chi_l + (1-\alpha_l)\chi_v \tag{2.10}$$

where ς_m represents mixture thermodynamic properties like enthalpy, entropy, total energy, etc…, χ_m is the mixture density, molecular viscosity or thermal conductivity, β is the liquid mass fraction and α_l is the liquid volume fraction. The connection between these last two quantities is straightforward:

$$\beta = \frac{m_l}{m_l + m_v} = \frac{\alpha_l\rho_l}{\alpha_l\rho_l + (1-\alpha_l)\rho_v} \tag{2.11}$$

The evaluation of the mixture speed of sound requires special considerations [19], and is calculated here by means of the Wallis Equation (see previous chapter). Two additional equations for the conservation of the liquid mass and the droplets number are coupled with the governing equations for the mixture:

$$\frac{\partial\rho_m n}{\partial t} + \frac{\partial\rho_m u_{mj} n}{\partial x_j} = \alpha_v J \tag{2.12}$$

$$\frac{\partial\rho_l\alpha_l}{\partial t} + \frac{\partial\rho_l u_{mj}\alpha_l}{\partial x_j} = \Gamma \tag{2.13}$$

where "*n*" is the number of droplets per unit mass of the mixture and it is assumed that the two phases move at the same speed (no-slip condition).

The term *"J"* in Equation (2.12) represents the nucleation rate, i.e., the rate of formation of new droplets per unit volume of vapor and is expressed here through the classical nucleation theory (more details can be found in [49]) modified with the Kantrowitz non-isothermal correction [50]:

$$J = \frac{q_c}{(1+\xi)} \frac{\rho_v^2}{\rho_l} \left(\frac{2\sigma}{\pi m^3}\right)^{1/2} exp\left(-\frac{\Delta G^*}{k_b T_v}\right) \tag{2.14}$$

$$\xi = q_c \frac{2(\gamma - 1)}{(\gamma + 1)} \frac{h_{lv}}{RT_v}\left(\frac{h_{lv}}{RT_v} - \frac{1}{2}\right) \tag{2.15}$$

Where q_c is the accommodation factor, h_{lv} is the liquid-vapor latent heat, σ is the liquid water surface tension and ξ is the Kantrowitz non-isothermal correction.

This correction is needed when the rapidity of the nucleation process prevents the two phases from reaching the thermal equilibrium (i.e., $T_L = T_v$). In the case of fast transformations (or low heat transfer rate between the phases) the temperature in the cluster becomes greater than T_v due to the latent heat release. This localized heat release enhances the rate at which the molecules evaporate from the cluster surface and leads to a partial suppression of the critical nucleation rate *J*. The *'Kantrowitz'* correction reproduces this phenomenon and typically reduces *J* by a factor of 50–100 [49].

The term ΔG^* in Equation (2.14) is Gibbs Free energy needed to form a stable liquid cluster (other thermodynamic constants are defined in the nomenclature). Thermodynamic stability considerations lead to a simple expression for ΔG^* [7]:

$$\Delta G^* = \frac{4}{3}\pi r^{*2}\sigma \qquad (2.16)$$

Where r^* is the critical radius of a stable liquid cluster and φ_{ss} is the supersaturation ratio:

$$r^* = \frac{2\sigma}{\rho_l R T_v \cdot ln\varphi_{ss}} \qquad (2.17)$$

$$\varphi_{ss} = \frac{P_v}{P_{sat}(T_v)} \qquad (2.18)$$

Equations (2.14)-(2.18) give the rate at which liquid nuclei spontaneously form within the vapor stream. The presence of the exponential term in Equation (2.14) is indicative of the shock-like nature of the condensation phenomenon. Moreover, it is important to note that all the variables of Equations (2.14)-(2.18) depend solely on the vapor thermodynamic state.

In order to close the set of governing equations, it is necessary to provide a law for the liquid mass generation rate per unit volume of mixture, Γ, in Equation (2.13). This quantity stems from two different sources:

$$\Gamma = \Gamma_{nuc} + \Gamma_{grow} = \alpha_v m_d^* J + \rho_m n \frac{dm_d}{dt} \qquad (\ 2.19\ )$$

where m_d is the mass of a generic liquid droplet and m_d^* is its value when the liquid nucleus first forms. By assuming a spherical shape for all liquid droplets, these are given by:

$$m_d^* = \frac{4}{3}\pi \rho_l r^{*3} \qquad (\ 2.20\ )$$

$$m_d = \frac{4}{3}\pi \rho_l r_d^3 = \frac{\rho_l \alpha_l}{\rho_m n} \qquad (\ 2.21\ )$$

The first of the two terms in the RHS of Equation (2.19) describes the mass generated from freshly nucleated droplets. This term is significant only in the first stages of the condensation process and is rapidly overtaken by the second addendum, Γ_{grow}, which represents the growth or shrinkage of existing droplets. Its expression requires the definition of a droplet growth law. In this work, the formulation derived by Hill following a statistical mechanics approach [29] and later rearranged by Young [51] is used:

$$\frac{dr_d}{dt} = \frac{p_v}{\rho_l h_{lv}\sqrt{2\pi R T_v}} \frac{c_p + c_v}{2} \cdot (T_s(p_v) - T_v) \qquad (\ 2.22\ )$$

Equations from (2.6) to (2.18) form a closed system of equations that can be solved as long as the vapor and liquid equations of state and thermodynamic properties are provided. In this respect, calculations of the non-equilibrium phase-change of steam necessarily requires the description of the fluid properties in metastable conditions, meaning that common tabulated properties cannot be used to this purpose. Unfortunately, there is a serious lack of experimental data for the properties of steam in supercooled conditions, which is regularly testified by reports of the International Association for the Properties of Water and Steam (IAPWS) [52]. Consequently, it is necessary to extrapolate a generic equation of state outside its normal range of validity in order to describe metastable states within the saturation curve.

In the present model, the steam properties are calculated following the work of Young [53] who derived a Virial equation of state truncated at the third term of the expansion:

$$p = \rho_v R T_v \cdot (1 + B\rho_v + C\rho_v^2) \qquad (\ 2.23\ )$$

where B and C are the second and third Virial coefficients. These are functions of the sole temperature and their expressions were calibrated to match steam data in the range between 273.16 and 1073 K. Moreover, formulations for the enthalpy, entropy and specific heats are derived from the Virial equations based on a procedure described by Young [53]. The steam thermal conductivity and dynamic viscosity are given by low order polynomial functions of the vapor temperature obtained from interpolation of NIST dataset [40]. The liquid phase properties (viz., liquid density, specific heat capacity, thermal conductivity and viscosity) are calculated assuming saturation conditions and are again expressed through empirical correlations obtained from NIST [40]. Finally, the water surface tension is a function of the sole temperature and is expressed following Young [51].

The described model has been implemented within the commercial CFD package ANSYS Fluent v18.0 [32]. In this regard, ANSYS Fluent features a built-in Wet Steam model that exploits a specifically developed density based solver. Unfortunately, it is not possible to directly modify the nucleation rate and droplet growth laws of this model according to user defined schemes. Nevertheless, the set-up of a customized scheme is still possible within the framework of Fluent pressure-based multiphase solver by adding a number of User Defined Functions (UDF). Of these, three are needed to input the source terms for the liquid mass fraction and droplet number transport equation and to enforce the expression for the diameter of the droplets. Moreover, a User Defined Real Gas Model is required to implement the virial equation of state and transport properties of the vapor phase. Ultimately, it may be worth to note that, although density-based solvers generally perform better, pressure-based schemes have also been successfully applied for the simulations of multiphase compressible flows with discontinuities (e.g. [20]).

In what follows, the presented numerical model is compared against data from the well-known nozzle test case of Moses and Stein [38]. The results are firstly also confronted with those obtained with the ANSYS Fluent built-in wet steam model in order to benchmark the present scheme with a previously validated code (e.g., [35] [54]). In this comparison, the droplet generation and growth rates equations implemented in the customized model are the same as those featured by the Fluent built-in scheme. Subsequently, the analysis of changes in some of the model settings (e.g., the droplet growth law) is presented.

The computational domain for these simulations has approximately 30000 quadrilateral cells with y+<1 along the nozzle surfaces and is presented in Figure 22. Due to the relative simplicity of the flow field (e.g., absence of pressure shocks), it was possible to set-up a third order accurate QUICK scheme [55] for the spatial discretization of all transport equations. A k-ω SST turbulence model is selected for all simulations.

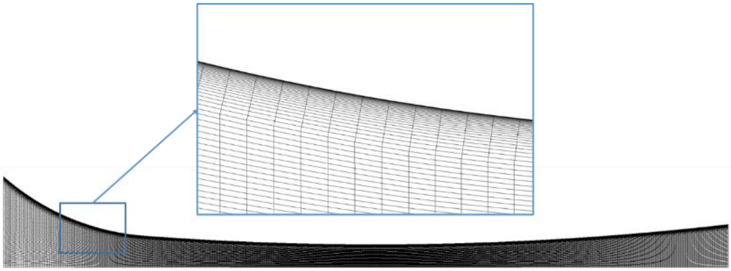

Figure 22 Computational Domain for the nozzle test-case

Simulations are performed for the experiment n. 252, which has inlet total pressure of 40 kPa and inlet total temperature of 101.2 °C [38]. For this test, data on pressure profiles and liquid mass fraction along the axis are available. Results on droplet average radius were not presented in the original paper; however, these were processed by Young [51] starting from light scattering data.

Figure 23 shows the normalized pressure trend along the ejector axis. The figure focuses on the region downstream of the nozzle throat (located at x=8.22 cm from the nozzle inlet) where the condensation shock takes place and experimental measurements are available. Clearly, the presented model overlaps with results from the Fluent built-in model and both seem to capture the pressure trend with reasonable accuracy. When compared to experimental values, numerical results underestimate the general pressure level and the steepness of the pressure rise.

Figure 23 presents also the comparison on the average droplet radii along the nozzle axis. The results show that CFD predicts values that are approximately a half of the experimental. Nevertheless, it is known that for this particular test-case there is a general tendency to under-predict droplet sizes by CFD models [33].

It is interesting to note that the numerical trends for the average radius tend to predict different slope of the curve in the region where the nucleation has terminated. This difference is even more pronounced when comparing the trends for the number of droplets per unit volume of mixture, as shown in Figure 24. The figure clearly shows two different trends of the numerical codes. In particular, the Fluent built-in model predicts the presence of a plateau immediately downstream of the nucleation zone, whereas the developed model shows a decreasing trend in this region.

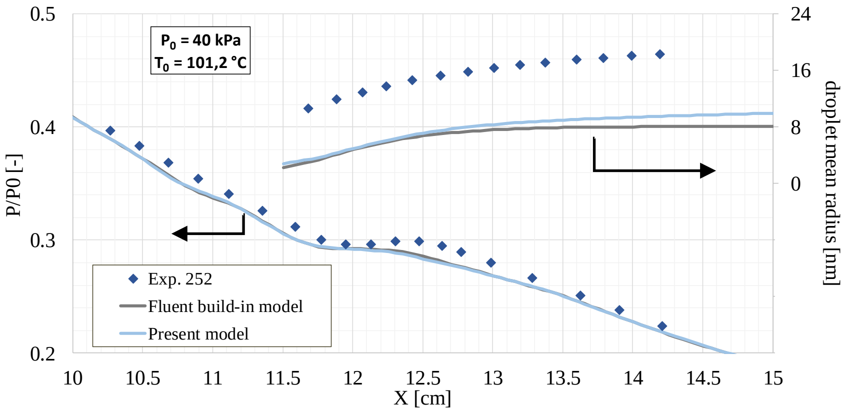

Figure 23 Normalized pressure trend along the nozzle axis (bottom curve) and corresponding droplet average radius (top right curves)

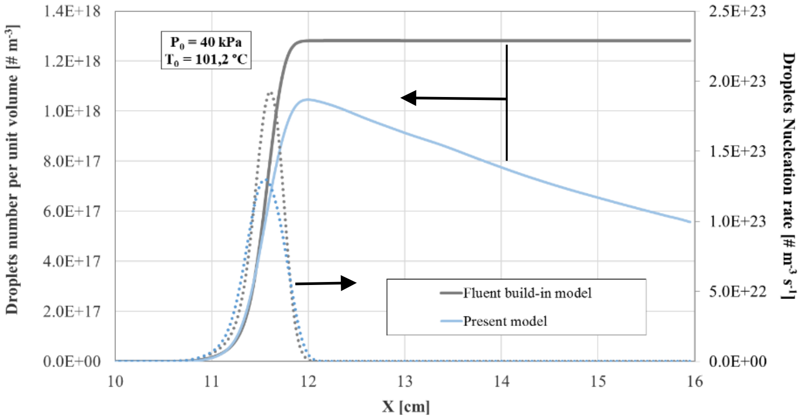

Figure 24 Number of droplets per unit volume of mixture along the nozzle axis (solid lines) and the corresponding droplets nucleation rates (dotted lines)

The reason for this difference is to be found in the formulation for the droplet number conservation, Equation (2.12). In the present model, the equation is written in term of the conservation of the droplets per unit mass of mixture, which, once multiplied by the mixture density, returns the number of droplets per unit volume of mixture (or number density):

$$\eta = \rho_m n \tag{2.24}$$

Writing Equation (2.12) in these terms allows the total number of droplets to be conserved in the computational domain, which is simply shown by performing a volume integration of the LHS of Equation (2.12) (the conservation of the droplet number can equally be obtained by using η as a variable, as long as the proper corrections to the droplet nucleation term, J, are made). Consequently, the present model improves on the Fluent built-in scheme by correctly reproducing a decreasing trend for η. This is caused by the fact that the total number of nuclei n is constant in this region (the nucleation rate is zero) and the flow is expanding in a duct with increasingly larger sections.

2.4 Sensitivity to different model settings

In this section, the sensitivity to some of the most influential parameters of the phase change model is presented, i.e., the surface tension, the nucleation equation and the droplet growth law. Specifically, the impact of suppressing the *Kantrowitz* non-isothermal correction from the nucleation equation was first evaluated. Secondly, the surface tension by using an empirical correlation from IAPWS [52] was described. Lastly, we analyze the use of a well-known droplet growth law that was derived by

Young [51] starting from an equation obtained by Gyarmathy [56]. Its final expression is as follows [33]:

$$\frac{dr_d}{dt} = \frac{\lambda_v}{\rho_l h_{lv} r_d} \frac{\left(1 - \frac{r^*}{r_d}\right)}{\left(\frac{1}{1 + 2C_1 Kn} + 3.78(1 - \upsilon)\frac{Kn}{Pr}\right)} \cdot \left(T_s(p_v) - T_v\right) \tag{2.25}$$

$$\upsilon = \frac{RT_s}{h_{lv}}\left(C_2 - 0.5 - \frac{2 - q_C}{2q_C}\left(\frac{\gamma + 1}{2\gamma}\right)\left(\frac{c_p T_s}{h_{lv}}\right)\right) \tag{2.26}$$

where λ_v is the vapor phase thermal conductivity, $Pr = \mu c_p/\lambda_v$ is the Prandtl number and Kn is the Knudsen number, defined as the ratio between the droplet diameter and the molecular mean free path:

$$Kn = \frac{l}{2r_d} \tag{2.27}$$

The two constants C_1 and C_2 in Equations (2.25) and (2.26) represents two tunable modelling parameters (see [51] for a description of their significance) that are set respectively equal to 0.0 and 9.0, as suggested by Young [51].

Figure 25 shows the comparison of the different model settings for four experimental cases (Exp. 252, 257, 193 and 411; for these last two measurements of the diameters are not available). Clearly, the use of the non-isothermal correction significantly retards the nucleation process with respect to the isothermal case. In turn, this results in a better agreement with experiments in all the simulated cases.

The adoption of the IAPWS correlation for the surface tension does not result in any detectable difference with respect to the formulation proposed by Young [51]. This is because the difference in the surface tension as predicted by the two correlations is always lower than 0.1% (at least for the temperature range of interest). However, it is important to note that both these formulation describes the surface tension as a function of the sole temperature and disregard any potential influence of the curvature radius.

Although it is generally acknowledged that the surface tension depends on the curvature for very small droplet radii (especially below 10 nm [57], which is the range of interest for wet steam flows), experimental evidences are still required to specify how σ depends on r or even identify the sign of this variation (some studies suggest that this may be temperature-dependent, with a transition from positive to negative upon increasing T above ~250 K [57]). Moreover, due to its chief impact on the nucleation process (σ appears within the exponential term of eq. raised to the third power) any change in the expression for the surface tension most likely requires a complete recalibration of the physical model settings and constants. As a result, most of the previous works in the wet steam related literature have been accomplished exploiting the simplified flat-film surface tension assumption, as done in this Chapter.

Finally, the most interesting comparison in Figure 25 relates to influence of the droplet growth law. The analysis of the various results reveals that the Young's droplet growth law can better capture the experimental trends for the average radius. By contrast, the two laws appear to alternatively match the experimental trends for the pressure, with the Young's law that always anticipate the nucleation region with respect to the Hill's expression.

This fact can be explained by considering the specific calibration adopted for the Young's droplet growth law. In particular, it is known that higher values of C_2 (as in this case) serve to boost the growth rate, resulting in larger droplets whilst simultaneously shifting the pressure rise upstream [33]. The analysis of other boundary conditions, not reported here, confirms the alternating performance of the two models. Therefore, it is not possible at present to draw a definite conclusion as to which model performs the best and both these expressions are tested for the analysis of the steam ejector.

Finally, it should be mentioned that the uncertainty connected to the pressure measurements was estimated by Moses and Stein [38] to be about ±40 Pa (the corresponding error bars are approximately of the same size of the experimental symbols in Figure 25). In terms of droplet radius, Starzmann et al. [33] make reference to an estimated uncertainty of perhaps ±20%, although the details of the derivation are not reported.

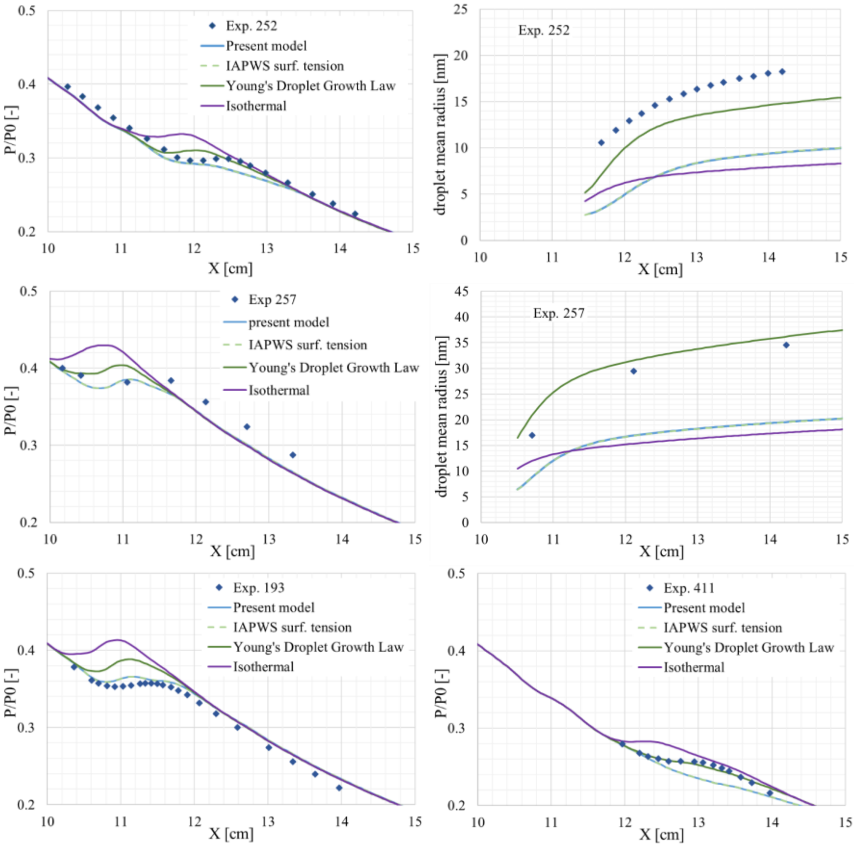

Figure 25 Comparison of model settings for different cases: Exp. 252 (P0=40050 Pa, T0=374.3 K), Exp. 257 (P0=67661 Pa, T0=376.7 K), Exp. 193 (P0=43023 Pa, T0=366 K), Exp. 411 (P0=42276 Pa, T0=385.15 K)

2.5 Steam ejector

In this section, the developed model is validated against data from the supersonic steam ejector studied by Al-Doori [39] and Ariafar *et al* [30]. The main dimensions of the ejector are summarized in Figure 26.

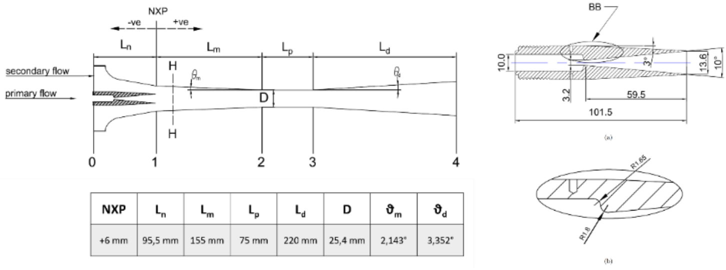

NXP	L_n	L_m	L_p	L_d	D	ϑ_m	ϑ_d
+6 mm	95,5 mm	155 mm	75 mm	220 mm	25,4 mm	2,143°	3,352°

Figure 26 Geometry and dimensions of the steam ejector studied by Al-Doori [39]

The set of boundary conditions analyzed are summarized in Table 2. The solution of the governing equations is achieved exploiting a pressure-based coupled solver. A second order accurate up-wind scheme is selected for the spatial discretization of all transport equations except for the volume fraction and momentum equations. The first of these is discretized through a 3rd order QUICK scheme whereas for the latter a power-law scheme had to be chosen due to numerical instabilities connected with the pressure-velocity coupling.

Table 2 Summary of ejector boundary conditions

Stream	Total Temperature [K]	Total Pressure [kPa]
Motive	403	270
Suction	287	1.6
Discharge		From 4.2 to 7.5 static pressure

A k-ω SST turbulence model is selected for all the simulations because of the specific calibration for transonic applications [58] and based on previous studies on single phase ejector flows [48] [10]. In addition, due to the high Mach reached within the ejector mixing chamber, two additional UDFs are built to endow the turbulence model equations with the correction for compressible mixing layer (in ANSYS Fluent, these are available only for single-phase flows).

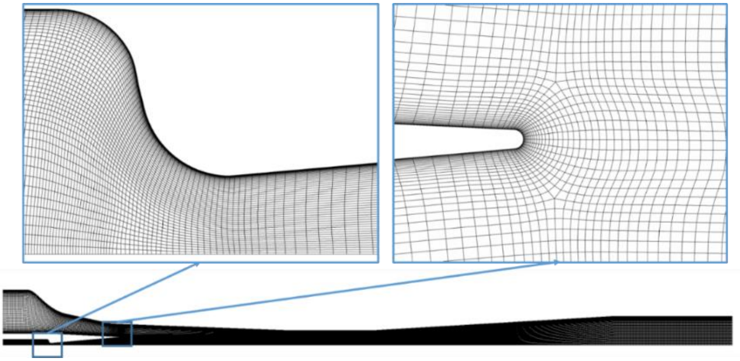

Figure 27 Computational domain and mesh details of the primary nozzle throat and fillet (grid with 70k cells)

Figure 27 shows the computational domain used for all the CFD analyses. Due to the high directionality of the flow (axial velocity component always greater than transversal component), a structured grid is selected to reduce numerical diffusion. Moreover, a straight channel is added at the end of the domain, due to the presence of large recirculation regions at the ejector outlet that prevented reaching stable convergence for some operating conditions. Although this change may induce some approximations, these are most probably limited to a small region near the outlet (the flow upstream of the shock in the diffuser is not influenced due to the hyperbolic nature of the supersonic flow). Moreover, the inclusion of the channel prevents backflow of unknown characteristics from entering into the ejector and allows the recirculation to reattach within the computational domain, thus improving the numerical stability of the simulations.

The adequacy of the mesh refinement was checked by comparing the mass flow rates results for three different grids having all y^+ values less than 1 along the ejector surfaces. Table 3 shows the results of the analysis. In order to reduce the computational time, the grid with 70k quadrilateral cells is selected for all subsequent calculations.

Convergence of the solution is defined by an error in the mass flow imbalance of less than 10^{-5} kg s^{-1} and calculations are stopped when all residuals are stable. Walls are assumed to be adiabatic and smooth.

Table 3 Grid independence results

Grid cells	Mass flow rate [kg/s]			Difference with finer mesh		
	Motive	Suction	ER	Motive	Suction	ER
~35 000	0.00341	0.00111	0.327	0.5%	-13.0%	-13.4%
~70 000	0.00339	0.00128	0.377	0.1%	1.2%	1.1%
~140 000	0.00338	0.00126	0.373	-	-	-

Figure 28 shows the comparison between the experimental and numerical Entrainment Ratio (ER) curves. Both the Young's and Hill's droplet growth law are tested (hereafter referred as Yg82 and Hi66). Details of the experimental apparatus and measurement procedures can be found in [39] (chapter 4 and 5). According to Al-Doori [39], the uncertainty level for the ER is around ±3%. The numerical simulations produce a higher value of ER at on design with a percent difference of about 14%. Moreover, CFD models somewhat anticipate and smoothen the transition toward the off-design regime.

Despite the large discrepancy, Figure 29 illustrates that when results for the motive and suction flows are analyzed separately, differences are smaller than the corresponding value of ER. This is due to a summation of the errors when dividing the two quantities (in other studies, it can be found that the discrepancy was lower for the ER than the mass flow rates, as in [48]). In particular, the greatest discrepancy is achieved for the data of the suction flow rates, with a percent difference of about 7% at on-design, whereas the difference for the motive flow rate is slightly less than 6%. For these two quantities, Al-Doori [39] reports uncertainties of 0.6% and 1-2% for the primary and secondary mass flow rate, respectively.

In terms of models sensitivity, the change of the droplet growth law seems to have a limited influence on the ejector mass flow rates. The only minor change occurs at off design, where the Hill's model performs slightly better than the Young's law. Moreover, a check of many flow variables has revealed only minor differences between the two models, as illustrated in Figure 30 for the volume fraction and Mach profile along the ejector axis. Consequently, all the subsequent analyses in this thesis are carried out by considering only the Hill's droplet growth expression.

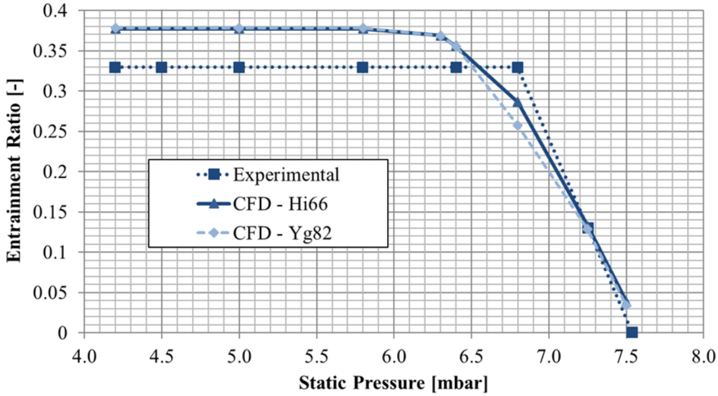

Figure 28 Comparison of experimental and numerical ER (experimental data are taken from [39])

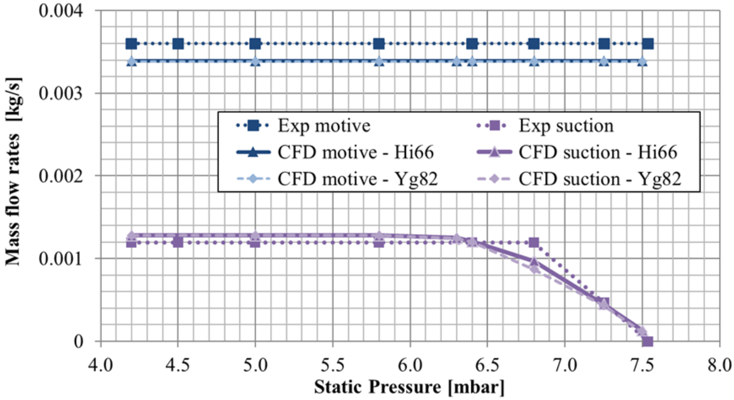

Figure 29 Comparison of experimental and numerical mass-flow rates (experimental data are taken from [39])

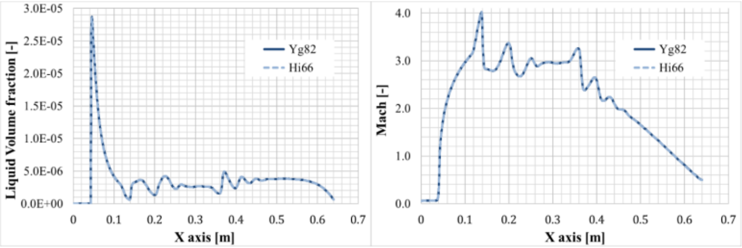

Figure 30 Liquid Volume Fraction (left) and Mach Number (right) profiles along the ejector axis. Comparison of different droplet growth model (P_{out} =4.2 kPa)

Despite the general trend for ER being well reproduced, the discrepancy on the primary flow rate is still large compared with the error that should reasonably arise from the simulation of the 1D flow across a De Laval nozzle. A first possible cause for this discrepancy may come from numerical inaccuracies due to the low grid refinement and low order discretization (especially for the momentum equation). In order to check this hypothesis, a grid/order independence was performed solely on primary nozzle and the results are shown in Table 4. Clearly, despite some differences between the low and high order schemes remaining even for the finest mesh, the scatter is in all cases well below the 1%.

One further reason for the discrepancy of the primary flow rate may be the presence of liquid at motive inlet (it should be noted that no superheating was imposed in the experimental tests). This may increase the average density of the stream passing through the throat, producing a larger value of experimental flow rate. Moreover, the presence of liquid nuclei or steam impurities (such as solid particles) may strongly affect the intensity and type of the condensation process (see for instance [59]). In this respect, a sensitivity analysis was performed by varying the amount of liquid mass fraction at nozzle inlet (the simulations were performed for the 22k nozzle mesh with the 3 order accurate scheme). The results of these trials showed that in order to increase the motive mass flow rate of about 6%, it is necessary to impose nearly 15% of liquid mass fraction at inlet[1], which is a too large amount to explain the discrepancy with experiments. Nevertheless, these trials were performed with the single-fluid approach described previously. This method is generally not suited to investigate problems with secondary or multiple nucleation [60]; hence, the obtained results cannot exclude the presence of liquid nuclei at the motive inlet, which could have an impact on the experimental trends.

Finally, one further cause may be the uncertainty connected with the experimental measurements and with the geometrical dimension of the throat. As for the first, Al-Doori [39] estimates an uncertainty of around 0.6% for the primary mass flow rate, which is almost one order of magnitude lower than the differences with CFD. On the other hand, previous studies performed on a single phase air ejector [48] have shown that even small uncertainties in the throat dimension (connected mostly with the manufacturing process), can lead to discrepancies in the mass flow rate up to many percents. Unfortunately, Al-Doori does not report information on the geometrical uncertainty and manufacturing precision for the investigated profiles. Nevertheless, a first estimation of the sensitivity to the nozzle throat diameter can be achieved by making use of the compressible 1D equations for perfect gases.

---

[1] This indicates that change in flow rate does not linearly depend on density variations, for instance, adding 6% percent of mass fraction at inlet leads to an increase of around 1.5% of the primary flow rate

By considering an average specific heat ratio of 1.3 (as found from inspection of CFD results), this method returns a primary mass flow rate ~ 0.00336 kg/s, which is around 1% lower than CFD results. By making use of this simple approach, it is found that an increase of only 16 µm (i.e., 1% of the nominal diameter) produces a change of the mass flow rate of more than 2%. If we consider this estimated sensitivity to approximately hold for CFD simulations, it follows that a discrepancy of around 50 µm may provide a difference close to the one obtained in the present simulations.

It is concluded that both the presence of liquid at inlet and possible geometrical uncertainties may have played a role in the observed differences with experimental primary flow rate.

Table 4 Motive nozzle mass flow rates for different grid size and discretization schemes

Discr. order / Grid size	1st order	Present setup	Full 2nd order	3rd order
~22 000	3.388 E-03	3.388 E-03	3.369 E-03	3.371 E-03
~44 000	3.376 E-03	3.378 E-03	3.363 E-03	3.365 E-03
~88 000	3.376 E-03	3.376 E-03	3.357 E-03	3.357 E-03

The focus is now moved on the suction flow rate. From a general viewpoint, it is known that accurate predictions of the entrainment process require accounting the influence of compressibility on the mixing layer. In particular, experimental investigations performed in the 70s (e.g., [61], [62]) have shown that compressible mixing layers are affected by a significant reduction of the spreading rate with respect to equivalent low-speed configurations.

Although this effect has been known for a long time, no convincing theoretical explanation has been given yet and turbulence models predict this decrease empirically (see Smits and Dussauge [63] or Gatsky and Bonnet [64] for more details). For ω-based models, Wilcox [65] proposes a correction to the turbulence kinetic energy equation based on the turbulent Mach number:

$$Ma_t = \frac{\sqrt{2k}}{a} \tag{2.28}$$

where k is the turbulent kinetic energy and a is the speed of sound.

The compressibility correction reduces the mixing layer entrainment by increasing the dissipation of turbulence kinetic energy within shear layers. Although its use improves the accuracy for compressible mixing layers, the correction can negatively affect predictions for wall boundary layers at transonic and supersonic speeds [66]. Because of this, the application of the correction was carefully evaluated.

Figure 31 shows a comparison of the turbulent Mach number field between a simulation with the compressibility correction active and one without correction. As can be seen, the turbulent Mach reaches very high levels within the mixing layer and downstream of the shock in the diffuser. In particular, a substantial part of the mixing layer presents values of Ma_t larger than 0.25, which is the threshold for compressibility to have any impact on the mixing layer [66]. The use of the correction limits these peak values and reduces the mixing layer spreading rate. In turn, the suppression of the spreading rate results in a reduction of the suction flow rate of nearly 17% percent. Therefore, the difference with the experimental mass flow rate would be of about 22% without the compressibility correction (as opposed to the 7% obtained with the correction).

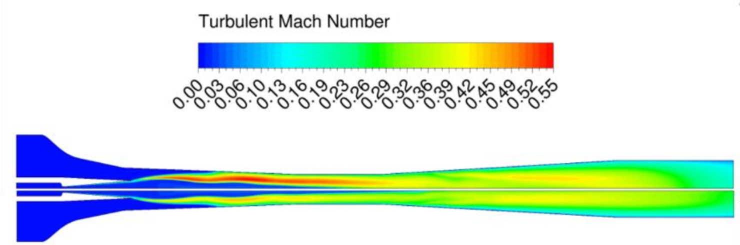

Figure 31 Turbulent Mach number contour for the case with compressibility correction (bottom) and without compressibility correction (top) (P_{out} = 4.2 kPa)

The same compressibility correction model has also been developed for the k-ε turbulence model.

Figure 32 presents the results for the pressure profiles along the ejector wall. In order to perform the comparison, the outlet boundary conditions were imposed so as to match the value of the last pressure probe in the diffuser. This was necessary due to the presence of large recirculations along the diffuser that prevented the pressure recovery from completing at the ejector outlet (it should be noted that the straight channel attached downstream of the diffuser begins at $x= 535.5\ mm$).

Overall, the comparison with experimental data shows a good agreement, especially near the mixing chamber entrance and throat regions. The accord with experiments decreases as flow approaches the diffuser, where the recirculations are found. These are notoriously hard to capture by common two-equation turbulence models and could partly account for the differences with experiments. Furthermore, the discrepancies in the prediction of the mass flow rates may also impact the results for the pressure trends. This is because the energy budget of the total stream is altered due to the different proportions of motive and suction flows, changing the positions of the shock within the diffuser as well as the pressure recovery trends.

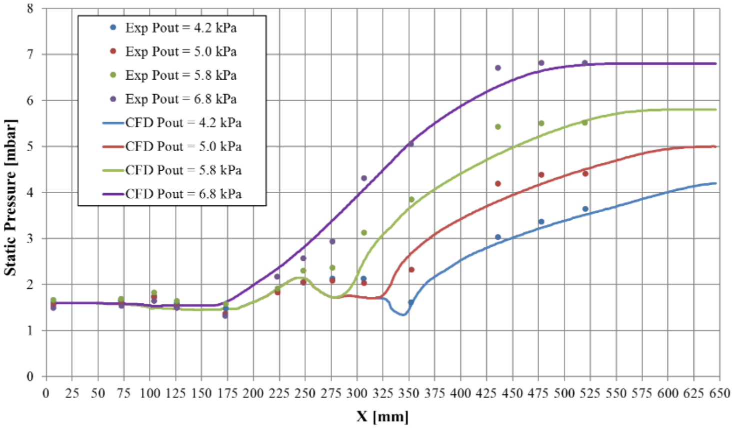

Figure 32 Comparison of experimental and numerical wall pressure profiles (experimental data are taken from [39])

Figure 33 and Figure 34 show the flow recirculation patterns and shock train structures for the different outlet pressures. It is interesting to note that the case with the lowest outlet pressure present a flow pattern that consists of two different vortex structures. A first one, smaller, occurs right after the shock train in the diffuser, and a second, larger, farther downstream. This case also presents the best agreement with the experimental pressure trend. According to CFD, the patterns adjust to a single vortex structure when the outlet pressure is increased. However, the agreement with experiments is reduced, therefore, these numerical patterns should be considered with some caution. Finally, the numerical Schlieren contours in Figure 34 show that the pressure-based scheme adopted in this work can qualitatively reproduce the shock train structures within the ejector. However, the thickness of each shock may be overestimated due to the higher numerical diffusion of these schemes.

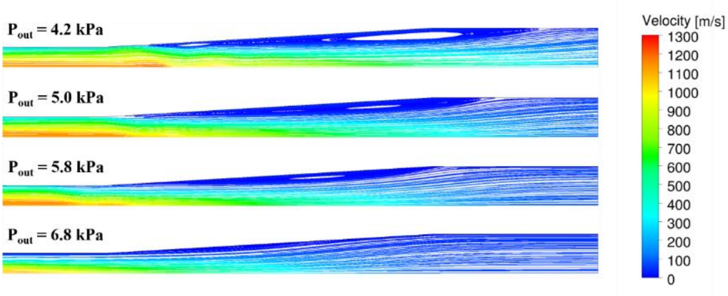

Figure 33 Streamline pattern at the ejector outlet showing the recirculation regions

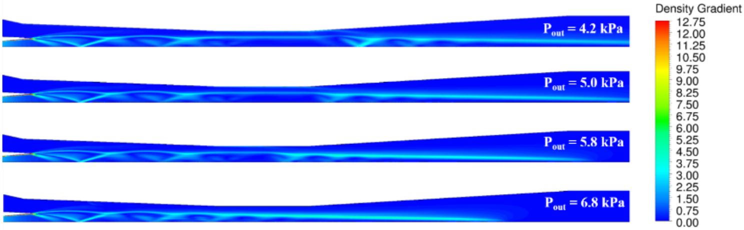

Figure 34 Numerical Schlieren images (density gradient contour) showing the shock train structures

Figure 35 shows the contour of the liquid mass fraction for the case with the lowest outlet pressure (P_{out} = 4.2 kPa). As can be seen, the condensed phase reaches value up to 20% of the total mass, with peak levels in the region downstream of the nozzle exit plane. This is due to the further acceleration caused by the primary jet under-expansion. The absence of any superheating of the motive stream exacerbate this problem that can lead, in some extreme cases, to the formation of ice inside the ejector (as discussed in the next section).

Figure 35 further illustrates that the liquid mass fraction evaporates almost completely toward the ejector outlet, where the mixed stream undergoes the shock trains and decelerate to reach the outlet pressure. In addition, the liquid mass fraction goes to zero at the nozzle wall, due to the heat recovery caused by the fluid deceleration and viscous dissipation within the boundary layer [28].

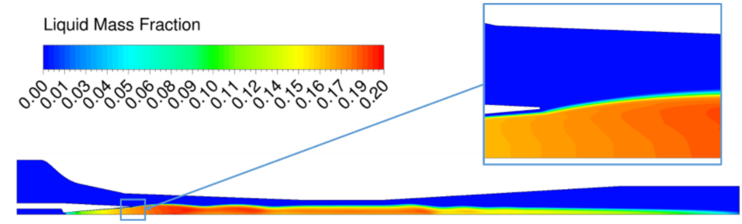

Figure 35 Liquid mass fraction contour (case with P_{out} = 4.2 kPa)

Figure 36 shows the contour of the droplet number per unit mass of mixture, n. The figure displays also the line representing the boundary where the liquid mass fraction is zero.

The contour clearly reveals the presence of a radial distribution of the droplet number. This stems from the significant curvature of the nozzle profile at the throat, which induces a region of low pressure near the wall and causes a stronger nucleation. The nucleated droplets are then convected down the ejector along streamlines and the radial distribution persist almost unaltered till the outlet.

The analysis of Figure 36 further shows that the droplets number contour follows closely that of the liquid mass fraction depicted in Figure 35. This is a direct consequence of the assumption of equal velocity between the phases. Yet, the comparison reveals also that toward the ejector outlet, where the condensed mass evaporates completely, the liquid droplets do not disappear but survive in the form of nuclei with zero mass and volume. The reason for this numerical error is to be found in the absence of a “droplets sink” term within the droplet transport equation, Equation (2.12).

This is a common feature of the single-fluid approaches which partly prevent their use in applications where secondary nucleation occurs (e.g., multi-stage steam turbine cascades). Although in principle it could be possible to add a sink term to the droplet number equation, in practice, the differential nature of the droplet transport equation complicates this task. For instance, the inclusion of a negative sink term in Equation (2.12) leads to regions with negative numbers of droplets. This problem may be worked around by positively limiting the value of the droplet number. Unfortunately, this is not possible in ANSYS Fluent.

Other options may exist in which, for instance, the value of the sink term is related to the number of droplets existing in the cell or it is described on a logarithmic basis. To the author's knowledge, these approaches have never been attempted before and may require an extensive development work. However, this effort may not be completely justified in view of the fact that the assumptions implicit in the single-fluid approach would anyhow lead to significant approximations (e.g., the droplet sizes originating from different nucleation sites are averaged out). In this respect, the adoption of more advanced schemes, such as the multi-fluid approach mentioned in the introduction or a Lagrangian approach (e.g., [60]), naturally account for the removal of droplets from the computational domain and can provide more accurate results than the method used in this work.

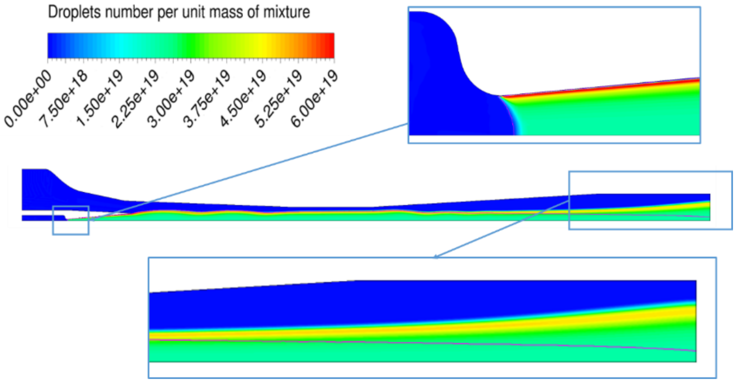

Figure 36 Contour of droplet number per unit mass of mixture (in purple is the line where the liquid mass fraction is zero; case with P_{out} = 4.2 kPa)

2.6 Model limitations

In this section, a review of certain specific limits connected with the developed model and a discussion on some possible implications deriving from them is presented. In doing so, the focus will be on those assumptions that seem particularly restrictive with respect to steam ejector applications.

A first limit connected with the developed model relates with the droplet growth regime. Generally speaking, the growth rate formulation for a liquid droplet is calculated differently depending on value of the Knudsen number. During the initial phase of the droplet growth, the liquid nucleus is generally much smaller than the mean free path, i.e., *Kn>>1*. Under these conditions, named as *free molecular regime*, the continuum hypothesis does not hold and the calculation of the droplet growth must be accomplished by means of kinetic theory or statistical mechanics concepts. At the other extreme is the situation where *Kn<<1.* In this case the droplet is large enough to apply the macroscopic balances for heat, mass and momentum. In between these two conditions is what is called the transition regime (*Kn~1*). This is the most difficult to analyze and is usually handled by means of interpolations formulae that connect the continuum and free molecular regimes (see for example [51]).

Specifically, the Hill's droplet growth law adopted in this work is valid only for the free molecular regime, so that some questions may arise about its applicability to ejector flows (especially in the case of under-expanded nozzles with a delayed appearance of shocks that can vaporize or reduce the droplet dimensions [28]).

Figure 37 shows the trend of the Knudsen number along the ejector axis, for one of the simulated cases (but all cases present similar trends). Clearly, the value of Kn is always well above unity except for a very small region near the primary nozzle throat. In this zone, the vapor temperature is still high and the mean free path is of the same order of magnitude of the droplet diameters (around 10^{-9} m).

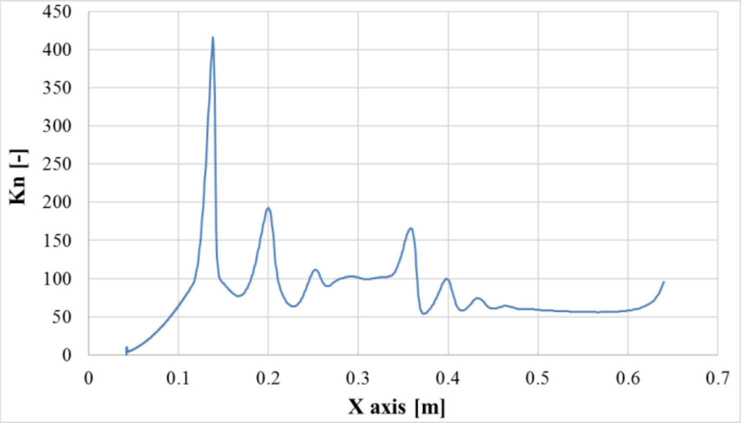

Figure 37 Knudsen number trend along the ejector axis (case with $P_{out} = 4.2\ kPa$)

Somewhat connected with the issue of the droplet growth regime is the assumption of velocity equilibrium between the phases. In order to understand whether a particle will follow the gaseous stream trajectory or depart from it, it is possible to estimate the Stokes number related with the particle velocity [67].

The Stokes number is defined as the ratio between the droplet response time to a variation in the velocity field and a flow characteristic time of the continuous phase:

$$St = \frac{t_d}{t_v} \qquad (2.29)$$

When the Stokes number is much lower than unity, the condensed phase will closely follow the gaseous stream and the assumption of a common velocity between the phases, as in the present work is allowed.

The droplet response time depends on the condensed phase inertia and on the carrier phase viscosity [67]:

$$t_d = \frac{\rho_d D_d^2}{18\mu_v} \tag{2.30}$$

The carrier phase time can be calculated as the ratio between a characteristic velocity and length scale:

$$t_v = \frac{u_v}{L} \tag{2.31}$$

Clearly, the definition of this last quantity is somewhat arbitrary because no specific definition of the characteristic length is provided. For nozzle flow, this is often the throat diameter, the use of which would give an estimate of St ~10^{-3}. However, this result refers to a characteristic time representative of the mean flow and does not consider any possible velocity mismatch arising from the interaction between turbulence and the dispersed phase. To this aim, t_v can be chosen so as to represent a turbulent characteristic time. Specifically, it is possible to calculate the Stokes number by using the inverse of the specific dissipation rate, which represents the frequency of the smallest turbulent eddies (those occurring at the Kolmogorov scale), i.e.:

$$t_v = t_{turb\_min} = \frac{1}{\omega} \tag{2.32}$$

where ω is the specific dissipation rate.

Figure 38 shows a map of this "turbulent" Stokes number within the ejector. Clearly, the assumption of equilibrium velocity appears to be satisfied in the whole two-phase flow domain, meaning that the fluid particle velocity should follow not only the average flow trajectories, but also the path of the smallest turbulent eddies (those with the highest frequency).

However, it should be noted that the above Stokes number was calculated under the assumption of "smooth" flow conditions. The presence of any local perturbation may notably reduce the characteristic length, which, in the specific case of a dynamic shock, is generally of the same order of magnitude of the molecular mean free path. In this case, the different inertia between vapor and liquid droplets may produce a local velocity mismatch and lead to the departure of the phase trajectories. Moreover, the effects of drag and interphase momentum exchange has been neglected in this work although it could represent a non-negligible source of kinetic energy losses. Detailed analyses of these type of processes is a complex task and may require the use of more advanced models than the single-fluid approach.

Finally, a last, key aspect that is of particular concern for steam ejector studies is related to the very low temperature levels attained by the expanding stream. This problem is particularly critical for ejector refrigeration applications, where efficiency considerations impose the use of low or no level of superheating at the inlet of the motive stream (this is also the case for the experimental results used in this work). Consequently, the motive jet can reach temperature levels that go well below the triple point, causing the possible appearance of ice.

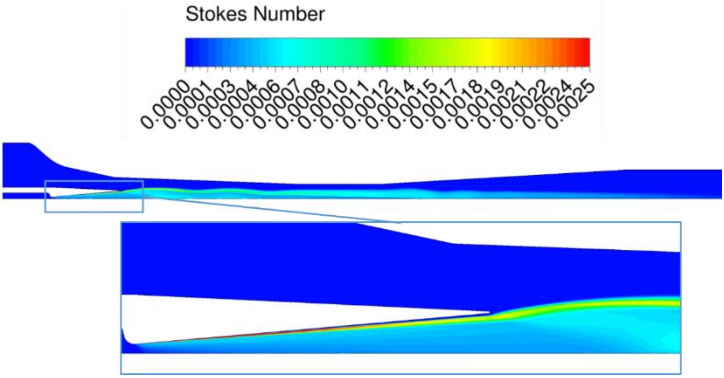

Figure 38 "Turbulent" Stokes number within the ejector (case with P_{out} = 4.2 kPa)

Figure 39 shows the mixture temperature contour within the ejector. Clearly, the temperature goes well below the limit of the triple point and the presence of ice cannot be excluded (especially downstream of the nozzle exit plane where the mixture temperature reaches values close to 210 K). Nevertheless, ice crystal formation, in much the same way as for droplet nucleation, is fundamentally a time dependent phenomenon and some degrees of supercooling usually exists before the water vapor or liquid starts to solidify.

In particular, experiments in cloud chambers with pure water vapor indicates that the homogeneous nucleation of ice usually occurs with around 30-40 K of supercooling [68]. By contrast, recent investigations in supersonic nozzles have shown that for the high cooling rates and small cluster sizes that are achieved in these devices, the supercooling can be as high as 90 K (i.e., supercooled water temperatures of nearly 190 K) [69]. However, these tests were conducted with ultrapure water and may not be directly applicable to the present case (this is because impurities in the water droplets or vapor stream can greatly anticipate crystal formation). As a result, the presence of ice cannot be excluded in the steam ejector under investigation.

The appearance of water ice crystal may induce substantial modifications to the mixture flow behavior. For instance, the change in the latent heat release (from the value of condensation to that of solidification) may modify the nozzle Mach and pressure profiles. Moreover, phenomena such as crystals agglomeration and deposition may be important and could lead to modifications in the ejector geometrical profiles. On the other hand, the presence of shocks immediately after every steam expansion may lead to the sudden melting of the ice, limiting its impact on the global flow dynamics. In this case, numerical simulations may still incur in significant discrepancies due to the uncertain extrapolation of the supercooled water properties below the triple point temperature (most of these, including viscosity, specific heat, surface tension and others, present exponential variations with decreasing temperatures [68]). In view of these many aspects, it is important that future experimental investigations properly address the analysis of ice formation inside steam ejectors.

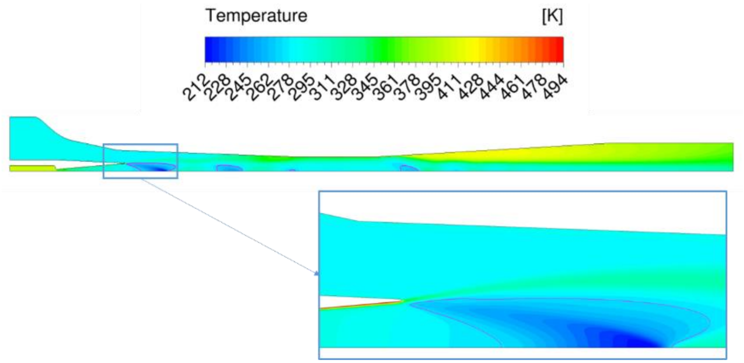

Figure 39 Temperature trend along the ejector; in purple is the line corresponding to the triple point temperature (case with P_{out} = 4.2 kPa)

In order to conclude this part of the work some comments and remarks will follow.

A numerical model for the simulation of wet-steam flow has been developed and implemented within the CFD software ANSYS Fluent via User Defined Functions. This approach allows great flexibility in the choice of the physical model settings and calibration parameters.

The model has been tested against experimental data from a De-Laval nozzle and a steam ejector test-case. The nozzle simulations have shown that the developed model can produce results that substantially agree with experiments and that are in line with those provided by the ANSYS Fluent wet steam model. However, the model improves on the Fluent built-in scheme by providing a proper conservation of the number of droplets within the computational domain. The analysis of the sensitivity to changes in model settings has shown the importance of both the nucleation rate non-isothermal correction and droplet growth law in predicting the condensation starting position. By contrast, the adoption of the IAPWS correlation for the surface tension did not result in any detectable difference with respect to the formulation used in the present model.

Simulations for the steam ejector test case have demonstrated a substantial agreement with experiments, both in terms of mass flow rates and wall pressure profiles. Some discrepancies are found for the primary mass flow rate that probably stems from the presence of liquid at the nozzle inlet or from uncertainties in the nozzle throat dimensions. The entrainment of the secondary flow can also be reproduced with accuracy, as long as the effects of compressibility on mixing layer development are accounted for in the turbulence model.

The analysis of the internal flow features has shown that, due to high level of expansion of the primary jet, the liquid mass fraction reaches values up to 20% within the mixing chamber. In this region, the mixture temperature goes well below the water triple point, indicating the possible presence of ice. However, the limited residence time and the presence of shocks may limit the impact of ice formation on the flow dynamics.

The assessment of the Knudsen and Stokes numbers within the ejector suggests that the approximations of free molecular droplet growth regime and velocity equilibrium between the phases should be valid, at least in the flow regions away from dynamic shocks.

In conclusion, it is important to note that some of the most important limitations of the model are related to the assumption of the flat-film surface tension as well as to the absence of a sink term in the droplets number equation. Improvements in both these two aspects may greatly increase the prediction capability of the wet-steam model but require an extensive development and tuning process that will be the subject of future studies.

The accuracy of the developed model has been also tested in comparison with a 2D steam turbine stationary cascade in [70] with experimental data form literature [71]. This part is not presented in detail in the doctoral thesis since it is off-topic. The finding that the author would like to mention is the general accuracy of the present model with steam turbines applications as well.

2.7 Metastability effects

The developed Wet-Steam model has also been tested in comparison with the Homogeneous Equilibrium Model described in Section 2.2. The reference test case is the ejector of Al-Doori [39]. The boundary condition are the same of the previous section and are summarized in Table 2.

Figure 40 shows the comparison between the experimental and numerical Entrainment Ratio (ER) curves (the entrainment ratio is the ratio of the motive to suction mass flow rate). The results illustrate that none of the numerical model clearly outperform the others in predicting the experimental trends. For instance, although the mixture model with the k-ε turbulence model seems to reproduce well the ER at on-design conditions (around 5.4% difference with experiment), the transition to off-design is clearly anticipated with respect to the experiments. Conversely, the mixture model with the k-ω SST turbulence model is less accurate at on-design but it better captures the global trend at off-design. The HEM model is the least accurate among the models both in terms of mass flow rate and critical pressure predictions.

Figure 41 shows the same trends by isolating the contribution of the motive and suction mass flow rates. As can be seen, there is a non-negligible discrepancy in the results for the primary flow rates, which is of the order of 6% and 11% for the mixture and HEM models, respectively. The curves for the motive flow practically coincide for mixture models. This is because the motive mass flow rate is not influenced by a change in the turbulence model. By contrast the motive mass flow rate of the HEM is the lowest. This is due to the fact that this model predicts the start of the condensation before the nozzle throat. The main effect of this condensation is the release of latent heat to the vapor, which increases the fluid temperature and reduces the overall density as well as mass the flow rate of the motive stream.

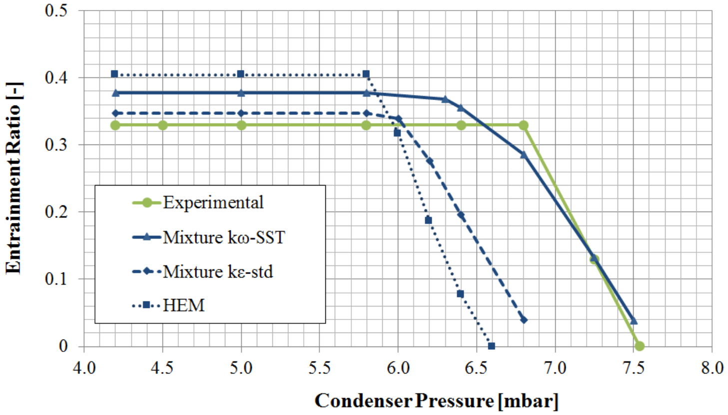

Figure 40 Comparison of experimental and numerical ER (experimental data from [39])

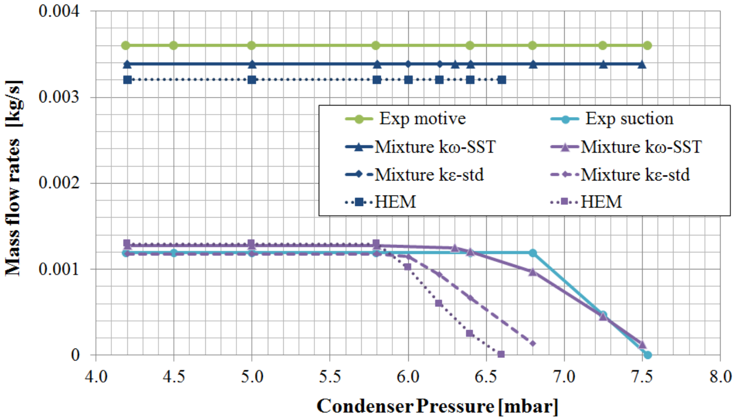

Figure 41 Comparison of mass flow rates (experimental data from [39])

The effect of the anticipated heat release is demonstrated by plotting the temperature trend along the ejector axis, as in Figure 42. The plot shows that the temperature rise of the HEM begins earlier than that of the mixture models. For these last, the condensation occurs abruptly after the throat as a consequence of the condensation shock (see the zoomed box in Figure 42). The figure also shows that the temperature falls down the triple point. This is especially true in the case of the mixture models, where it reaches a minimum value lower than -50°C, thus indicating the possibility of ice formation.

Figure 43 shows the trend of the liquid mass fraction along the ejector axis. Clearly, the HEM model reaches higher values of condensed mass. Moreover, the fluctuations are more severe than for the mixture schemes. This may be explained by the presence of a relaxation time in the case of the Non-Equilibrium models that acts as a damper of the phase-change related oscillations (the same effect is seen on the pressure trend, but it seems inverted in the temperature variations in Figure 42).

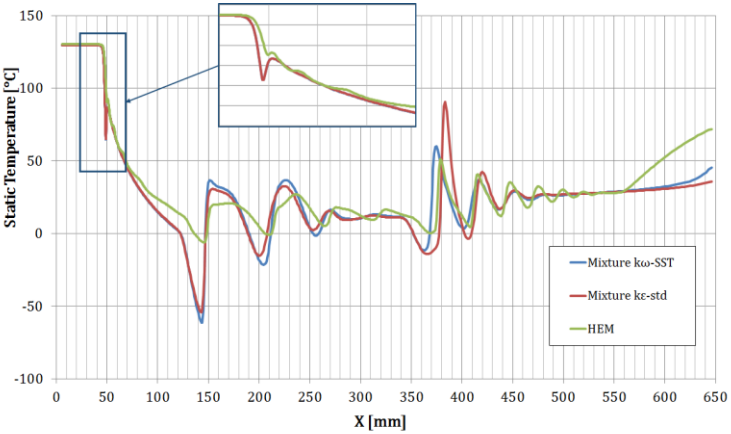

Figure 42 Static temperature trends along the ejector axis

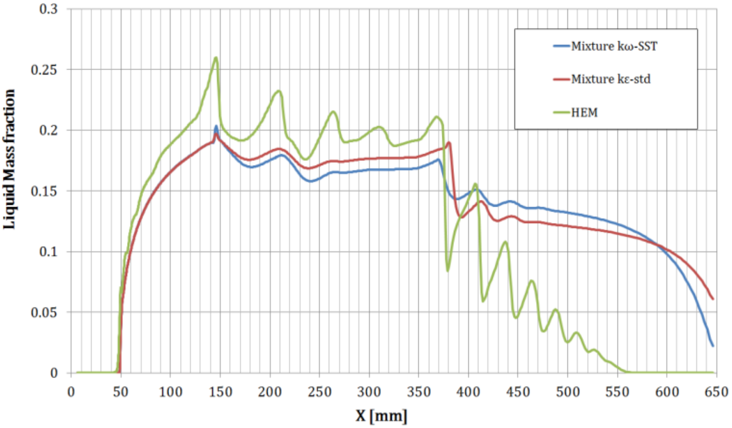

Figure 43 Liquid mass fraction along the ejector axis

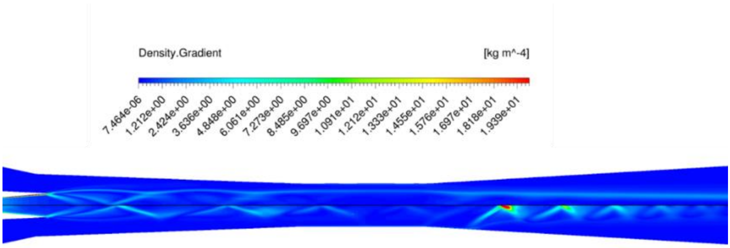

Figure 44 Density Gradient Contour (Numerical Schlieren). Mixture-Model (TOP) vs. HEM (BOTTOM)

This is also visible in Figure 44, where the comparison of the two density-gradient contours is shown. The strength of shock and expansion waves is clearly reduced in the mixture model where the effects of metastability play an important role.

Finally, Figure 45 shows the comparison between the experimental and numerical wall pressure profiles. As can be seen, the agreement is quite satisfactory for all the evaluated models. Some discrepancy appears in the mixing chamber and at the ejector diffuser, where the numerical simulations predict a lower pressure than experiments. Nevertheless, all models seem to qualitatively reproduce the experimental trends. Surprisingly, this holds true even for the case with the highest outlet pressure (P_{out}= 6.8 kPa), for which the analysis of the mass flow rates (Figure 40 and Figure 41) showed that CFD predicts off-design conditions, whereas the experimental curve appear to be still in on-design mode.

This fact suggests that more and different experiments should integrate mass flow rates and pressure profiles in order to precisely assess the accuracy of different CFD models. For instance, trends of wall temperatures may be extremely useful to cross check the accuracy of turbulence and multiphase models in general.

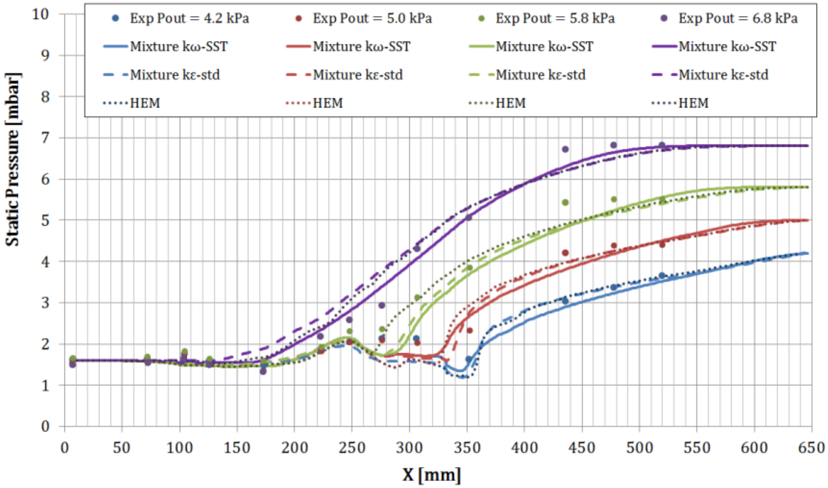

Figure 45 Comparison of wall pressure profiles (experimental data form [39])

2.8 Eulerian-Eulerian model

In the full Eulerian-Eulerian implementation of the WS model a full set of governing equations is solved for each phase. The set-up and of the model is similar to the one described in Section 2.3 for the Mixture model. The adopted discretization methods are Least Squares Cell Based for the Gradients and 3rd order QUICK for all the other quantities. The geometry and computational mesh are the same as shown in Figure 22.

The additional closure equations needed to model the phases interactions are described in [32] and can be summarized as follows:

- *Schiller-Naumann* correlation for Drag law;
- Symmetric interfacial area concentration for the liquid phase;
- *Hughmark* correlation for heat transfer between the phases.

The resulting normalized pressure profile is plotted in Figure 46 in comparison with Mixture-Model and standard Fluent model.

The three pressure profiles are basically coincident and there is no appreciable difference between them. However, the Eulerian-Eulerian model could allow improvements against the mixture model for several applications.

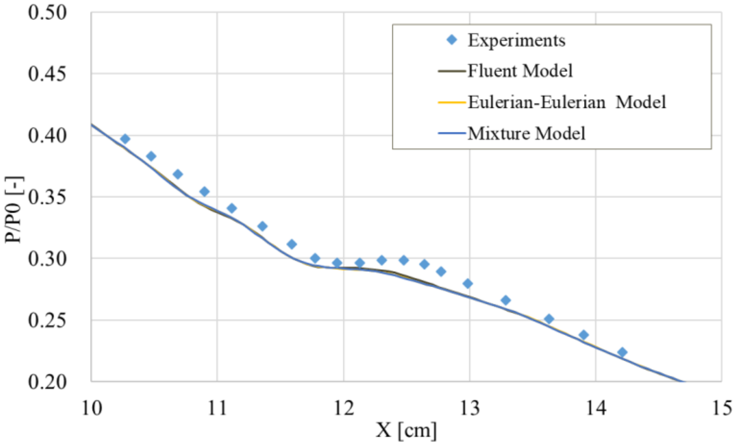

Figure 46 Normalized pressure trends along the nozzle axis

2.9 Concluding Remarks

Two numerical model for the simulation of wet-steam flows have been validated and tested against a steam ejector test-case. The first one is a Non-Equilibrium Mixture Model that accounts for metastability effects during steam condensation. The second one is a Homogeneous Equilibrium Model that assumes velocity and thermal equilibrium between the phases. Both models have been implemented within the commercial CFD software ANSYS Fluent by means of several User-Defined Functions. This approach allows great flexibility in the choice of the physical model settings, calibration parameters and fluid properties.

Simulations for the steam ejector test case have demonstrated that the mixture model can better reproduce the experiments in terms of mass flow rates. The analysis of the internal flow features has shown that the liquid mass fraction reaches values up to 20% and 25% for the mixture and HEM models, respectively.

The HEM was found to be less accurate with respect to the WS model and less costly from a computational point of view. Even with its simplified approach, it can still reproduce the main flow features of the ejector. Hence, it has to be intended as a versatile preliminary analysis tool. Such a model will be also used for flashing CO_2 calculations in the next chapter.

Finally, the development of a full Eulerian-Eulerian model has been presented and validated for the condensing steam nozzle only. This latter model is less interesting for ejectors application because of stability issues but it could give the possibility to accurately model the phases interactions for several applications, such as steam turbines.

3 Chapter 3

The part of the thesis about experimental and numerical activity on flashing CO_2 will be described in this Chapter. The results shown in this chapter have been published in [72], [73] and [74].

3.1 CO_2 Flashing Flow

The use of ejectors to improve the efficiency and capacity of vapor compression chillers has seen a renewed interest from both industry and academy in recent years. One of the fluids that benefits the most from the modification of the conventional cycle (e.g., by the inclusion of a two-phase flashing ejector) is carbon dioxide.

The use of ejectors in R744 vapor compression cycles was first proposed by Lorentzen [75] and widely tested both numerically and experimentally (e.g. [14] and [2] to cite some). These early studies demonstrated significant efficiency and capacity improvements despite the low additional investment cost.

A novel CFD approach for the flashing of CO_2 through nozzles and ejectors will be presented in this Chapter. The novelty of the method is represented by the possibility of defining both the liquid and vapor phases as compressible materials with the properties of each phase obtained via lookup-tables calibrated against standard fluid libraries and are valid in the whole domain of interest, including the supercritical, subcritical and metastable regions.

The model has been implemented within a commercial CFD solver and is completely general, i.e., it can be applied to any type of compressible single and multiphase flow. In what follows, the proposed approach is validated against an experimental test-case available in literature.

One of the most common cycle improvement was shown in Figure 1 (see Introduction), where the ejector is used to compress the low-pressure vapor from the evaporator to the receiver, thus reducing the pressure ratio of the compressor. A further benefit of the ejector is the increase in system capacity thanks to the reduction of the throttling losses faced by the flow coming from the gas cooler (or condenser).

The main challenge in the research and development of the ejector is the understanding and modeling of the complex flow occurring in such a device. Some of the typical features are, for instance, two-phase non-equilibrium flow with phase change, presence of shocks and expansion-waves, recirculation, supersonic mixing layer between motive and suction flows. Consequently, the development and validation of predictive CFD models is necessary in order to enhance the performance of these devices.

To date, several CFD studies on two-phase flashing ejector have already been conducted, but more work has still to be done in order to improve the currently available models. In the work of Yazdani et al. [76] the authors used a “Mixture-Model” approach to simulate the flow of CO_2 within flashing ejectors. Basically, this is a single phase model with the solution of the volume fraction transport equation of the vapor phase. The model is capable to account for the non-equilibrium phase change in the ejector and the authors implemented it in the commercial code ANSYS Fluent. Lucas et al. [43] used a homogeneous equilibrium model (HEM) with the phase change occurring in equilibrium and the two phases sharing same pressure and temperature; in this case, the model was implemented within the open source CFD code Open-FOAM. In Smolka et al. [42] the authors employed a HEM based on a modified enthalpy transport equation implemented in the commercial code ANSYS Fluent. A similar approach was used by Giacomelli et al. in [72] and [73] who evaluated the fluid properties through a bi-linear interpolation of lookup-tables. The tables were automatically generated by means of a Matlab [41] script linked with the NIST Refprop v.9.0 libraries.

In 2011, Colarossi [77] developed a Homogeneous Relaxation Model (HRM) and implemented it within the CFD code Open-FOAM. A similar model was also developed in ANSYS Fluent by Haida et al. [45], by modifying the previously validated HEM.

3.2 Flashing Model Validation

The present Section presents a novel approach that treats both the liquid and vapor phases as compressible materials. The method was developed within the CFD package ANSYS Fluent v19.0 [78] and is based on the construction of dedicated R744 look-up tables and their extension in the metastable region. The computational results are compared against the experimental data obtained by Nakagawa et al. [79] for a R744 flashing nozzle.

The numerical model is again based on a single fluid approach, also known as Mixture-Model. The set of averaged conservation equations for mass, momentum and energy has the following form:

$$\frac{\partial \rho_m}{\partial t} + \frac{\partial \rho_m u_{mj}}{\partial x_j} = 0 \tag{3.1}$$

$$\frac{\partial \rho_m u_{mi}}{\partial t} + \frac{\partial \rho_m u_{mi} u_{mj}}{\partial x_j} = -\frac{\partial p}{\partial x_j} + \frac{\partial \tau_{ij\_eff}}{\partial x_j} \tag{3.2}$$

$$\frac{\partial \rho_m E_m}{\partial t} + \frac{\partial \rho_m u_{mj} h_m}{\partial x_j} = \frac{\partial q_{j\_eff}}{\partial x_j} + \frac{\partial u_{mi} \tau_{ij\_eff}}{\partial x_j} \tag{3.3}$$

$$\frac{\partial \rho_v \alpha_v}{\partial t} + \frac{\partial \rho_v u_{mj} \alpha_v}{\partial x_j} = \Gamma_e - \Gamma_c \tag{3.4}$$

The subscript *m* refers to mixture properties that are calculated by means of mass or volume weighted averages (see Chapter 2).

Since the flow is expected to be supersonic or near the sonic conditions, the definition of the two-phase sound speed requires special consideration. The definition of this property of the flow is not accessible and modifiable by the user of ANSYS Fluent but, as already reported in [26], the following equation, already presented in Chapter 1, was found to be used by the solver:

$$a = \sqrt{\frac{1}{(\alpha_l \rho_l + \alpha_v \rho_v)\left(\frac{\alpha_l}{\rho_l a_l^2} + \frac{\alpha_v}{\rho_v a_v^2}\right)}} \tag{3.5}$$

It is worth to remember that this equation represents the harmonic-average of the sound speeds of saturated phases [19] and is commonly used in many CFD applications, especially for water and steam mixtures ([26], [20] and [8]). Finally, the effect of slip velocity between the phases is neglected, and the phases are assumed to share the same pressure and temperature (mechanical and thermal equilibrium conditions). Hence, the following identities are valid in the whole domain:

$$u_v = u_l = u_m \qquad (\ 3.6\ )$$

$$p_v = p_l = p \qquad (\ 3.7\ )$$

$$T_v = T_l = T \qquad (\ 3.8\ )$$

Γ_e and Γ_c in Equation (3.4) are the mass-transfer source terms related to the evaporation and condensation process, respectively. The two terms can be written in the following form:

$$\Gamma_e = \sigma_e \alpha_l \rho_l \frac{T \quad - T_{sat}}{T_{sat}} \qquad (\ 3.9\ )$$

Which is valid if T > T_{sat}; else if T < T_{sat} one has:

$$\Gamma_c = \sigma_c \alpha_v \rho_v \frac{T \quad - T_{sat}}{T_{sat}} \qquad (\ 3.10\ )$$

σ_e and σ_c are two accommodation coefficients that can be interpreted as relaxation times [78] and can have different values for condensation and evaporation. From now on these coefficients will be referred to as evaporation and condensation factor, respectively. The saturation temperature in Equations (3.9) and (3.10) is calculated as a polynomial function of the static pressure natural logarithm and implemented into Fluent by means of a UDF.

The phase change model is obtained by substituting the Clausius-Clayperon equation into the Hertz-Knudsen equation. For more details on the derivation and the physical basis of the model the reader is referred to [78] and [17]. The described model is available in ANSYS Fluent as a standard mass-transfer model.

To date, more accurate methods exist that employ either Mixture or full Eulerian-Eulerian multiphase approaches. These methods have been extensively used to simulate the flashing of water, e.g. in [80], [81] and [82]. In this case, detailed experimental data are abundant in the literature, which allows a proper calibration of the several unknown parameters that characterize the mass, momentum and heat transfer between the liquid and vapor phases. More details on recent advancements in the numerical modeling of flashing water flow can be found in the review of Liao and Lucas [82] and in the work of Karathanassis et al. [83].

Unfortunately, experimental test cases for CO_2 flow are still lacking. In particular, new experiments are needed that can provide simultaneous evidence of wall temperature and pressure profiles, mass flow rates measurements, local bubble density and diameters, as well as insights on the wall conditions. Therefore, the model adopted in the present work is a standard Mixture Model that allows avoiding the calibration of a great number of unknown parameters. This new procedure is completely general and it can easily be adapted to any fluid in both single and two-phase flows.

The evaluation of the fluid thermodynamic properties in compressible multiphase flow is a topic of primary importance. The inaccurate evaluation of these properties can lead to significant deviation with respect to actual mass flow rate and local pressure or temperature trends. This issue is even more critical for CO_2 due to the extremely high pressure variations typical of nozzle and ejector flows. The solution to this problem generally requires the definition of two compressible materials, one for each phase.

The best way to define the properties for a compressible phase in ANSYS Fluent is to adopt a *User-Defined Real Gas Model* (UDRGM), which is a set of C programming language function that can be edited by the user. However, in multiphase flows only one UDRGM can be adopted, e.g., the liquid phase. The definition of the vapor properties is thus subjected to some limitations; most notably, the isobaric specific heat capacity and specific enthalpy must be function of temperature only. In principle, this is not a very stringent restriction when the liquid or vapor phase are far from the critical state. However, in HVAC applications the flow of CO_2 is often transcritical and the fluid properties undergo large variations with respect to both temperature and pressure. A workaround to this problem consists in the use of a Multispecies-UDRGM.

The adoption of this scheme within the Fluent multiphase solver allows defining a UDRGM for both the liquid and vapor phases.

In order to accomplish this, two different *species* and two different *phases* must be defined, as described in Figure 47. The first of the two *species* has the properties of the liquid CO_2 and it is named the “liquid species”. The second *species* has the properties of vapor and it is called the “vapor species”. The properties of two species are coded inside a unique *Multispecies-UDRGM* file. This file is then duplicated to express the properties of both the liquid and vapor.

This procedure activates four species, two of which must be considered as “dummy”. In order to do this, the *mass* fraction Y of each species (in the domain of the corresponding phase) at the nozzle boundaries is set to a constant value that is either 1 or 0. Moreover, the mass transfer mechanisms due to evaporation or condensation is activated only for the two species of interest. Finally, unphysical diffusion between the species is suppressed by setting the molecular diffusivity of each material to a nearly-zero value and by imposing a very large turbulent Schmidt number (this is needed for the turbulent model). As a result, the final set of equations correspond to the Mixture-Model equations described in the previous section.

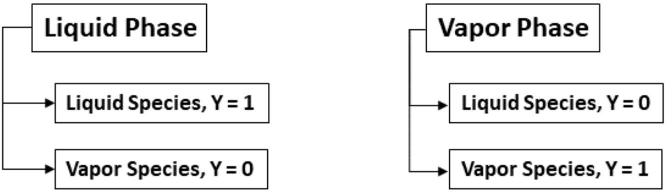

Figure 47 Multispecies multiphase model layout

In order to obtain an accurate and computationally efficient approach the properties of both phases are inserted in the multi-species-UDRGM by means of 22 lookup-tables. As reported in [22] [24] [72] [84], this method is a practical and common solution for CFD simulations.

In the present model, all the lookup-tables have been automatically generated through a VBA Excel code and printed in ASCII text files. The code is directly linked with the NIST Refprop libraries [40], which use the Span and Wagner equation of state (EOS) for the properties of R744 [85]. This EOS makes use of the Helmholtz-free-energy potential and represents the current state of the art for the description of CO_2 properties. It is worth to mention that the properties calculated with this method can be extended in both the liquid and vapor metastable regions, up to the respective spinodal lines (for further details on how to calculate metastable properties with Nist Refprop, the reader is referred to [40]).

As an example, Figure 48 shows the density map for the liquid phase, as obtained from the corresponding lookup-table. The metastable states are included in the region that lies between the saturation line (in red) and the spinodal limit. Beyond this limit, the NIST database would return a non-value, which can produce abrupt interruption of the fluid properties definition. Therefore, an extrapolation of the properties beyond the spinodal line (not shown in Figure 48) was necessary in order to avoid numerical errors during the first iterations. The steps sizes in terms of Temperature and Pressure are respectively 1 K and 0.1 MPa and they are kept constants in the whole domain. A more computationally efficient approach would be to implement a variable step size as adopted in the work by De Lorenzo et al.

[22]. However, sensitivity analyses performed on the lookup-table step size (see later) has revealed that an adequate level of accuracy can be achieved without an excessive refinement and computational cost. Therefore, this method was adopted in the present work.

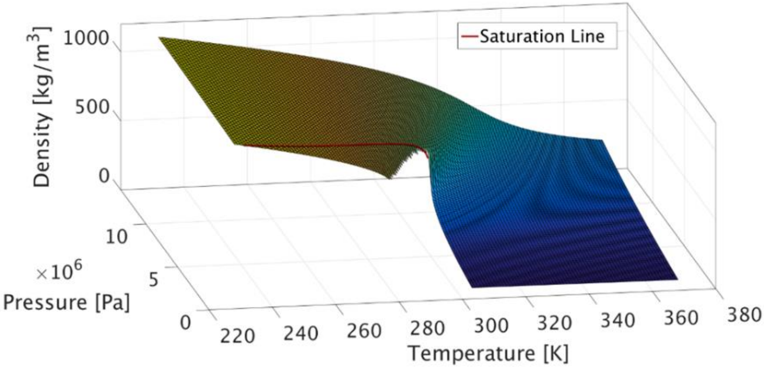

Figure 48 Density lookup-table as function of pressure and temperature with saturation line

All the lookup-tables are read and loaded in the Random Access Memory (RAM) before the start of the calculation. At runtime, the solver operates bi-linear interpolations (similarly to [72]) in terms of pressure and temperature to calculate the local value of the various properties. The procedure of loading and interpolating the tables is developed by means of C code programming with a total of 44 additional functions included in the header files of the Multispecies-UDRGM. An analysis of sensitivity to the table resolution has also been performed in order to evaluate the impact of subsequent refinement on the computational time and accuracy. This will be further discussed in next sections.

The properties (with corresponding units) needed to define the UDRGM for both liquid and vapor are:

- Density [kg m^{-3}]
- Enthalpy [J kg^{-1}]
- Entropy [J kg^{-1} K^{-1}]
- Specific heat at constant pressure [J kg^{-1} K^{-1}]
- Molecular weight (this is a constant value, so the lookup-table is not needed) [kg kmol^{-1}]
- Speed of sound [m s^{-1}]
- Dynamic viscosity [kg m^{-1} s^{-1}]
- Thermal conductivity [W m^{-1} K^{-1}]
- $\left(\frac{\partial \rho}{\partial T}\right)_{P=const.}$ [kg m^{-3} K^{-1}]
- $\left(\frac{\partial \rho}{\partial P}\right)_{T=const.}$ [kg m^{-3} Pa^{-1}]
- $\left(\frac{\partial h}{\partial T}\right)_{P=const.}$ [J kg^{-1} K^{-1}]
- $\left(\frac{\partial h}{\partial P}\right)_{T=const.}$ [J kg^{-1} Pa^{-1}]

The computational domain is a half of the 2D planar section of the nozzles tested by Nakagawa et al. [79]. Four geometries have been investigated in [79], which differ for the diverging angle of the nozzle. However, only the two geometries that have pressure trends above the triple point have been selected, namely nozzle A and B (although the Span and Wagner EOS

can be extrapolated below the triple point, the possibility of ice formation demand for a deeper analysis and a specific study of the problem). A list of the tested inlet boundary condition is summarized in

Table 5 for each nozzle. The representation of the Inlet boundary condition on the CO_2 P-h diagram is also visible in Figure 49.

The experimental data available from the work of Nakagawa et al. [79] are the static pressure and temperature at the side walls of the nozzle obtained from differential pressure gauge and thermocouple taps. The temperature trends were reported by Nakagawa et al. [79] as saturation pressures, assuming thermodynamic equilibrium. These have been converted back into temperatures values in order to compare both pressure and temperature trends with the computational results.

Table 5 Inlet boundary conditions

Case	Θ [°]	Total Pressure [MPa]	Total Temperature [K]	α_v [-]
1	0.076	9.1	310.15	0.0
2		6.1	293.65	0.0
3	0.153	9.1	310.45	0.0
4		6.1	293.15	0.0

The main geometrical parameters as well as the diverging angles (θ) of the investigated nozzles are shown in Figure 50. Adiabatic Wall (with no slip condition) and Symmetry boundaries are adopted according to Figure 50. A two-equations k-ω SST turbulence model is selected for all the calculations.

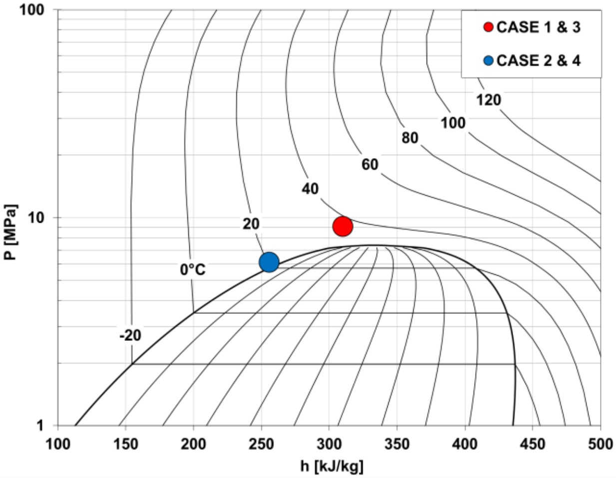

Figure 49 p-h diagram of CO2 with representation of Nozzle Inlet boundary conditions

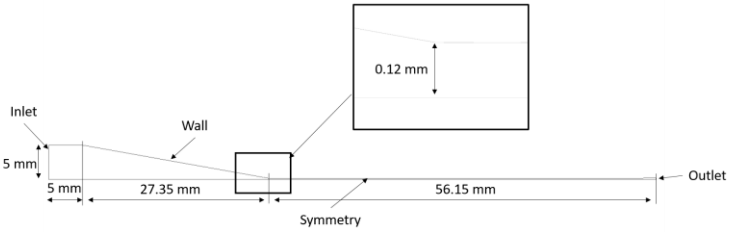

Figure 50 Nozzle Geometry with main quotes.
The outlet heights are 0.195 mm and 10.27 mm corresponding to diverging angles (θ) of 0.076° and 0.153°, respectively

The choice of 2D geometry was made in order to save computational cost. The 12000 quadrilateral elements mesh is shown in Figure 51. The values of wall y^+ are above 11 everywhere with the exception of the very beginning of the converging part of the nozzle where velocity is very slow. However, the k-ω SST in ANSYS fluent is based on a y^+ insensitive approach so that different values of this parameter along the domain do not affect the solution in a significant manner.

A pressure-inlet boundary condition has been used for the nozzle inlet. Several conditions have been tested at the outlet, as discussed in the next section. All the calculations have been performed using a pressure-based solver with pressure-velocity coupling. The discretization schemes are finally summarized in Table 6.

Table 6 Numerical Setup Summary

Discretization schemes adopted	
Quantity	**Method**
Gradients	Least Squares Cell Based
Pressure	PRESTO
All Others	3rd Order QUICK

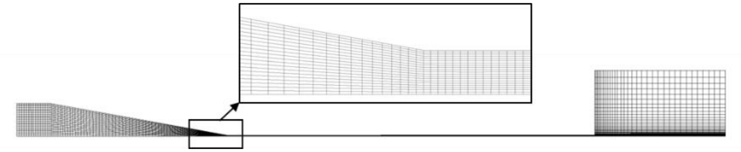

Figure 51 Computational Mesh with zoom near the nozzle throat

Several preliminary calculations have been performed in order to test the model sensitivity to various numerical parameters:

- Mesh refinement;
- Lookup-tables refinement;
- Outlet geometry and boundary conditions;
- Evaporation factor σ_e

The condensation factor, σ_c, was found to have a negligible impact on the results, due to the scarce condensation occurring in the nozzle. Hence, a sensitivity analysis on this parameter has not been performed and will be addressed in future work related to full ejector CFD simulations, where the condensation factor is expected to have more influence.

The mesh sensitivity results are presented in Figure 52 for Case 2 of Table 5

Table 5 Inlet boundary conditions (reference case) which shows a substantial equivalence of the three meshes with the exception of the plenum zone where the 50 000 elements mesh shows the presence of strong variations of pressure due to the mismatching of the nozzle exit pressure and imposed outlet pressure. Since the physics of the flow inside the plenum is not of interest in this work, the 12 000 elements mesh, also shown in Figure 51, was selected for all subsequent calculations.

The 12000 elements mesh analysis shows a good agreement with the experiments for both pressure and temperature and the values of the percentage errors for pressure and temperatures are shown in Table 7. As can be seen the agreement with measured temperatures is better than the one of pressures. In this latter case the CFD results are within the range of ±4.5% with the exception of the last pressure sensor; nevertheless, it is seen that for both pressure and temperature profiles, the experimental results are qualitatively well reproduced.

Table 7 Values of relative errors between CFD and Experiments. Sensors are numbered starting from nozzle inlet

Percentage Errors		
P_1= 2.9 %	T_1 = -0.57 %	T_6 = -0.31 %
P_2 = 2.3 %	T_2 = -0.19 %	T_7 = -0.35 %
P_3 = -4.4 %	T_3 = -0.01 %	T_8 = -1.09 %
P_4 = -19.1 %	T_4 = -0.01 %	T_9 = -2.53 %
	T_5 = -0.24 %	

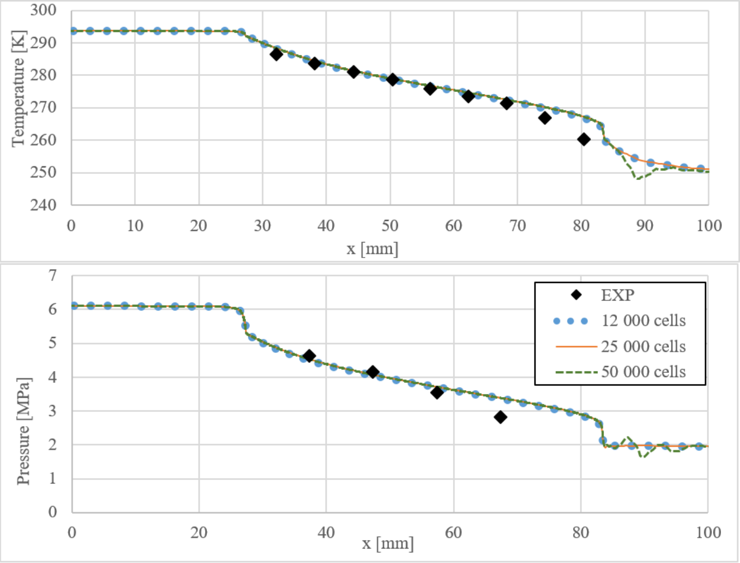

Figure 52 Mesh sensitivity: Symmetry data from the results of the geometry of Nozzle with Plenum

Figure 53 illustrates the effect of the refinement of the lookup tables for Case 2.

In the “Refined Tables” case, the lookup-tables were refined by approximately 5 times compared to the coarse case. Clearly, the results do not show significant variation between the two cases, with the 2 lines that are almost undistinguishable in the plots. By contrast, the computational time needed to achieve convergence increase by almost a factor of 4 for the refined case.

Table 8 shows the relative errors of the main thermodynamic quantities resulting from the CFD calculation with respect to the NIST Refprop libraries values for all the points along the nozzle symmetry axis. NIST values are calculated at the same pressure and temperature of the computed ones. The resulting errors, presented for both coarse and refined lookup tables, show a good agreement with respect to the values from Refprop database. The highest error that can be noted is for the vapor specific heat in case of coarse tables and is below 1.6% of absolute value.

Figure 54 shows the plot of liquid and vapor density along the nozzle axis of symmetry for the case of coarse lookup table. The corresponding NIST Refprop values, calculated at the same local pressure and temperature are also shown in the plot as well as the vapor volume fraction. The difference between computed and Refprop libraries values is negligible. Consequently, given also the advantage of reduced computational cost, the coarse tables have been preferred for all the calculations.

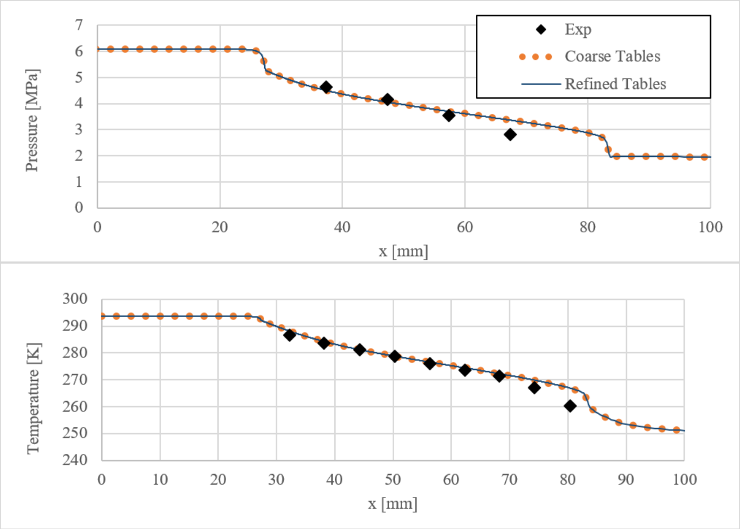

Figure 53 Tables refinement sensitivity. Symmetry data from the results of the geometry of Nozzle with Plenum

Since the Mach number in a two-phase mixture does not have a univocal definition (a detailed discussion of this problem is given in Section 3.2), the condition of supersonic chocked outflow was believed to be a potential issue. In order to check the presence of critical flow at the throat, the mass-flow rate was verified to remain constant while varying the outlet pressure of the nozzle. In many cases, despite the Mach number at the outlet is supersonic, the absolute pressure of the flow was found to match the static pressure imposed at the boundary. This flow behavior is typical of subsonic regimes and is probably due to the inability of the software in properly evaluating the supersonic outlet conditions for a mixture flow.

Consequently, a sensitivity analysis was performed to investigate whereas different outlet boundary conditions (BC) and geometries could have an impact on the results. Three different conditions have been tested:

- Pressure-outlet BC imposed at the nozzle outlet without modification to the geometry of Figure 50;
- Addition of a plenum 20 mm long and 10 mm high with static pressure imposed at the plenum outlet;
- Addition of a diverging section with a diverging angle of 11.3° and static pressure imposed at the diverging section outlet.

Figure 55 illustrates the sketches of the different geometries tested.

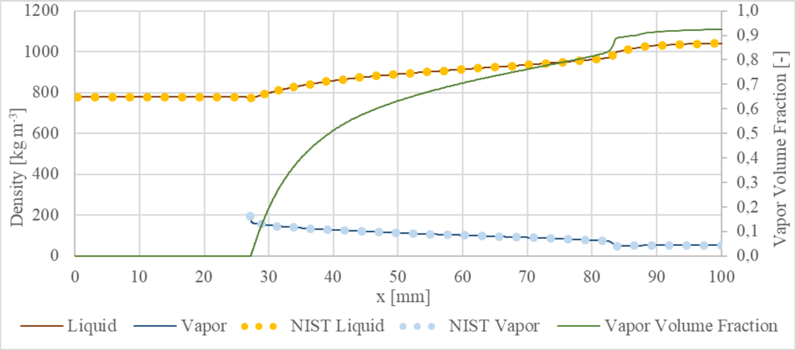

Figure 54 Density along the nozzle symmetry compared to NIST Refprop libraries results. The vapor volume fraction is also plotted

Figure 55 Different tested outlet geometries

Table 8 Minimum, Maximum and Average error of main thermodynamic quantities along the nozzle symmetry axis with respect to NIST Refprop libraries values

COARSE TABLES										
	LIQUID					**VAPOR**				
	ρ	h	cp	k	μ	ρ	h	cp	k	μ
MAX ERR [%]	0.04487	-0.00017	-0.00063	0.00623	0.05774	-0.00423	0.03298	-0.01704	-0.00535	-0.00074
MIN ERR [%]	0.00013	-0.02579	-0.71406	-0.01531	-0.00520	-0.15844	0.00057	-1.56289	-0.49593	-0.06385
AVERAGE ERR [%]	0.01097	-0.00691	-0.14024	0.00094	0.01194	-0.03804	0.00589	-0.19603	-0.06459	-0.00934
REFINED TABLES										
	LIQUID					**VAPOR**				
	ρ	h	cp	k	μ	ρ	h	cp	k	μ
MAX ERR [%]	0.00227	-0.00003	-0.00010	0.00024	0.00320	0.00222	0.00464	-0.00082	-0.00031	0.00031
MIN ERR [%]	0.00002	-0.00128	-0.03302	-0.00075	-0.00332	-0.02866	-0.00042	-0.17776	-0.05970	-0.00886
AVERAGE ERR [%]	0.00041	-0.00027	-0.00529	0.00003	0.00039	-0.00186	0.00027	-0.00937	-0.00314	-0.00047

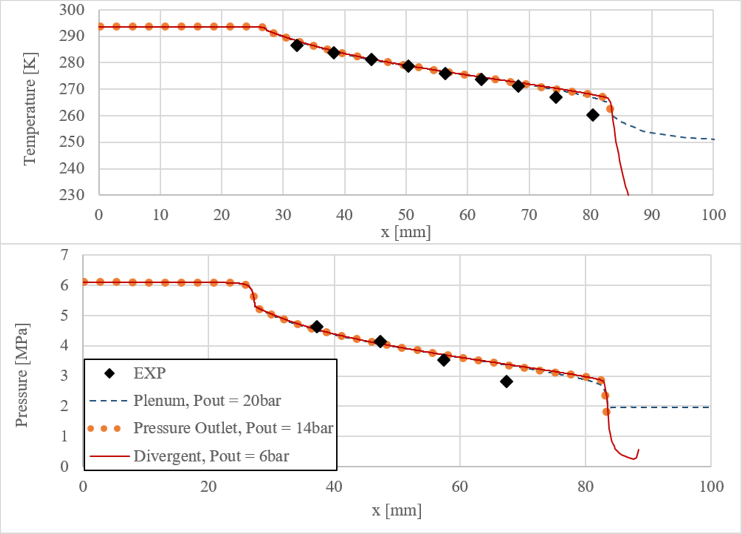

Figure 56 Outlet sensitivity analysis results. Symmetry data from the results of the different geometries of Nozzle Outlet

The results of the comparison are presented in Figure 56. Both pressure and temperature profiles inside the nozzle (x < 85 mm) seem to be scarcely affected by the outlet geometry. The calculation of the plenum caused an increase in computational time and convergence instabilities due to the presence of unsteady flow features, such as recirculation at the plenum outlet and vortex shedding at the nozzle outlet. Nevertheless, the case with the plenum was considered to be the most reliable because no boundary condition has to be imposed at the nozzle outlet that affects the solution in unphysical ways. Moreover, a plenum is also present in the experimental set-up of Nakagawa et al. [79]. Consequently, all subsequent results refer to computational domains with a plenum at the outlet.

Finally, Figure 57 shows the effect of varying the evaporation factor for case 2. The comparison is made by varying by two order of magnitudes the value of the σ_e coefficient in Equation 7 (from 1x10^4 up to 1x10^6).

As can be seen, a lower value of the evaporation coefficient results in a higher temperature trend along the nozzle axis. This is particularly evident for $\sigma_e = 10000$ (blue line in Figure 57), although a slight difference can be also seen between the other two cases. This temperature variation depends on the latent heat that is absorbed by the flow when part of the CO$_2$ liquid mass evaporates.

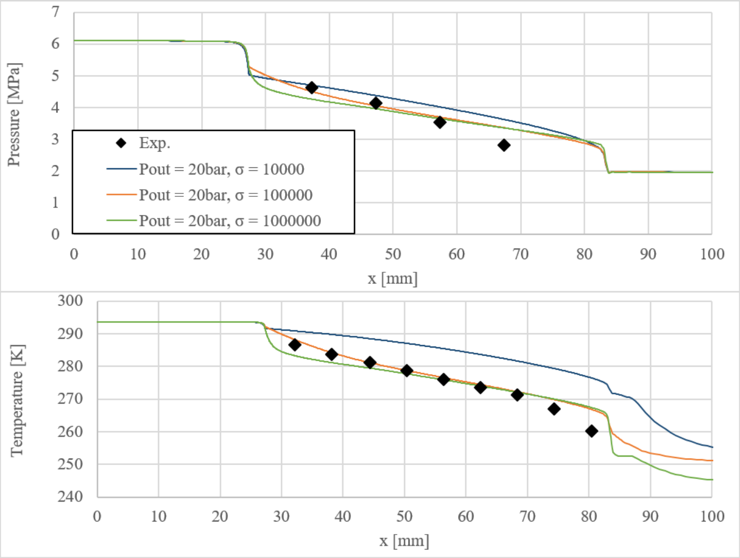

Figure 57 Evaporation coefficient sensitivity. Symmetry data from the results of the geometry of Nozzle with Plenum

In a similar way, the pressure decrease is generally more evident with a higher evaporation coefficient. This is due to the increase in vapor volume fraction, which leads to a significant acceleration of the mixture. In turn this causes a further pressure reduction due to the augmented friction losses.

For Case 2, the best agreement with experiments is achieved by imposing $\sigma_e = 10^5$ (orange dotted line in Figure 57). The same analysis was made for all the investigated cases and returned similar results. Therefore, only the solutions with $\sigma_e = 10^5$ will be presented in subsequent analyses.

The comparison of numerical results and experiments for Case 1 are shown in Figure 58. The agreement with experimental data is good in the first half of the nozzle divergent, while the computed pressure and temperature are higher than the experiments in the second half of the nozzle length. These discrepancies are possibly due to an underestimation of the vapor volume fraction formed during the flashing process. Case 1 is the least accurate among all the presented cases. The maximum absolute values of relative errors for pressure and temperature, compared to the experimental values, are respectively: 34 % and 6.5 %. In all the other cases lower percentage errors have been obtained.

Moreover, for this case it was found that the pressure and temperature go beyond the liquid phase spinodal limit in some cells. This problem is connected to the assumption of thermal and mechanical equilibrium between the phases. In particular, the Mixture-Model approach requires the use of a shared pressure and temperature between the phases. In cases where the CO_2 expansion is well within the saturation dome (e.g., qualities close to 0.5, such as in Case 1), the mixture state can cross regions where one of the two phases is beyond the Spinodal limit.

The adoption of a full Eulerian-Eulerian model should overcome this issue. Some preliminary tests, not presented in this paper, have been performed and will be the subject of subsequent studies.

Figure 59 shows the pressure and temperature trend for Case 3. Clearly, a better agreement with the experimental results is visible. However, a sudden pressure jump can be noted near the nozzle outlet, which is due to the presence of a shock-wave. This behavior is only visible in nozzle B, which has a larger diverging angle with respect to nozzle A. This issue will be further commented in the next section.

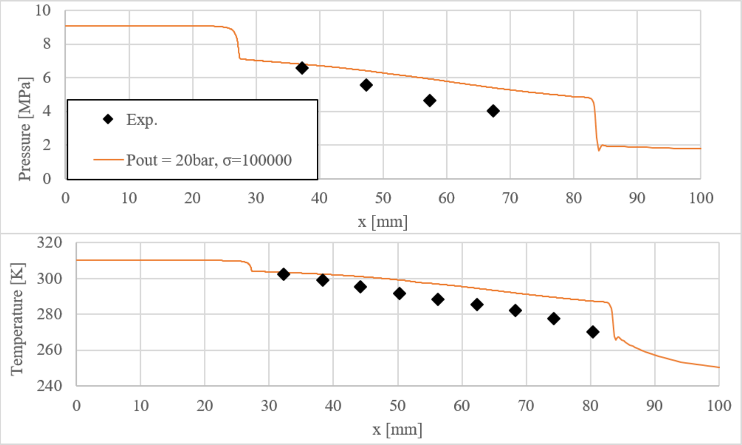

Figure 58 Case 1. Numerical results vs. experiments (Nozzle A)

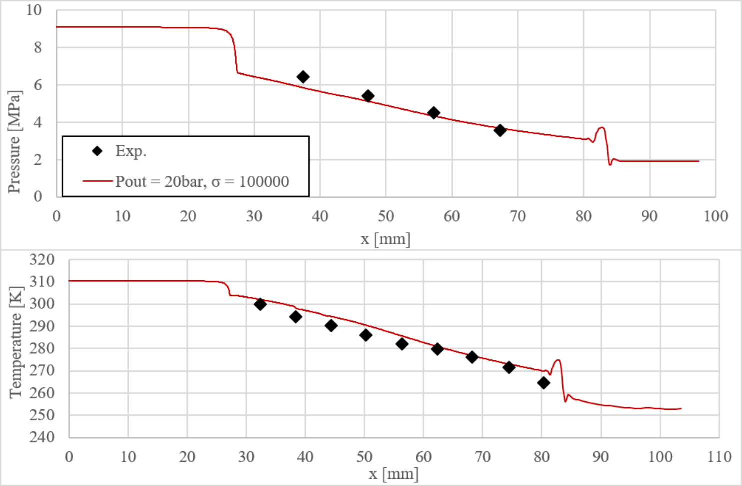

Figure 59 Case 3. Numerical results vs. experiments (Nozzle B)

Figure 60 illustrates the contours comparison of vapor volume fraction, superheating and density gradient, between the two different tested geometries. In order to have a better visualization of the maps, the axial coordinate in all the contour plots has been scaled by $D_{th}/4$, where D_{th} is the throat hydraulic diameter. Moreover, only the divergent and the region close to the nozzle throat is showed.

The superheating is defined as the difference between the local temperature and the saturation temperature at the local pressure. When the superheating is above zero the liquid is in metastable state. Practically, this occurs all along the diverging part of the nozzle. In addition, it should be noted that in both cases the superheating reaches values above zero before the nozzle throat, although this is more evident in the contour of case 3.

The density gradient contour illustrates the regions of the computational domain where the phase change is more intense. In particular, the region with the highest density gradient is immediately downstream of the nozzle throat, where the wall corner induces a low pressure region that causes a significant flashing.

The direct comparison of two different geometries with similar inlet boundary conditions help visualizing the resulting differences caused by the wider diverging angle. For instance, the maximum value of vapor volume fraction is greater in case 3 because of the more abrupt expansion. Moreover, the nozzle outlet pressure is lower in case 3 and it causes the formation of a shock-wave near the nozzle exit. In turn, the shock-wave leads to a partial condensation of the vapor phase.

The numerical results of Case 2 have already been compared to the experiments in Section 3.4 and will not be repeated here. The results for Case 4 are presented in Figure 61. A good agreement with the experimental data is visible. As in Case 3 (which has the same geometry), a shock-wave appears near the nozzle exit.

According to the contours of Figure 62 the volume fraction after the shock-wave slightly decreases because of the condensation connected to the pressure rise. In this respect, a sensitivity analysis on the condensation factor σ_c may produce a better agreement of the results even with the last thermocouple of Figure 61.

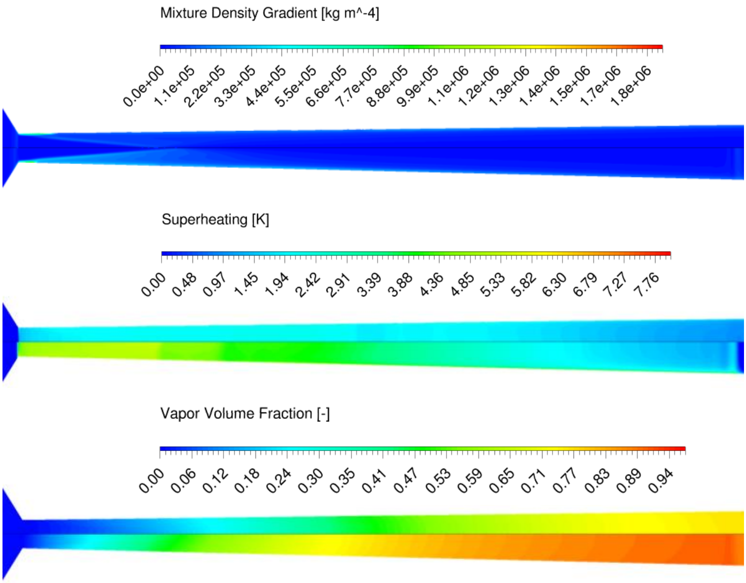

Figure 60 Case 1 (TOP) vs Case 3 (BOTTOM). Contour Comparison. (Out of scale)

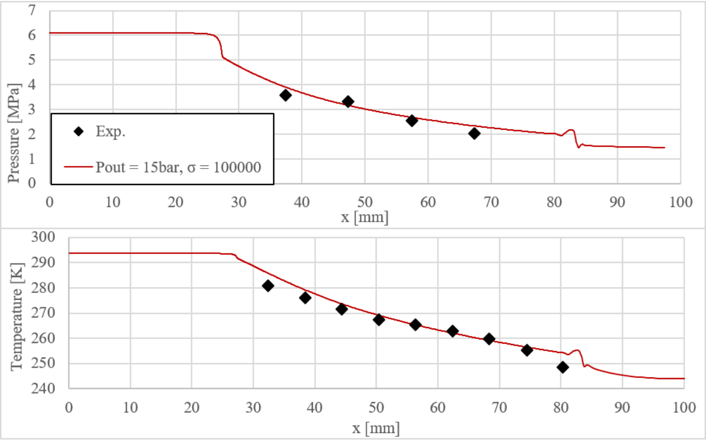

Figure 61 Case 4. Numerical results vs. experiments (Nozzle B)

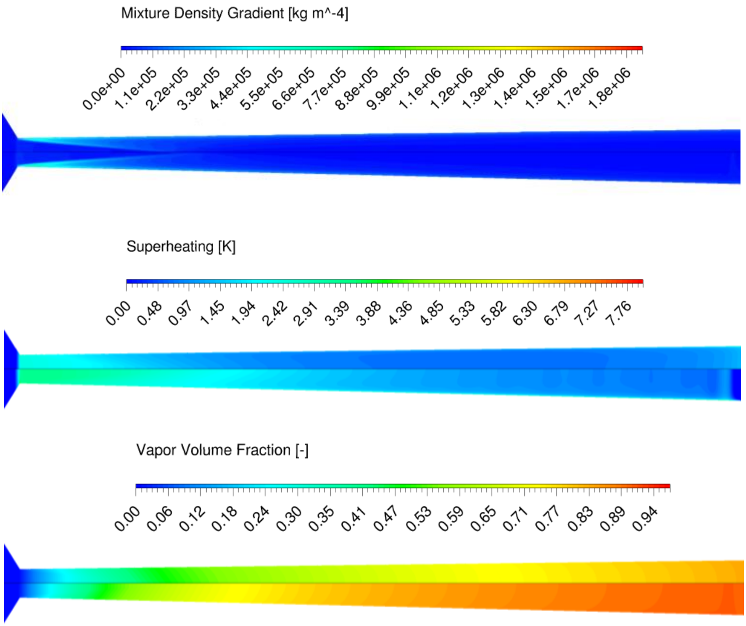

Figure 62 Case 2 (TOP) vs. Case 4 (BOTTOM). Contour Comparison. (Out of scale)

In order to analyze in greater detail the effect of the supersonic condition, the Mach number was calculated in post-processing by means of a different equation for the mixture speed of sound, in analogy to the work of Yazdani et al. [76].

The equation was derived by Brennen [21] by applying an incremental pressure to a mixture of liquid and vapor. It assumes homogeneous equilibrium model (instantaneous heat transfer between the phases) and homogeneous frozen model (no heat transfer between the phases) as extreme cases of validity. It was already presented in Chapter 1 and it is reported here for clarity:

$$\frac{1}{\rho a^2} = \frac{\alpha_v}{P}[(1-\varepsilon_v)f_v + \varepsilon_v g_v] + \frac{1-\alpha_v}{P}\varepsilon_l g_l \qquad (3.11)$$

Where f and g are functions of the thermodynamic properties of the fluid while ε_v and ε_l are the interacting portions, i.e. portion of phase that exchange heat with each other, of vapor and liquid respectively. The equation was eventually simplified according to the suggestions of the same author:

- $f_v \approx 1$;
- $g_v \approx 1$;
- $\varepsilon_v \approx (1-\alpha_v)$;
- $\varepsilon_l \approx \alpha_v$;
- $g_l \approx 2.1\left(\frac{P}{P_{critical}}\right)^{-0.566}$

In Figure 63 the contours of Mach Number calculated with the Brennen Equation (Equation (1.8)) and the Wallis Equation (Equation (1.4)) are compared along the nozzle diffuser and a portion of the plenum. The sonic lines of both cases are also visible.

The sonic line and Mach contour obtained with the Brennen equation seem to be in better agreement with the behavior of the flashing flow. In particular, the flow becomes supersonic in the diffuser and continues to accelerate until a shock-wave occurs, where a part of the flow becomes subsonic.

The contour obtained with Eq. (1.4) shows a similar trend with an abrupt acceleration that resemble a shock-wave. However, the Mach number in this case is below 1, which is in contrast with the predicted flow trend. Downstream of the nozzle exit plane, the jet spreading is clearly visible in both cases.

In this comparison, the Wallis Equation for the mixture sound speed seems not completely appropriate to represent the mixture flow, resulting in Mach numbers that do not reflect the computational results. Perhaps, the issue in the proper evaluation of supersonic outlet condition could possibly be solved by implementing a different equation, similar to Equation (1.9), for the mixture speed of sound. Unfortunately, the Wallis expression is the default equation implemented in ANSYS Fluent and it cannot be modified by the user. According to ANSYS documentation [78] the speed of sound is used to solve the pressure-correction equation but further details are not available since it is not an open-source code.

Moreover, it should be noted that both the Wallis and Brennen equations are only "post-process" definition of the sound speed which in no way impact the final numerical solution. The actual numerical speed of sound stems mathematically from the governing systems of equations, and it depends on the choice of the equation of state [22].

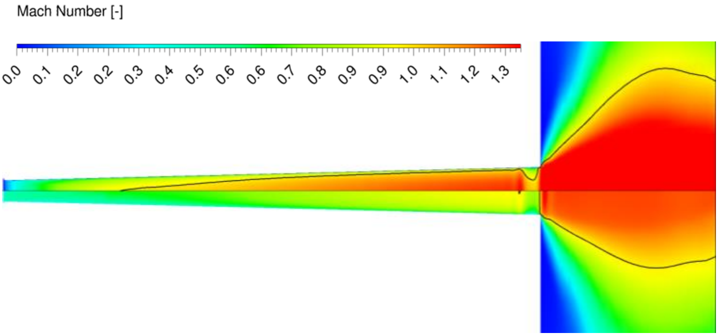

Figure 63 Case 3. Mach Number with Brennen Equation (TOP) vs Mach Number with Wallis Equation (BOTTOM) with sonic lines. (Out of scale)

In conclusion of the present section, some comments to summarize the main findings and results will follow.

A novel method to perform CFD calculations of flashing CO_2, implemented on the commercial solver ANSYS Fluent v.19.0 by means of *User-Defined-Functions* was presented. The main feature of the method is the possibility of defining the properties of both phases by means of lookup-tables obtained from NIST Refprop v.9.1 libraries including liquid, vapor, supercritical and metastable states. This automatic procedure of implementing the properties is based on several VBA and C code functions and it can be easily adapted to virtually any kind of fluid in both single and two-phase flows.

The numerical simulations were compared to the experimental results available from literature with satisfactory agreement. The pressure and temperature profiles are qualitatively well reproduced except in Case 1, the least accurate among all the presented cases, where the maximum absolute values relative errors for pressure and temperature (with respect to the experimental values) are respectively: 34 % and 6.5 %.

A comparison between two different equations for the mixture speed of sound has also been performed which illustrated that the Brennen formulation may be more accurate than the expression derived by Wallis and used as a default equation by commercial software adopted in this work.

3.3 CO_2 Ejector: Experimental Part

Experimental activity on ejector-equipped systems is also extremely important at both system and component level and several works are available in the literature in this field. Banasiak et al. [15] conducted a detailed experimental investigation about the influence of the ejector geometry on the efficiency of this component. Elbel and Harnjak [14] focused on the performance of a transcritical R744 system equipped with an ejector. As a final example, Banasiak et al. [86] made an extensive performance mapping of ejectors in the "multipack" device (multiple ejectors in parallel). In the experimental part of the present work the focus was on the ejector itself and the purpose was to use the obtained experimental results to benchmark and validate the CFD model.

The experimental part of this work was conducted at the SINTEF Energy and NTNU lab in Trondheim, Norway. The experimental setup was described in detail in Banasiak et al. [15]. The only difference from that work is a slight modification of the ejector geometry and system layout in order to obtain a higher pressure lift of the tested ejector. The actual layout is depicted in Figure 64. Heat input and output are provided to the system via two separate glycol loops at the evaporator (blue) and the gas cooler (red), while additional heat is provided at the air heat exchanger (green) in order to achieve a higher pressure lift of the ejector.

For more detailed description of all the components of the test-rig, the reader is referred to Banasiak et al. [15].

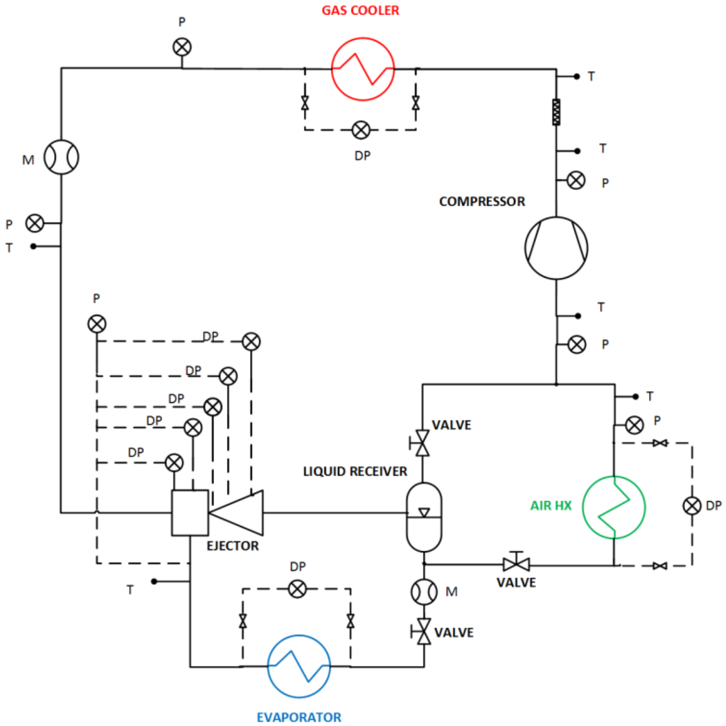

Figure 64 Experimental test-rig layout. T: T-type thermocouple P: pressure sensor DP: differential pressure sensor M: Coriolis mass-flow meter

The measurement system (see Figure 64) was based on temperature sensors (T-type thermocouples), absolute and differential pressure sensors (piezoelectric elements), and mass flow meters (Coriolis-type). The uncertainties for all the measured quantities are evaluated considering both instrument and random errors with the following equation:

$$\varepsilon = \sqrt{(\sigma^2 + \varepsilon_i^2)} \qquad (\ 3.12\ )$$

where σ is the standard deviation of the measured value and ε_i is the instrument error. For the derived quantities, the following equation was used instead:

$$\varepsilon = \sqrt{\sum_i \left(\frac{\partial f(x_i)}{\partial x_i}\delta x_i\right)} \qquad (\ 3.13\ )$$

where $f(x_i)$ is the derived quantity, while x_i are the measured quantities. $\frac{\partial f(x_i)}{\partial x_i}$ is known as "sensitivity index", which in case of absence of an analytical formulation for the derived quantity (e.g., when evaluating the enthalpy of the refrigerant through NIST libraries), can be evaluated as follows [87]:

$$\frac{\partial f(x_i)}{\partial x_i} = \frac{1}{2}\left(\left|\frac{f(\bar{x}_i + \delta x_i) - f(\bar{x}_i)}{\delta x_i}\right| + \left|\frac{f(\bar{x}_i) - f(\bar{x}_i - \delta x_i)}{\delta x_i}\right|\right) \qquad (\ 3.14\ )$$

The mean values of the measurement uncertainties, including both sensor accuracy and the time-averaged deviations from steady state, were as follows: $\varepsilon(T) = \pm 0.3$ K, $\varepsilon(P) = \pm 15\text{x}10^3$ Pa, and $\varepsilon(\dot{m}) = \pm 0.5\text{x}10^{-3} \text{kg} \cdot \text{s}^{-1}$.

The main dimensions of the ejector are shown in Figure 65 and summarized in Table 9, where D_{FILLET} stands for the diameter at the end of the A part (motive nozzle part in Figure 65). The detailed ejector drawings with quotes as well as some pictures of the CO_2 test-rig can be found in the Appendix. With respect to the real ejector some geometry de-featuring has been operated to perform the CFD calculations (see Sections 3.4 and 3.5). The ejector also has a slightly swirled flow entering the secondary inlet. The suction nozzle connection pipe is not radial but has an angle of 62.5°. For the preliminary CFD analyses this feature of the device has been neglected and the suction flow is assumed to be axisymmetric. The error introduced with this assumption will be also discussed in Sections 3.4 and 3.5.

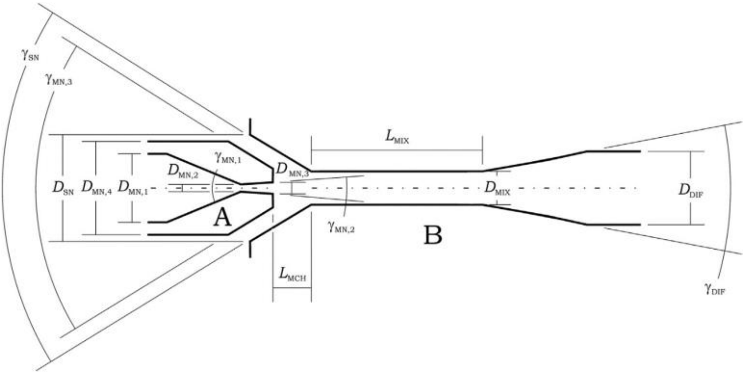

Figure 65 Basic dimensions of the ejector geometry. A is motive nozzle piece, and B is suction nozzle, mixer and diffuser piece

Table 9 Main ejector dimensions

Motive Nozzle	$D_{MN,1}$, 10^{-3} m	6
	$D_{MN,2}$, 10^{-3} m	0.9
	$D_{MN,3}$, 10^{-3} m	1.03
	$D_{MN,4}$, 10^{-3} m	12
	$\gamma_{MN,1}$, °	30
	$\gamma_{MN,2}$, °	2
	$\gamma_{MN,3}$, °	42
	D_{FILLET}, 10^{-3} m	3.5
Mixing Chamber and Diffuser	L_{MCH}, 10^{-3} m	7.5
	D_{SN}, 10^{-3} m	18.8
	γ_{SN}, °	42
	D_{MIX}, 10^{-3} m	2
	L_{MIX}, 10^{-3} m	16.9
	D_{DIF}, 10^{-3} m	10
	γ_{DIF}, °	5

The motive and suction nozzle conditions of full set of collected experimental data are shown in the P-h diagram of Figure 66, where the colour of the marks represent the range of ejector efficiency, as defined in Chapter 1. The same set of points is also plotted in Figure 67 as function of two of the main performance parameters of the ejector: entrainment ratio and pressure lift. The colour scheme again represents the ejector efficiency.

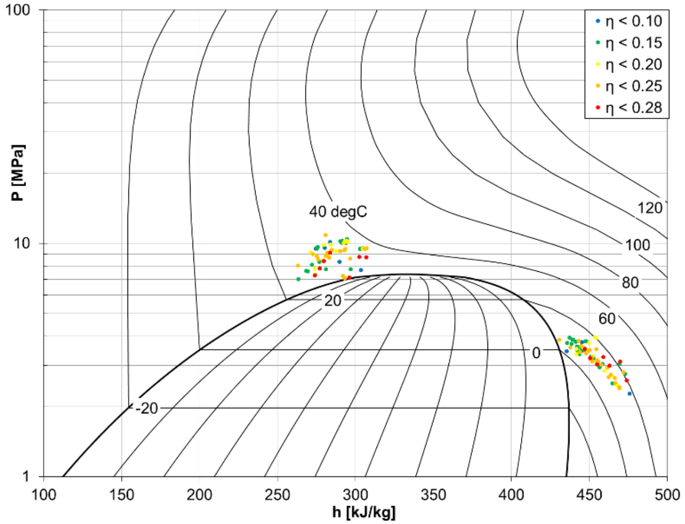

Figure 66 P-h diagram of experimental conditions at inlets with ejector efficiency

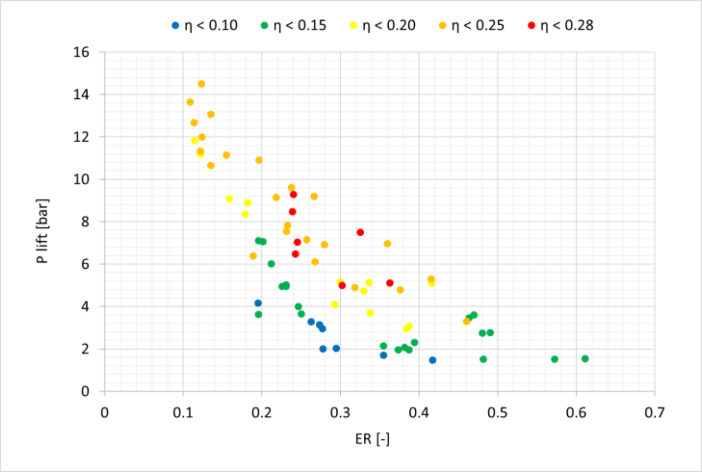

Figure 67 Non-dimensional performance parameters plot

Among all the experimental points, a set of ten cases have been chosen for the comparison with the computational results. Table 10 summarizes all the selected cases. Figure 68 presents the three performance curves of the ten cases as functions of the adimensional parameters. Each curve was experimentally obtained by adjusting the throttling valve before the suction nozzle of the Ejector. In facts by closing the throttling valve one can obtain a lower entrainment ratio, so the available energy at the motive nozzle inlet is used to increase the overall pressure lift instead of entraining the mass flow rate from the suction nozzle. These experimental results have also been compared to the numerical ones, as shown in the next section.

Table 10 Tested Case Boundary Conditions. MN = Motive Nozzle; SN = Suction Nozzle; OUT = Outlet

Case	$\mathbf{P_{MN}}$ **[MPa]**	$\mathbf{T_{MN}}$ **[K]**	$\mathbf{P_{SN}}$ **[MPa]**	$\mathbf{T_{SN}}$ **[K]**	$\mathbf{P_{OUT}}$ **[MPa]**
1	9.48	310.1	3.86	282.8	4.13
2	9.49	310.3	3.59	283.4	4.10
3	9.50	310.6	3.38	282.2	4.08
4	9.52	310.8	2.93	286.7	4.02
5	9.53	303.5	3.46	281.3	3.96
6	9.53	303.5	3.60	281.7	3.97
7	9.49	303.6	3.55	282.6	3.95
8	8.41	302.8	3.74	287.9	4.04
9	8.41	302.9	3.52	288.4	4.01
10	8.42	303.1	3.26	288.5	3.96

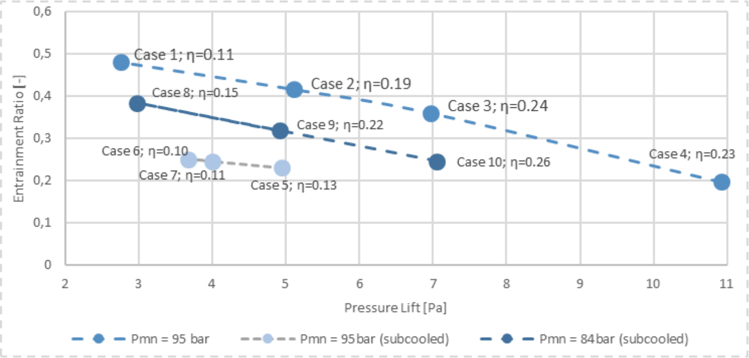

Figure 68 Experimentally obtained performance curves

3.4 Numerical Results: HEM

The computational domain consisting of 2D axis-symmetrical domain discretized in approximately 50000 quadrilateral elements is shown in Figure 69. The set of computed equation has been modified by substituting the standard energy equation with a Scalar Transport Equation of enthalpy. The turbulence model used in the present work is the 2 equations *k-ε Realizable* model with turbulent kinetic energy production limiter. All the equations are solved with a second order upwind spatial discretization method and a Least Squares Cell Based method for the gradients. The solver is a pressure-based solver with pressure velocity coupling. As mentioned in Chapter 2, the properties of R744 are evaluated assuming equilibrium phase change by means of lookup-tables obtained with an in-house developed MATLAB code. As an example the 3D plot of the CO_2 density is shown in Figure 70. The code allows the user to easily change the fluid in the computational model. For a more detailed description of the developed routines and the model description, the reader is referred to Chapter 2.

Figure 69 R744 ejector 2D mesh

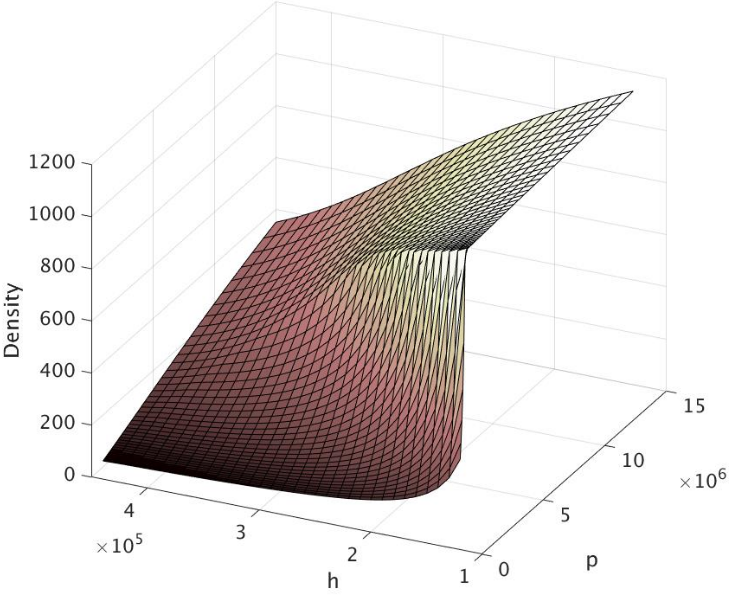

Figure 70 Density lookup table plot as function of Pressure and Specific Enthalpy

A mesh sensitivity analysis has been conducted in order to find the independency of the computational model from the number of mesh elements. The tested meshes had respectively 25000, 50000 and 100000 elements and the resulting mass flow rates for Case 1 at both inlets are plotted in Figure 71. The mass flow rate remains almost constant by increasing the number of elements, but, in case of a 100000-element mesh the overall error on the Mass Imbalance results in a higher value (approx. 1×10^{-4}). This is possibly due to the capability of the refined mesh to capture the flow instabilities nearby the diffuser shock leading to an increased mass imbalance error because of the steady state assumption made in the simulation, this was confirmed also by inspection of CFD results. Hence, the adopted mesh was the 50000 elements one, that showed low mass imbalance error combined to mass flow rates very similar to the most refined mesh.

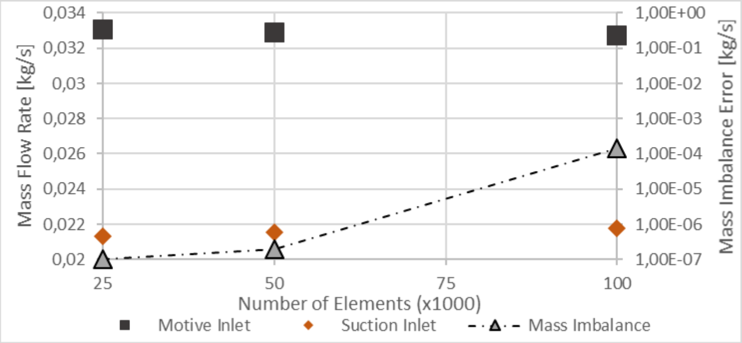

Figure 71 Mesh sensitivity for Case 1

One of the main criteria to evaluate the performance of the presented numerical model is the accuracy in the predicted mass flow rates. In Figure 72, the resulting mass flow rates at both motive and suction nozzle are shown and compared to the experimental results; the error between CFD and experiments is also plotted. The primary nozzle flow rate is better reproduced with a relative error between 12% and 19%. This discrepancy is possibly due to the inefficacy of the equilibrium model to predict the actual phase change phenomena, which resulted in an overestimation of the vapor volume fraction and, hence, an underprediction of the motive nozzle mass flow rate. The resulting suction mass flow rate from CFD calculations is considerably higher than experimental ones, which could be due to the aforementioned limitations of the computational model. Moreover, for these preliminary results, the swirl motion at the suction nozzle inlet has been neglected in favor of simplicity by considering an axis-symmetrical flow in the ejector. In the unchocked case (Case 4), a good agreement with experiments can be noticed.

The pressure profiles at the ejector wall are shown in Figure 73 and compared to the experimental results for Cases 1-4; the results of the remaining cases are similar. This comparison shows that the present model tends to place the shock position more downstream than the experimental value for all the chocked cases (Cases 1-3). However, the results at the wall are well predicted for Case 4 where the flow in the ejector mixer/diffuser is not in a chocked condition. The chocked/unchocked condition of the flow can be also seen in Figure 74, where the pressure contours of Case 1 (chocked) and Case 4 (unchocked) are compared. As can be seen, the shock-wave at the beginning of the diffuser is absent in Case 4, while the shock/expansion-waves at the motive nozzle exit have increased strength. Figure 75 shows the comparison of the density gradients contours of the two cases. Also in this case, the different strength of shock and expansion waves is evident. The start of the flashing process nearby the nozzle throat is also visible.

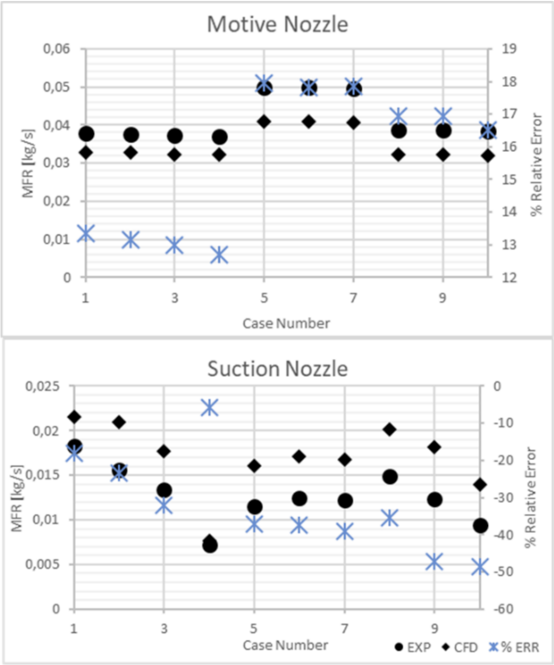

Figure 72 Mass Flow rate comparison between CFD and Experiments at both Motive and Suction Nozzles. (TOP) Motive Nozzle; (BOTTOM) Suction Nozzle

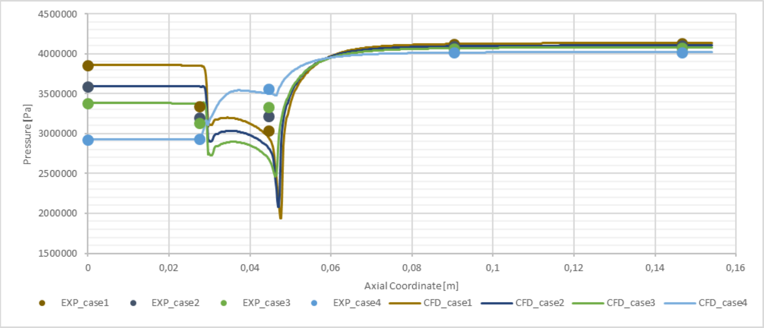

Figure 73 Pressure profiles comparison at ejector wall

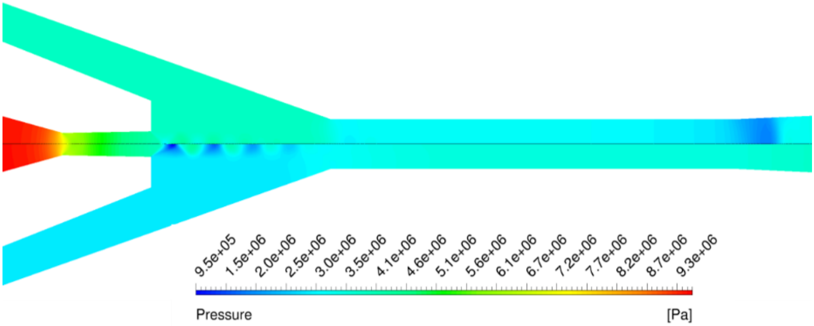

Figure 74 Pressure profile in Ejector Mixer/Diffuser. (TOP) Case 1; (BOTTOM) Case 4

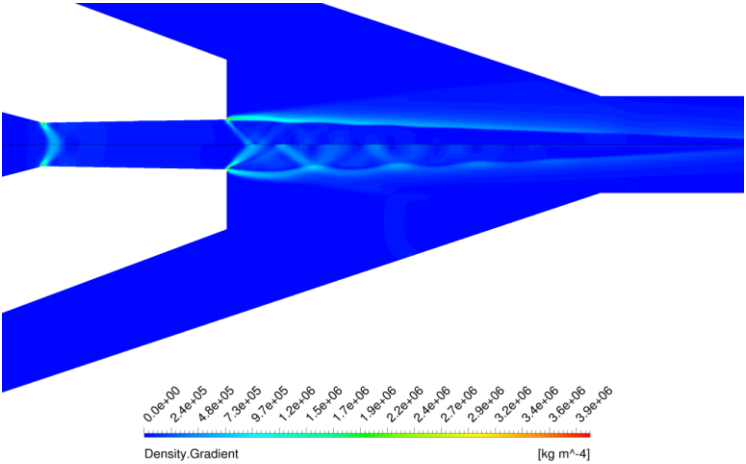

Figure 75 Density Gradient Contour (Numerical Schlieren). (TOP) Case 1; (BOTTOM) Case 4

This first comparison has shown the capability of the Homogeneous Equilibrium Model to predict the main flow features of flashing ejectors, especially for the unchoked conditions, which are common in this application. The described computational approach may be a useful tool because, notwithstanding its limitations, it may be still a valid tool to quickly obtain first results, thanks to its low computational cost and its flexibility in terms of adaptability to different fluids.

The next section will present the numerical results obtained with the computational model described in Section 3.2 compared to the experimental results of the CO_2 ejector. The improvements of the novel Mixture-model against the HEM will be also discussed.

3.5 Numerical Results: Mixture-Model

The same computational model described in Section 3.2 has been tested in the R744 ejector test-case. The geometry is the same shown in Figure 65. The swirled flow at the suction inlet has been modeled in an axis-symmetric domain by means of direction cosines. The angle formed by the suction nozzle inlet pipe with respect to the radial direction is visible in the Appendix and measures 62.5°. However, the angle between the flow direction and the inlet axis cannot be deduced from the geometrical features, so a sensitivity analysis has been performed for this parameter.

The evaporation factor σ_e in Equation (3.9) has been tuned to match the measured mass-flow rate of the motive nozzle, whilst

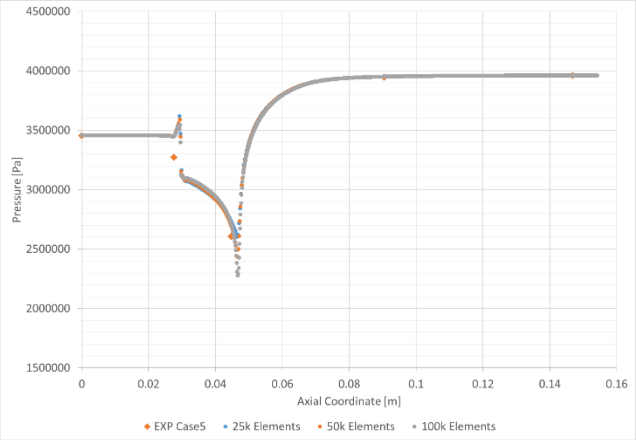

Figure 77 Pressure profiles for different meshes at the ejector wall with experimental data for Case 5

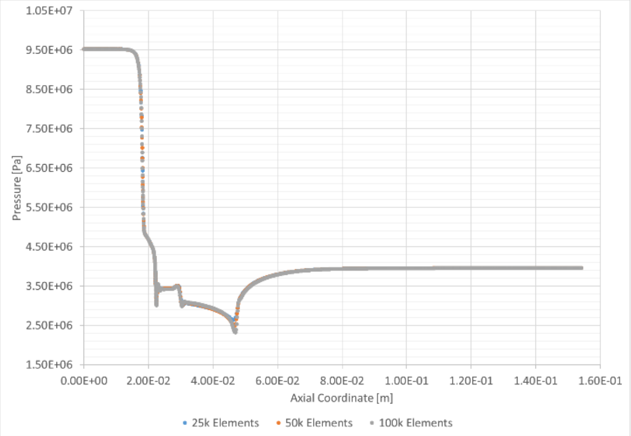

Figure 76 Pressure profiles for different meshes at the ejector axis for Case 5

for the condensation factor σ_c in Equation (3.10), a sensitivity analysis has been performed.

A mesh sensitivity analysis has also been performed for Case 5 (see Table 10), using a 25000, 50000 and 100000 quadrilateral elements meshes.

Figure 77 and Figure 76 show the pressure profiles obtained with the different meshes at the ejector axis and external wall respectively. The three meshes return basically the same results in terms of pressure and from Figure 78 a good agreement with the measurements can be seen.

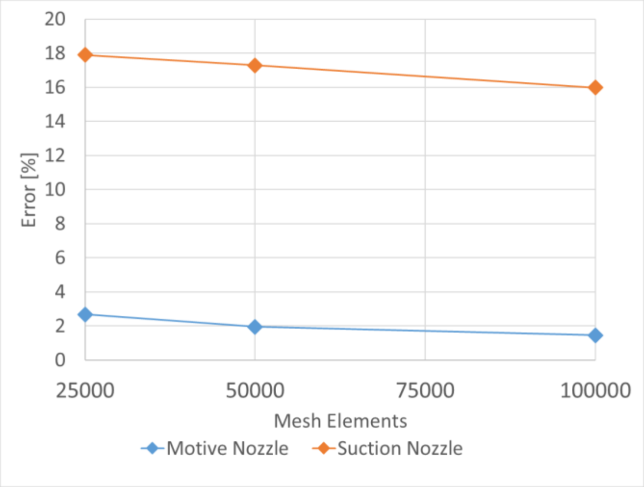

Figure 78 Error of the computed mass-flow rates with respect to the measured values for the different meshes

Figure 78 shows the percentage error of the computed values of both motive and suction nozzle mass-flow rates with respect to the measured ones. The trend of reduction of the error is clearly visible for both inlets. The variation between the computed mass-flow rates between 50000 and 100000 elements meshes are approximately 0.5% and 1.5% for motive and suction nozzle respectively. The variation between 25000 and 100000 elements meshes are approximately 1.3% and 2.3% for motive and suction nozzles respectively. So, the 50000 elements mesh has been selected for all the subsequent analyses.

For the condensation factor a sensitivity analysis has been performed in Case 5 by varying the order of magnitude of the coefficient from 0.1 to 10000.

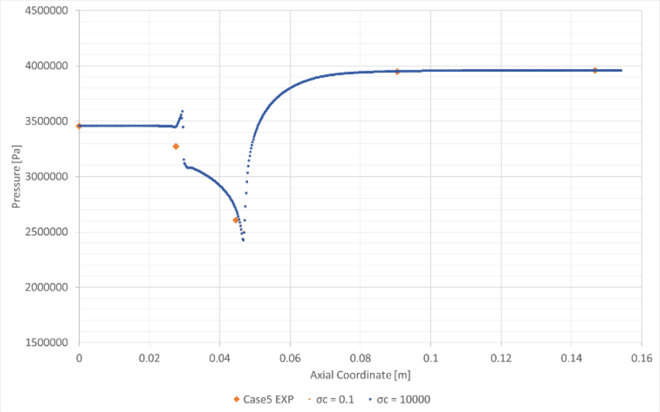

Figure 79 Pressure profiles at ejector wall for different condensation factors for Case 5

Figure 79 and Figure 80 show the resulting pressure profiles at ejector wall and axis respectively for the extreme values of condensation factor: $\sigma_c = 0.1$ and $\sigma_c = 10000$. The profiles are basically coincident, showing that this coefficient does not have a particular impact on the computational results. Also the mass flow rates values are basically coincident. As discussed in Section 3.2, the motive nozzle mass-flow rate is not affected by variations of σ_c.

From this sensitivity analysis, the suction nozzle mass-flow rates resulted in:

- $17.28\ kg \cdot s^{-1}$ for $\sigma_c = 0.1$
- $17.27\ kg \cdot s^{-1}$ for $\sigma_c = 10000$

Therefore, the mass-flow rates turn out to be insensitive to variations of the condensation factor of several orders of magnitude.

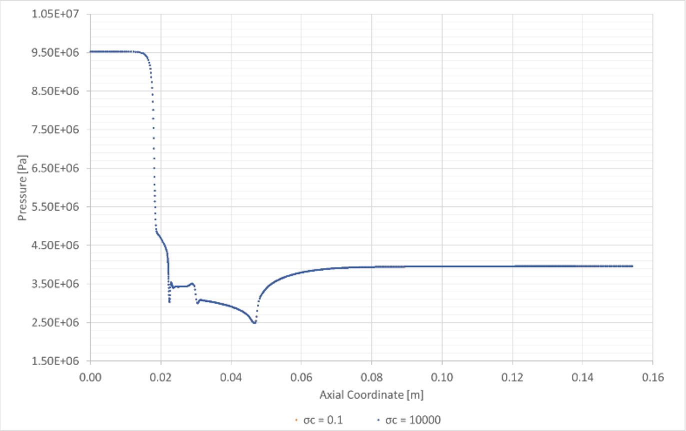

Figure 80 Pressure profiles at ejector axis for different condensation factors for Case 5

Finally, as already mentioned, the swirled suction flow has been modeled by means of direction cosines. In order to assess the angle between the flow the axial direction another sensitivity analysis has been performed. The geometrical angle of 62.5° has been kept constant. The wall pressure profile shown in Figure

81 does not show any significant variation for the different tested angles: 0°, 45° and 85°.

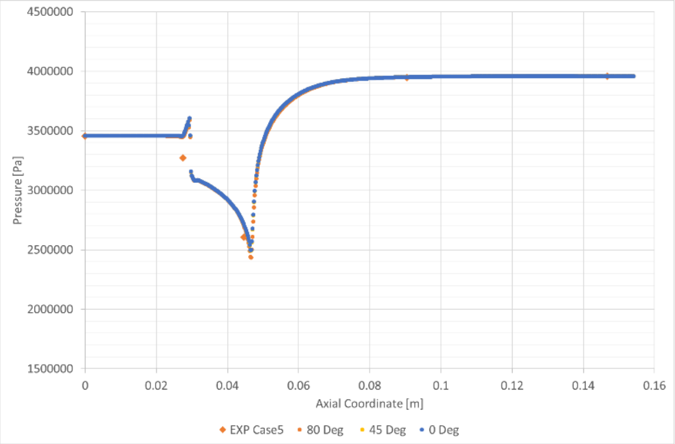

Figure 81 Pressure profiles at ejector wall for different angles for Case 5

The mass-flow rates of both motive and suction nozzles for different swirl angles are shown in Figure 82, where the errors with respect to the measured values are plotted on the secondary axes.

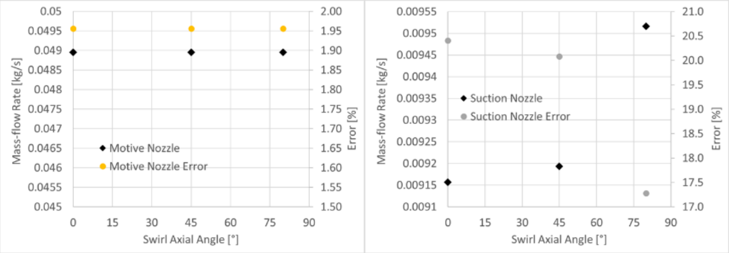

Figure 82 Computed mass-flow rates at different swirl angles and errors with respect to the experimental data. Motive Nozzle (LEFT) and Suction Nozzle (RIGHT)

As can be seen, the motive nozzle mass-flow rate is insensitive to the variations of suction nozzle angle, while this latter has an increasing mass-flow rate by increasing the swirl angle. In order to have a better agreement with the experiments, the 80° angle has been selected for all calculations. It is worth to remember that this is a brutal approximation and, in order to simulate the real flow behavior a full 3D analysis would be necessary. This 2D model is intended to be a first test and validation of the developed CFD model on the available experimental test-case with reasonable computational time.

All the cases (see Table 10 for boundary conditions) considered in this analysis are shown in Table 11. The values of the evaporation factor (σ_e in Equation (3.9)) are shown in Table 11 as well.

Table 11 Tested cases with errors of mass-flow rates with HEM and Mixture Model (MIX) and values of adopted evaporation coefficient

		Mass-Flow Rates $kg \cdot s^{-1}$			
CASE	**MN HEM** *err [%]*	**MN MIX** *err [%]*	**SN HEM** *err [%]*	**SN MIX** *err [%]*	σe
1	13.35	1.00	-18.19	9.79	600000
2	13.15	0.43	-23.33	12.08	600000
3	12.98	0.09	-32.15	16.93	600000
5	17.86	1.96	-39.13	17.28	100000
7	17.82	1.79	-37.45	15.85	100000

The new model clearly improves on the HEM for both motive and suction mass-flow rates. The former is obtained by tuning the evaporation factor coefficient, which was found to have the same order of magnitude for all the considered cases. It is worth to note that, according to what found in Section 3.2, for similar inlet boundary conditions, the value that returns the best mass-flow rate gives the best pressure profile as well. It is worth to note that for transcritical Cases, the evaporation factor is higher than subcooled liquid Cases. By increasing this parameter, a reduction of the metastability effect is operated, thus making the model more similar to the limit condition of the HEM. This means that the behavior of a transcritical flow is closer to an equilibrium phase change than a subcooled flashing flow. Similar conclusions were stated by Palacz et al. [88] where HEM and HRM (*Homogenous Relaxation Model*) performance were analysed.

The suction nozzle mass-flow rates improve on the HEM ones, but the error is still between ~10% and ~17%. In order to reduce it, a full 3D analysis should be performed and, since the developed model is based on the standard multiphase framework of ANSYS Fluent, some turbulence corrections accounting for the topology of the flow could be easily added as well by means of *UDFs.*

Figure 83 shows the comparison of the wall pressure profiles of HEM and Mixture model for all the considered cases with the experimental values. The cases are divided in two groups with similar motive nozzle inlet temperature (see Table 5), while the motive inlet pressure is the same for both groups. In this way a comparison of supercritical and subcritical ejector operation at constant pressure will be possible.

The wall pressure profiles show a general improvement of the Mixture model with respect to the HEM against the measured values. In order to precisely assess the flow behavior more pressure sensors and possibly thermocouples should be used in the future experimental test-cases to obtain detailed pressure and temperature profiles at the ejector wall. However, this may be difficult to have because of the small dimensions of R744 flashing ejectors.

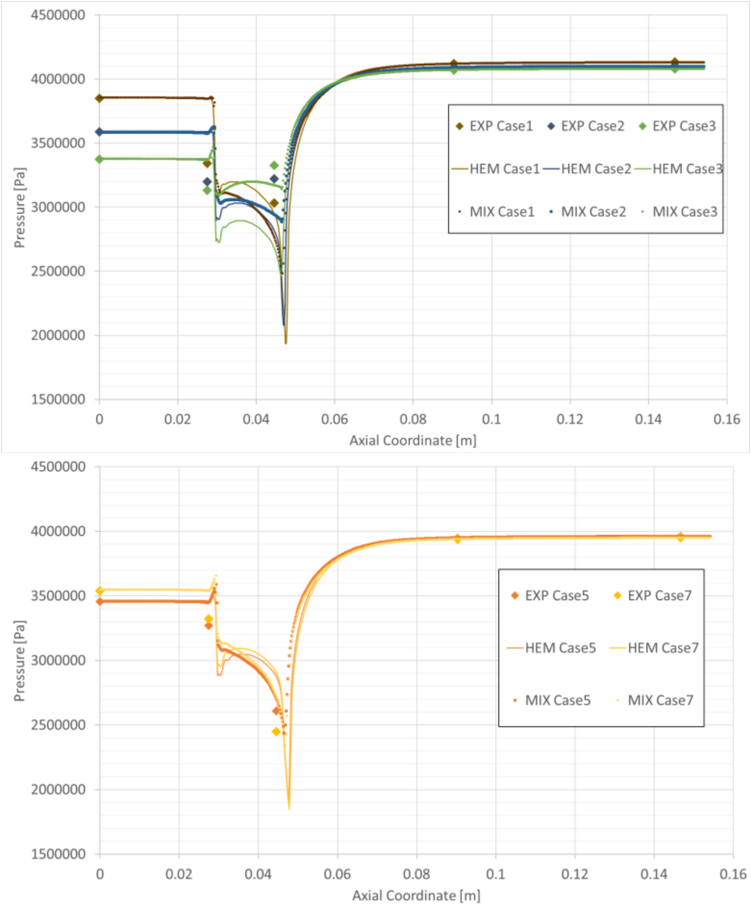

Figure 83 Ejector wall pressure profiles of HEM and Mixture model (MIX). Case 1-2-3 (TOP); Case 5-7 (BOTTOM)

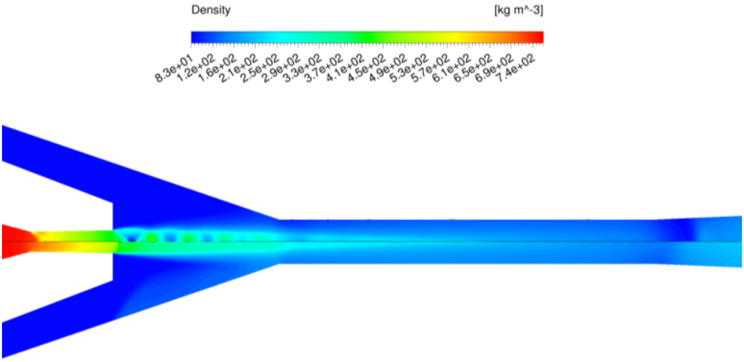

Figure 84 Density contours for Case 5. HEM (TOP), Mixture-model (BOTTOM)

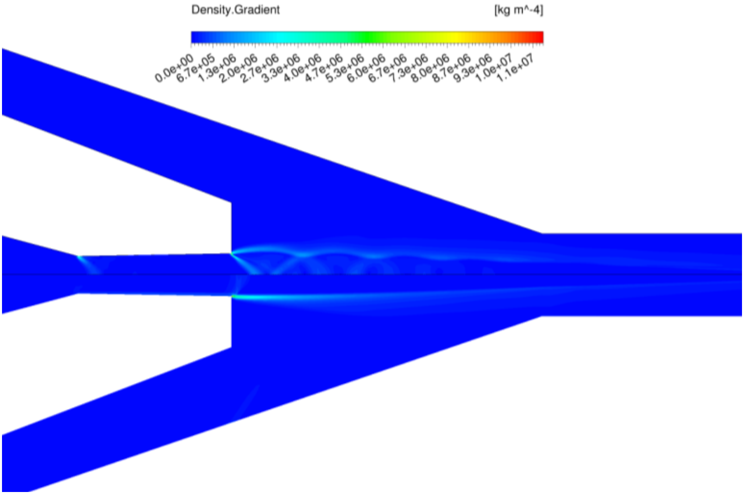

Figure 85 Density gradient contours for Case 5. HEM (TOP), Mixture-model (BOTTOM)

In Figure 84 the density contours resulting for Case 5 with HEM on the top half and Mixture-model on the bottom half are shown. The strength of shock and expansion waves at the motive nozzle exit is higher for the HEM. This is also clearly visible by looking at the density gradient contours of Figure 85. The normal shock at the beginning of the diffuser results again in an increased strength with HEM, according to the results shown in Figure 84. In agreement to what shown in Chapter 2, the non-equilibrium phase-change of the Mixture-model approach results in a damping of the mass-transfer related gradients.

Another interesting comparison can be seen in Figure 84 and Figure 85 where the results of Case 1 and Case 5 are compared in terms of density and vapor volume fraction, respectively. In this way, the differences in the supercritical (Case 1) and subcritical (Case 5) operation of the ejector at constant inlet pressure can be analyzed.

From Figure 85, an increased density at the motive nozzle inlet in Case 5 is evident, while the strength of the shock and expansion waves at motive nozzle outlet is increased for the supercritical case (Case 1). By looking at Figure 84, a delayed phase change is visible for subcritical operation. Thus resulting in an increased motive nozzle mass-flow rate of Case 5, which is confirmed by the experimental measurement (see Figure 72). The increased evaporation occurring in Case 1 in correspondence of the expansion at the nozzle exit is also visible in Figure 84.

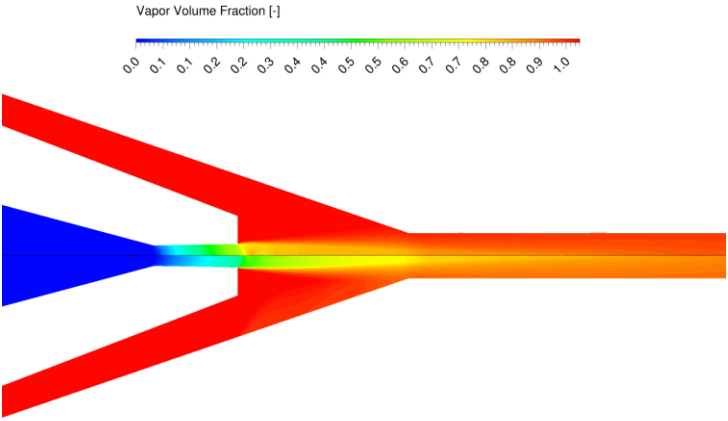

Figure 86 Vapor volume fraction contours of Mixture model. Case 1 (TOP), Case 5 (BOTTOM)

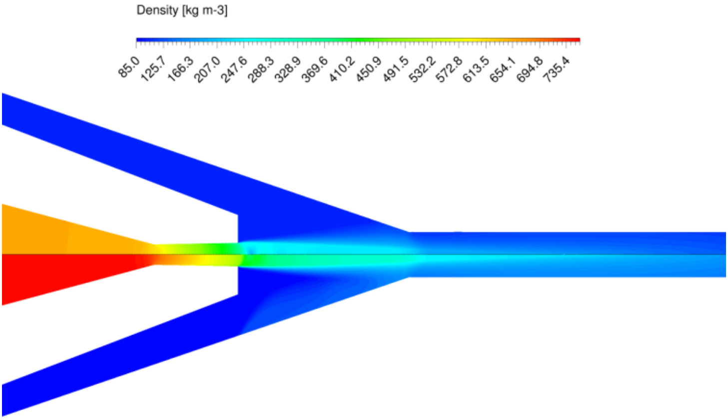

Figure 87 Density contours of Mixture model. Case 1 (TOP), Case 5 (BOTTOM)

The comparison of the Mach numbers obtained with the two different two-phase sound speed formulations (similarly to Figure 63) are shown in Figure 88 for Case 1 and Figure 89 for Case 5. In both cases, the Mach number obtained with Brennen equations results in higher values, with respect to Wallis formulation (see Chapter 1). As discussed in Section 3.2, this is more coherent with the computational model. In general, the Mach numbers of Case 5 are higher than the ones of Case 1. This is due to the lower suction nozzle pressure of the former with respect to the latter case.

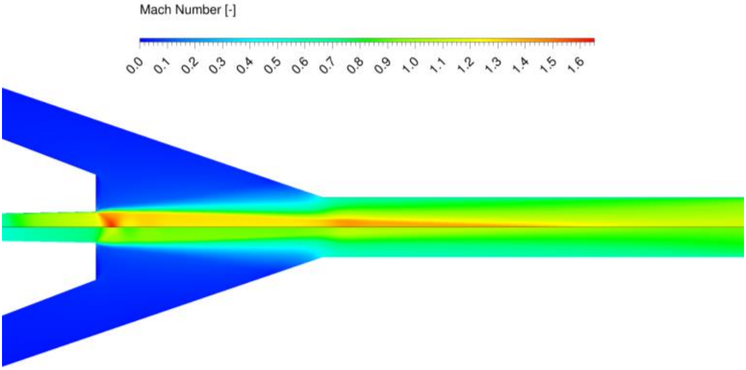

Figure 88 Mach numbers contour with different speed of sound formulations for Case 1. Brennen equation (TOP), Wallis equation (BOTTOM)

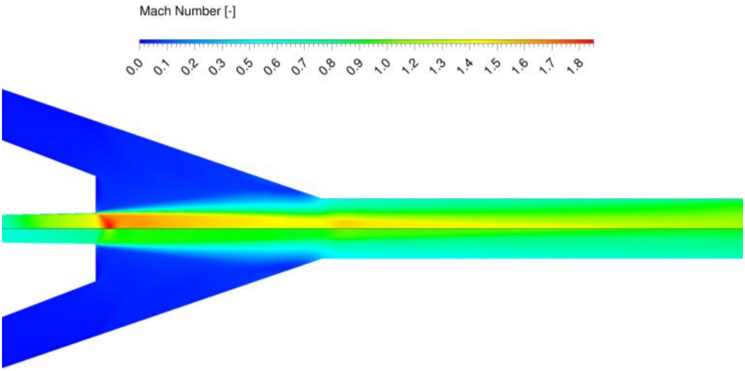

Figure 89 Mach numbers contour with different speed of sound formulations for Case 5. Brennen equation (TOP), Wallis equation (BOTTOM)

3.6 Concluding Remarks

Two numerical model for the simulation of flashing flows have been developed for the computational analysis of flashing R744 ejectors. The first one is a Homogeneous Equilibrium Model that assumes mechanical and thermal equilibrium between the phases. The second one is a Non-Equilibrium Mixture Model that accounts for metastability effects during CO_2 phase-change. Both models have been implemented within the commercial CFD software ANSYS Fluent by means of several User-Defined Functions. This approach allows great flexibility in the choice of the physical model settings, calibration parameters and fluid properties.

An experimental activity in Sintef and NTNU joint lab has been conducted in order to have experimental data on a R744 ejector. Those data have been used for the benchmarking of computational model.

The Mixture-model has shown a remarkable improvement on the HEM results, both in terms of pressure profiles and mass-flow rates. As mentioned in the previous Chapter the HEM is still valuable as a fast computational tool for preliminary analysis of ejectors.

Finally, a new formulation for the evaluation of the two-phase speed of sound has been implemented in the post-processing, showing a more coherent behavior with respect to the computational results in comparison with the standard formulation in ANSYS Fluent.

Conclusions

In the present work, three numerical models for multiphase ejectors working with natural refrigerants have been developed. The fluid considered are R718 for Heat Powered Cycles (HPC) and R744 for Vapor Compression Cycles (VCC). All the numerical models have been implemented in the commercial code ANSYS Fluent by means of User-defined Functions (UDFs). This allows for a great flexibility of all the models in the choice of physical model settings, calibration parameters as well as fluid properties.

The condensation process occurring in steam ejectors has been modeled by means of a non-equilibrium Wet-Steam (WS) model. The numerical results have been compared with a Homogeneous Equilibrium Model (HEM) and two experimental test-cases (a nozzle and a full ejector) available from the literature. The agreement with experiments was found to be satisfactory. The WS model also improves on the Homogeneous Equilibrium Model in terms of mass-flow rates and critical pressure prediction. This latter was found to be computationally efficient and more suitable as a preliminary analysis tool. Finally, a full Eulerian-Eulerian model has been developed and validated against condensing steam nozzle data. This latter model is less stable and difficult to handle for ejectors applications. However, it is interesting for future developments because of the possibility of implementing accurate modeling of phases interaction.

The flash evaporation process in the R744 ejector has been studied with the HEM and with a non-equilibrium evaporation-condensation model with real fluid properties. This latter has been validated on a flashing nozzle test-case available from the literature. Both models have finally been compared with an ejector test case. The experimental data have been collected by the author during a visiting research period in NTNU/SINTEF laboratory. The non-equilibrium model was found to improve on the HEM in terms of pressure profiles and mass-flow rates. Finally, a new speed of sound formulation applicable in the two-phase domain has been implemented as a post-processing tool. This correlation was found to be more coherent with the numerical results with respect to the standard equation of ANSYS Fluent.

As for the future activities, since both the non-equilibrium model have been implemented in the standard multiphase framework of ANSYS Fluent, several phases-interaction model as well as phases-turbulence interaction models could be added. Moreover, the presented tools could be used to develop reduced order model or lumped parameters model as done in [89], [90] and [91] in order to develop fast and reliable design methods or to explore novel geometrical features, as recently done by Bodys et al. [92], for the next generation of supersonic ejectors.

Appendix

The geometry of the combinable ejector, firstly presented by Banasiak et al. in [15] is shown in the pictures below. The geometry used in the present thesis is new and never presented before.

The drawings of the parts are general, so the specific quotes of the ejector presented in Chapter 3 are the following:

Table 12 Dimensions of the ejector parts

Nozzle	
A = 0.9 mm	B = 1.03 mm
C = 1.0 mm	
Mixing Chamber	
A = 2 mm	B = 10.91 mm
C = not available	D = 21 mm
E = 25.5 mm	
Diffuser	
A = 2 mm	B = 5 mm
C = 10 mm	D = 25.6 mm
E = 23.6 mm	F = 52.8 mm
G = 101.1 mm	
End Connector	
A = 10 mm	B = 12 mm
C = 20.5 mm	

Moreover, 2 additional spacers of 0.5mm (1mm in total) are posed between nozzle and mixer.

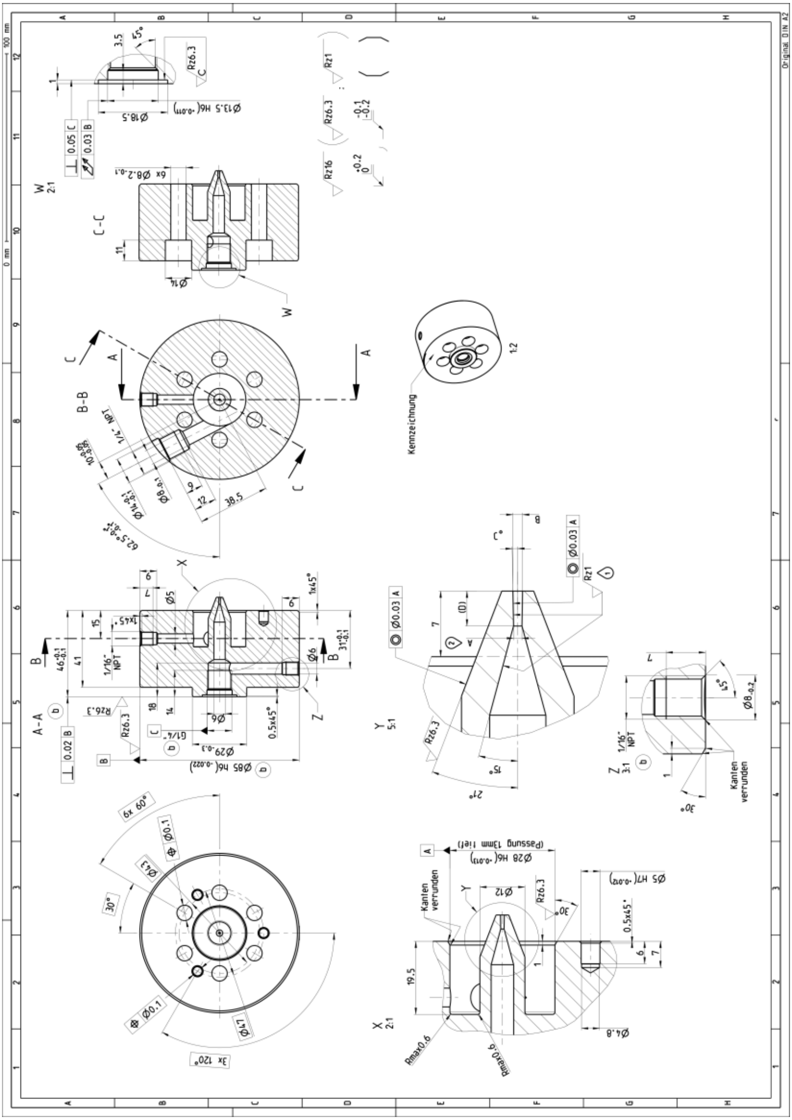

Figure 90 Nozzle Part

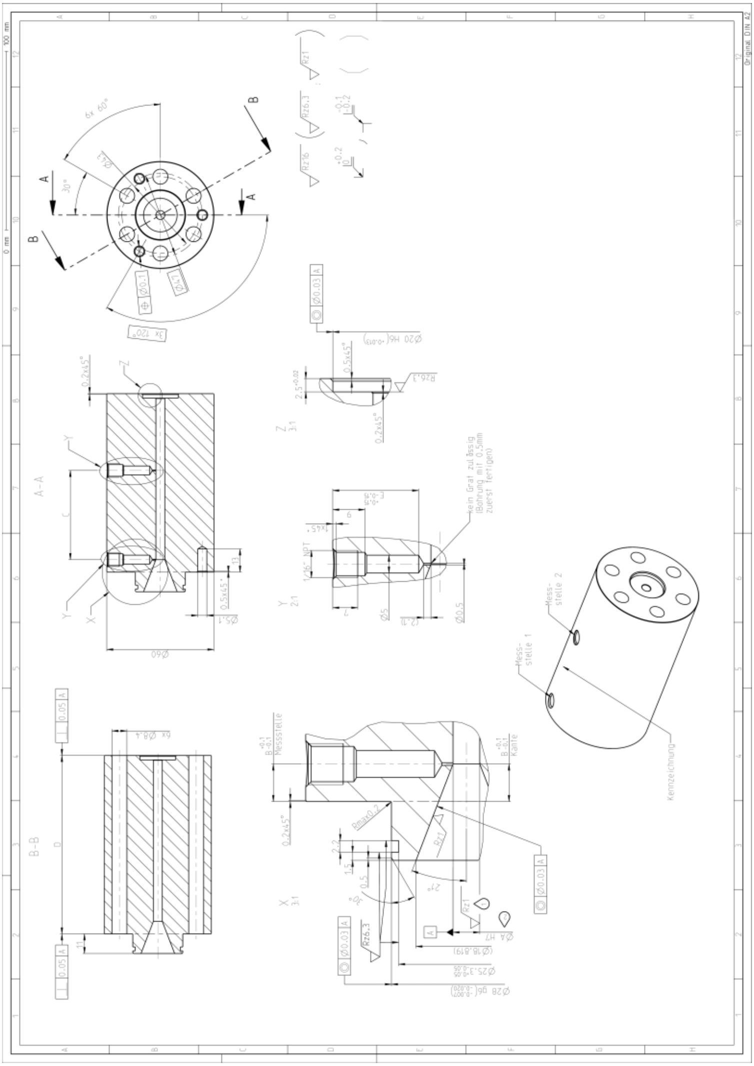

Figure 91 Mixing chamber part

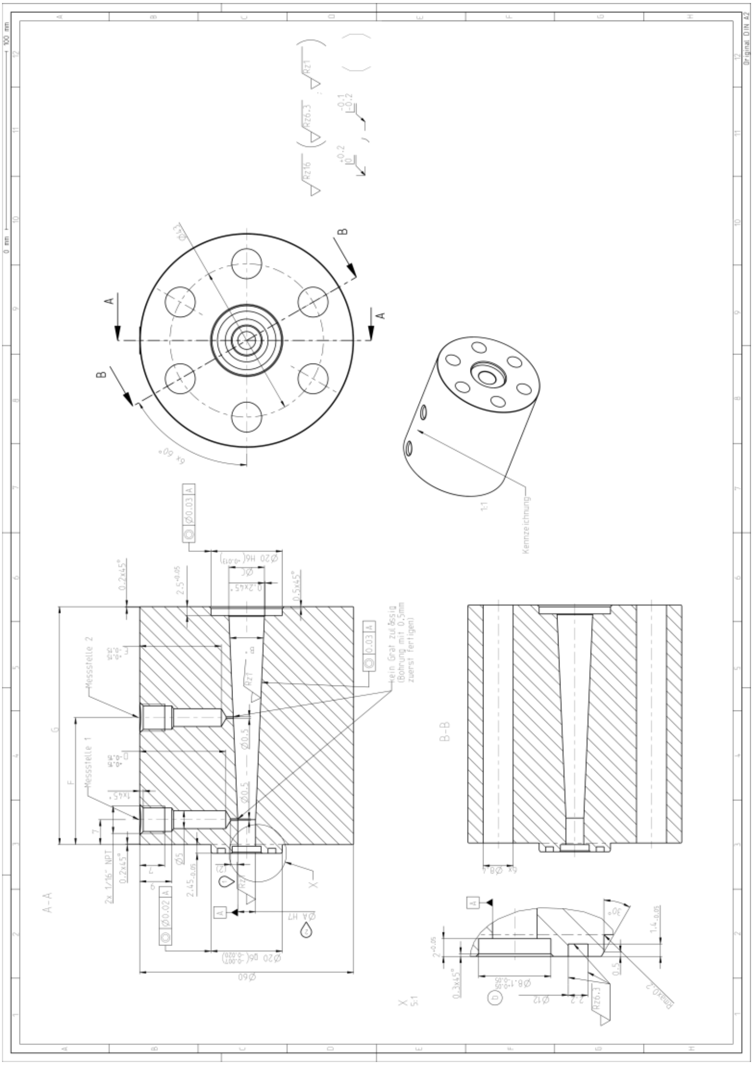

Figure 92 Diffuser part

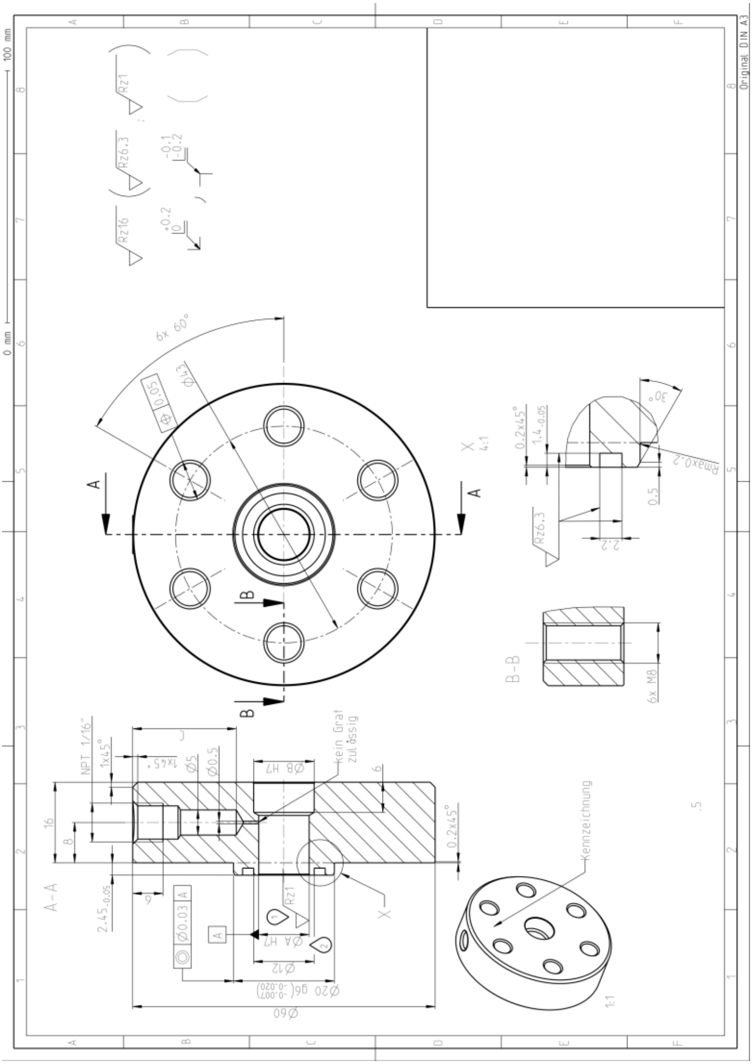

Figure 93 End-connector part

Figure 94 and Figure 95 show the combinable ejector assembled and the CO_2 test-rig, respectively.

Figure 94 Ejector assembled and mounted in the test-rig

Figure 95 Full R744 transcritical test-rig

References

[1] M.-H. Kim, J. Pettersen and C. Bullard, «Fundamental process and system design issues in CO2 vapor compression systems,» *Progress in Energy and Combustion Science,* vol. 30 , p. 119–174, 2004.

[2] S. Elbel and N. Lawrence, «Review of recent developments in advanced ejector technology,» *International Journal of Refrigeration,* pp. 1-18, 2016.

[3] S. Minetto, R. Brignoli, C. Zilio and S. Marinetti, «Experimental analysis of a new method for overfeeding multiple evaporators in refrigeration systems,» *International Journal of Refrigeration,* pp. 1-9, 2014.

[4] A. Hafner, S. Försterling and K. Banasiak, «Multi-ejector concept for R-744 supermarket refrigeration,» *International Journal of Refrigeration,* vol. 43, pp. 1-13, 2014.

[5] A. Hafner, S. Poppi, P. Nekså, S. Minetto and T. M. Eikevik, «Development of commercial refrigeration systems with heat recovery for supermarket building,» in *Proceedings of the 10th IIR Gustav Lorentzen Conference on Natural Refrigerants*, Delft, The Netherlands, 2012.

[6] P. Gullo, A. Hafner and K. Banasiak, «Transcritical R744 refrigeration systems for supermarket applications: current status and future perspectives,» *International Journal of Refrigeration,* 2018.

[7] F. Mazzelli, Single & Two-Phase Supersonic Ejectors for Refrigeration Applications, Florence: Ph.D. Thesis, 2015.

[8] G. Grazzini, A. Milazzo and F. Mazzelli, Ejectors for Efficient Refrigeration. Design, Applications and Computational Fluid Dynamics, In press a cura di, Springer, 2018.

[9] R. Zucker and O. Biblarz, Fundamentals of gas dynamics, Hoboken: John Wiley and Sons, Inc., 2002.

[10] F. Mazzelli and A. Milazzo, «Performance analysis of a supersonic ejector cycle working with R245fa,» *International Journal of Refrigeration,* vol. 49, pp. 79-92, 2015.

[11] K. Matsuo, Y. Miyazato and H. Kim, « Shock train and pseudo-shock phenomena in internal gas flows,» *Progress in Aerospace Sciences* , vol. 35 , pp. 33-100, 1999.

[12] A. Pope and K. Goin, High-Speed Wind Tunnel Testing, Wiley, 1978.

[13] A. H. Shapiro, The Dynamics and Thermodynamics of Compressible Fluid Flow, Vol. II, New York: Ronald Press, 1953.

[14] S. Elbel and P. Hrnjak, «Experimental validation of a prototype ejector designed to reduce throttling losses encountered in transcritical R744 system operation,» *International Journal of Refrigeration,* pp. 411-422, 2008.

[15] K. Banasiak, A. Hafner and T. Andresen, «Experimental and numerical investigation of the influence of the two-

phase ejector geometry on the performance of the R744 heat pump,» *International Journal of Refrigeration,* vol. 35, pp. 1617-1625, 2012.

[16] G. Polanco, A. Holdøb and G. Munday, «General review of flashing jet studies,» *Journal of Hazardous Materials,* vol. 173, p. 2–18, 2010.

[17] V. P. Carey, Liquid-Vapor Phase-Change Phenomena, CRC Press, 2007.

[18] H. Stadtke, Gasdynamic Aspects of Two-Phase Flow, Weinheim: Wiley-VCH Verlag Gmbh and Co., 2006.

[19] C. Brennen, Cavitation and Bubble Dynamics, Oxford University Press, 1995.

[20] M. Labois and C. Narayanan, «Non-conservative pressure-based compressible formulation for multiphase flows with heat and mass transfer,» in *9th International Conference on Multiphase Flow*, May 22nd - 27th, Firenze, Italy, 2016.

[21] C. E. Brennen, Fundamentals of Multiphase Flows, Pasadena, California: Cambridge University Press, 2005.

[22] M. De Lorenzo, P. Lafon, M. Di Matteo, M. Pelanti, J. M. Seynhaeve and Y. Bartosiewicz, «Homogeneous two-phase flow models and accurate steam-water table look-up method for fast transient simulations,» *International Journal of Multiphase Flow,* vol. 95, pp. 199-219, 2017.

[23] K. Ameur, Z. Aidoun and M. Ouzzane, «Modeling and numerical approach for the design and operation of two-

phase ejectors,» *Applied Thermal Engineering,* vol. 109, pp. 809-818, 2016.

[24] F. Giacomelli, G. Biferi, F. Mazzelli and A. Milazzo, «CFD modeling of the supersonic condensation inside a steam ejector,» *Energy Procedia,* pp. 1224-1231, 2016.

[25] F. Mazzelli, F. Giacomelli and A. Milazzo, «CFD modelling of the condensation inside a Supersonic Nozzle: implementing customized wet-steam model in commercial codes,» *Energy procedia* , vol. 126, pp. 34-41, 2017.

[26] F. Mazzelli, F. Giacomelli and A. Milazzo, «CFD modeling of condensing steam ejectors: comparison with an experimental test-case,» *International Journal of Thermal Sciences,* vol. 127, n. C, pp. 7-18, 2018.

[27] F. Mazzelli, F. Giacomelli and A. Milazzo, «Numerical modeling of a supersonic steam ejector for a heat powered refrigeration systems,» *Refrigeration Science and Technology,* pp. 1315-1323, 2018.

[28] P. P. Wegener and L. M. Mack, «Condensation in Supersonic Wind Tunnels,» in *Advances in Apllied Mechanics*, New York, Academic Press Inc., 1958, pp. 307-440.

[29] P. G. Hill, «Condensation of water vapour during supersonic expansion in nozzles,» *J. Fluid Mech.,* vol. 25, n. 3, pp. 593-620, 1966.

[30] K. Ariafar, D. Buttsworth and G. Al-Doori, «Effect of mixing on the performance of wet steam ejectors,» *Energy,* vol. 93, pp. 2030-2041, 2015.

[31] F. Mazzelli, D. Brezgin, I. Murmanskii, N. Zhelonkin and A. Milazzo, «Condensation in supersonic steam ejectors: comparison of theoretical and numerical models, International Conference on Multiphase Flow, ICMF,» in *Proceedings of 9th International Conference on Multiphase Flow*, Florence, 2016.

[32] ANSYS Inc., ANSYS Fluent Theory Guide, Canonsburg, PA: release 18.0, 2016.

[33] J. Starzmann, F. R. Huges, A. J. White, J. Halama, V. Hric, M. Kolovratnik, H. Lee, L. Sova, M. Statny, S. Schuster, M. Grubel, M. Schatz, D. M. Vogt, P. Y., G. Patel, T. Turunen-Saaresti, V. Gribin, V. Tishchenko, I. Garilov and et al., «Results of the International Wet Steam Modelling Project,» Prague, 2016.

[34] A. Gerber and M. Kermani, «A pressure based Eulerian-Eulerian multiphase model for non-equilibrium condensation in transonic steam flow,» *International Journal of Heat and Mass Transfer,* pp. 2217-2231, 2004.

[35] L. Zori and F. Kelecy, «Wet Steam Flow Modeling in a General CFD Fow Solver,» in *35th AIAA Fluid Dynamics Conference and Exhibit*, Toronto, Canada, 2005.

[36] T. Sriveerakul, S. Aphornratana and K. Chunnanond, «Performance prediction of steam ejector using computational fluid: Part 1. Validation of the CFD

results,» *International Journal of Thermal Sciences,* vol. 46, pp. 812-822, 2007.

[37] X. Wang, H. Lei, J. Dong and J. Tu, «The spontaneously condensing phenomena in a steam-jet pump and its influence,» *International Journal of Heat and Mass Transfer,* vol. 55, p. 4682–4687, 2012.

[38] C. A. Moses and G. D. Stein, «On the growth of steam droplets formed in a Laval nozzle using both static pressure and light scattering measurements,» *Journal of Fluids Engineering,* pp. 311-322, 1978.

[39] G. Al-Doori, Investigation of Refrigeration System Steam Ejector Performance Through Experiments and Computational Simulations, Ph.D. thesis, University of Southern Queensland, 2013.

[40] E. Lemmon, M. Huber and M. McLinden, «NIST Standard Reference Database 23: Reference Fluid Thermodynamic and Transport Properties-REFPROP, Version 9.1,» 2013.

[41] The MathWorks Inc., MATLAB, version 8.6.0 (R2015b), Natick, Massachusetts, 2015.

[42] J. Smolka, Z. Bulinski, A. Fic, A. J. Nowak, K. Banasiak and A. Hafner, «A computational model of a transcritical R744 ejector based on a homogeneous real fluid approach,» *Applied Mathematical Modelling,* pp. 1208-1224, 2013.

[43] C. Lucas, H. Rusche, A. Schroeder and J. Koehler, «Numerical investigation of a two-phase CO2 ejector,» *International Journal of Refrigeration,* pp. 154-166, 2014.

[44] M. Palacz, J. Smolka, A. Fic, Z. Bulinski, A. Nowak, K. Banasiak and A. Hafner, «Application range of the HEM approach for CO2 expansion inside two-phase ejectors for supermarket refrigeration systems,» *International Journal of Refrigeration,* vol. 59, p. 251–258, 2015.

[45] M. Haida, J. Smolka, A. Hafner, M. Palacz, K. Banasiak and A. J. Nowak, «Modified homogeneous relaxation model for the R744 trans-critical flow in a two-phase ejector,» *International Journal of Refrigeration,* vol. 85, pp. 314-333, 2018.

[46] P. Palacz, J. Smolka, W. Kus, A. Fic, Z. Bulinski, A. Nowak, K. Banasiak and A. Hafner, «CFD-based shape optimisation of a CO2 two-phase ejector mixing section,» *Applied Thermal Engineering,* vol. 95, p. 62–69, 2016.

[47] P. Palacz, J. Smolka, A. Nowak, K. Banasiak and A. Hafner, «Shape optimisation of a two-phase ejector for CO2 refrigeration systems,» *International Journal of Refrigeration,* vol. 74, p. 212–223, 2017.

[48] F. Mazzelli, A. B. Little, S. Garimella and Y. Bartosiewicz, «Computational and Experimental Analysis of Supersonic Air Ejector: Turbulence Modeling and Assessment of 3D Effects,» *International Journal of Heat and Fluid Flow,* vol. 56, pp. 305-316, 2015.

[49] F. Bakhtar, J. B. Young, A. J. White and D. A. Simpson, «Classical nucleation theory and its application to condensing steam flow calculations,» in *Proceedings of the*

Institution of Mechanical Engineers, Part C: Journal of Mechanical Engineers Science, 2005.

[50] A. Kantrovitz, «Nucleation in very rapid vapour expansions,» *J. Chem. Phys.,* vol. 19, pp. 1097-1100, 1951.

[51] J. B. Young, «The Spontaneous Condensation in Supersonic Nozzles,» *PhysicoChemical Hydrodynamics,* vol. 3, n. 1, pp. 57-82, 1982.

[52] International Assotiation for the Properties of Water and Steam, «Thermophysical Properties of Metastable Steam and Homogeneous Nucleation,» 2011.

[53] J. B. Young, «An Equation of State for Steam for Turbomachinery and Other Flow Calculations,» *Journal of Engineering for Gas Turbines and Power,* vol. 110, n. 1, pp. 1-7, 1988.

[54] Y. Yang and S. Shen, «Numerical simulation on non-equilibrium spontaneous condensation,» *International Communications in Heat and Mass Transfer* , vol. 36, pp. 902-907, 2009.

[55] B. Leonard, «A stable and accurate convective modelling procedure based on quadratic upstream interpolation,» *Computer Methods in Applied Mechanics and Engineering,* vol. 19, pp. 59-98, 1979.

[56] G. Gyarmathy, «Bases for a theory for wet steam turbines,» PhD thesis, ETH Zurich, 1962.

[57] M. Joswiak, N. Duff, M. Doherty and B. Peters, «Size-Dependent Surface Free Energy and Tolman-Corrected

Droplet Nucleation of TIP4P/2005 Water,» *J. Phys. Chem. Lett.* , vol. 4, p. 4267–72, 2013.

[58] F. R. Menter, «Two-Equation Eddy-Viscosity Turbulence Models for Engineering Applications,» *AIAA Journal,* vol. 32, n. 8, pp. 1598-1605, 1994.

[59] W. Wróblewski, S. Dykas and A. Gepert, «Steam condensing flow modeling in turbine channels,» *International Journal of Multiphase Flow,* vol. 35, pp. 498-506, 2009.

[60] F. Hughes, J. Starzmann, A. White and Y. J.B., «A Comparison of Modeling Techniques for Polydispersed Droplet Spectra in Steam Turbines,» *Journal of Engineering for Gas Turbines and Power,* vol. 138, 2016.

[61] H. Ikawa, Turbulent Mixing Layer in Supersonic Flow, Ph.D. thesis, California Institute of Technology, 1973.

[62] G. Brown and A. Roshko, «On density effects and large structure in turbulent mixing layers,» *journal of Fluid Mechanics* , vol. 64, pp. 775-816, 1974.

[63] A. J. Smits and J. P. Dussauge, Turbulent Shear Layers in Supersonic Flow, second edition, New York, NY: Springer, 2006.

[64] T. B. Gatsky and J. P. Bonnet, Compressibility, Turbulence and High Speed Flow, 2nd edition, Oxford, UK.: Academic Press, 2013.

[65] D. Wilcox, «Dilatation–dissipation corrections for advanced turbulence models,» *AIAA Journal,* vol. 11, pp. 2639-2646, 1992.

[66] D. Wilcox, Turbulence Modeling for CFD, La Canada, California: DCW Industries, Inc, 2006.

[67] C. Crowe, J. Schwarzkopf, M. Sommerfeld and Y. Tsuji, Multiphase flows with droplets and particles, second edition, Boca Raton, FL: CRC Press, 2012.

[68] H. R. Pruppacher, «A new look at homogeneous ice nucleation in supercooled water drops,» *J. Atmos. Sci.* , vol. 52, pp. 1924-33, 1995.

[69] J. Wölk, B. Wyslouzil and R. Strey, «Homogeneous nucleation of water: From vapor to supercooled droplets to ice,» *AIP Conf. Proc.,* vol. 1527, pp. 55-62, 2013.

[70] A. Gerber, R. Sigg, L. Völker, M. Casey and N. Sürken, «Predictions of non-equilibrium phase transition in a model low-pressure steam turbine,» *Proc. IMechE Vol. 221 Part A: J. Power and Energy,* pp. 825-35, 2007.

[71] A. J. White, J. B. Young and P. T. Walters, «Experimental validation of condensing flow theory for a stationary cascade of steam turbine blades,» *Philos. Trans. R. Soc. Lond.,* pp. 59-88, 1996.

[72] F. Giacomelli, F. Mazzelli and A. Milazzo, "Evaporation in supersonic CO2 ejectors: analysis of theoretical and numerical models," in *International Conference on Multiphase Flow*, Firenze, Italy, 2016.

[73] F. Giacomelli, K. Banasiak, A. Hafner, F. Mazzelli and A. Milazzo, «Experimental and Numerical Investigation on an Ejector for CO2 Vapor,» *Refrigeration Science and Technology,* pp. 1307-1314, 2018.

[74] F. Giacomelli, F. Mazzelli and A. Milazzo, «A novel CFD approach for the computation of R744 flashing nozzles in compressible and metastable conditions,» *Energy,* vol. 162, pp. 1092-1105, 2018.

[75] G. Lorentzen, «Revival of carbon dioxide as a refrigerant,» *International Journal of Refrigeration,* pp. 292-301, 1993.

[76] M. Yazdani, A. A. Alahyari and T. Radcliff, «Numerical modeling of two-phase supersonic ejectors for work-recovery applications,» *International Journal of Heat and Mass Transfer,* pp. 5744-5753, 2012.

[77] M. F. Colarossi, Multidimensional Modeling of Condensing Two-Phase Ejector Flow, University of Massachusetts Amherst, 2011.

[78] ANSYS Inc., ANSYS Fluent Theory Guide, Canonsburg, PA: release 19.0, 2018.

[79] M. Nakagawa, M. S. Berana and A. Kishine, «Supersonic two-phase flow of CO2 through converging-diverging nozzles for the ejector refrigeration cycle,» *International Journal of Refrigeration,* vol. 32, pp. 1195-1202, 2009.

[80] J. P. Janet, Y. Liao and D. Lucas, «Heterogeneous nucleation in CFD simulation of flashing flows in

converging–diverging nozzles,» *International Journal of Multiphase Flow* , vol. 74 , p. 106–117, 2015.

[81] Q. Dang Le, R. Mereu, G. Besagni, V. Dossena and F. Inzoli, «Computational Fluid Dynamics Modelling of Flashing Flow in Convergent-Divergent Nozzle,» *ASME: Journal of Fluids Engineering,* vol. 140, pp. 101102-1-101102-22, 2018.

[82] Y. Liao and D. Lucas, «Possibilities and Limitations of CFD Simulation for Flashing Flow Scenarios in Nuclear Applications,» *Energies,* 2017.

[83] K. Karathanassis. I., P. Koukouvinis and M. Gavaises, «Comparative evaluation of phase-change mechanisms for the prediction of flashing flows,» *International Journal of Multiphase Flow,* n. 95, p. 257–270, 2017.

[84] Y. Fang, M. De Lorenzo, P. Lafon, S. Poncet and Y. Bartosiewicz, «An Accurate and Efficient Look-up Table Equation of State for Two-phase Compressible Flow Simulations of Carbon Dioxide,» *Industrial and Engineering Chemistry Research,* 2018.

[85] R. Span and W. Wagner, «A New Equation of State for Carbon Dioxide Covering the Fluid Region from the Triple-Point Temperature to 1100K at Pressure up to 800MPa,» *J. Phys. Chem,* vol. 25, n. 6, pp. 1509-1595, 1996.

[86] K. Banasiak, A. Hafner, E. E. Kriezi, K. B. Madsen, M. Birkelund, K. Fredslund and R. Olsson, «Development and performance mapping of a multiejector expansion work

recovery pack for R744 vapour compression units,» *International Journal of Refrigeration,* pp. 265-276, 2015.

[87] K. Banasiak and A. Hafner, «1D Computational model of a two-phase R744 ejector for expansion work recovery,» *International Journal of Refrigeration,* pp. 2235-2247, 2011.

[88] M. Palacz, M. Haida, J. Smolka, A. J. Nowak, K. Banasiak and A. Hafner, «HEM and HRM accuracy comparison for the simulation of CO2 expansion in two-phase ejectors for supermarket refrigeration systems,» *Applied Thermal Engineering,* vol. 115, pp. 160-169, 2017.

[89] G. Besagni, R. Mereu, P. Chiesa and F. Inzoli, «An Integrated Lumped Parameter-CFD approach for off-design ejector performance evaluation,» *Energy Conversion and Management,* vol. 105, pp. 697-715, 2015.

[90] G. Besagni, R. Mereu, G. Di Leo and F. Inzoli, «A study of working fluids for heat driven ejector refrigeration using lumped parameter models,» *International Journal of Refrigeration,* vol. 58, pp. 154-171, 2015.

[91] M. Haida, J. Smolka, A. Hafner, Z. Ostrowski, M. Palacz, K. B. Madsen, S. Forsterling, A. J. Nowak and K. Banasiak, «Performance mapping of the R744 ejectors for refrigeration and air conditioning supermarket application: A hybrid reduced-order model,» *Energy,* vol. 153, pp. 933-948, 2018.

[92] J. Bodys, J. Smolka, K. Banasiak, M. Palacz, M. Haida and A. J. Nowak, «Performance improvement of the R744

two-phase ejector with an implemented suction nozzle bypass,» *Energy,* vol. 90, pp. 216-228, 2018.

The author is grateful to all people without whom this work would not have been possible. First of all, my supervisors Prof. Grazzini and Prof. Milazzo, for their suppert and pretious advices. Secondly, my gratitude goes to my incomparable colleagues in Florence and Trondheim: Dr. Federico Mazzelli, Jafar Mahmoudian and Dr. Paride Gullo, who helped me in many ways. Special thanks go also to Prof. Hafner and Dr. Banasiak who kindly welcomed me during my stay at NTNU. I would also like to thank my family and friends for the sympathy they demonstrated in many occasions.

Lastly, I would like to dedicate this work to Elena, with the hope of a life together in the years to come.

La felicità della tua vita dipende dalla
qualità dei tuoi pensieri.

[Marco Aurelio]